Mapping Deflections of Extragalactic Ultrahigh-Energy Cosmic Rays in Magnetohydrodynamic Simulations of the Local Universe[¶]

K. Dolag[1], D. Grasso[2], V. Springel[3], and I. Tkachev[4]

[1] *Dipartimento di Astronomia, Universitá di Padova, Padua, Italy*
[2] *Scuola Normale Superiore and I.N.F.N., Pisa, Italy*
[3] *Max-Planck-Institut für Astrophysik, Garching, Germany*
[4] *CERN – Theory Division, Geneva, Switzerland*
Submitted April 22, 2004; in final form, May 12, 2004

We construct a map of deflections of ultrahigh-energy cosmic rays by extragalactic magnetic fields using a magnetohydrodynamical simulation of cosmic structure formation that realistically reproduces the positions of known galaxy clusters in the Local Universe. Large deflection angles occur in cluster regions, which, however, cover only an insignificant fraction of the sky. More typical deflections of order $\lesssim 1°$ are caused by crossings of filaments. For protons with energies $E \geq 4 \times 10^{19}$ eV, deflections do not exceed a few degrees over most of the sky up to a propagation distance of 500 Mpc. Given that the field strength of our simulated intergalactic magnetic field forms a plausible upper limit, we conclude that charged particle astronomy is in principle possible. © 2004 MAIK "Nauka/Interperiodica".

PACS numbers: 98.70.Sa; 95.30.Qd

INTRODUCTION

Considerable effort is presently being undertaken around the world to create [1, 2] experiments devoted to determining the composition, energy spectrum, and arrival directions of ultrahigh-energy cosmic rays (UECRs). This challenge is in part motivated by the Greisen–Zatsepin–Kuzmin (GZK) puzzle [3], which became particularly acute with Fly-Eye and AGASA data [4], and by the realization that the UECR flux at $E > 10^{19}$ eV is probably dominated by the emission of sources which are quite different from conventional galactic sources. The directional information may allow the identification of UECR sources, provided primary particles are not deflected too much by galactic and intergalactic magnetic fields (IGMFs).

Several arguments suggest that UECRs are electrically charged nuclei, most likely protons. The possibility of neutral particles is not ruled out but needs not be discussed here since such rays point back to the sources anyway. It is possible that a fraction of UECRs is comprised of iron nuclei, see, e.g., [5]. However, according to an analysis of inclined events recorded by the Haverah Park shower detector [6], above 10^{19} eV, less than 30% of the primary cosmic rays can be iron nuclei at the 95% confidence level. In what follows, we normalize our results to the case of protons. The case of other nuclei can be recovered by multiplication with their charge, Z.

Galactic magnetic fields (MF) with $B_{gal} \sim 1$ μG are not expected to produce significant deflections at extremely high energies, $E \gtrsim 10^{20}$ eV in the case of protons. Even at lower energies $E \sim 4 \times 10^{19}$ eV, strategies have been proposed which allow source identification without detailed knowledge of the galactic MF [7].

The very attractive perspective to do astronomy with proton primaries might however be spoiled by the presence of strong IGMFs. So far, evidence of the presence of IGMFs has been found only within, or very close to, rich clusters of galaxies. The most relevant observations are those based on Faraday rotation measurements (RMs) of the polarized radio emission of sources located within or behind clusters and on the synchrotron emission of relativistic electrons in the intracluster MF. The results of both methods imply the presence of MFs with strength at the μG level extending up to 1 Mpc from cluster centers. The coherence length of the field is inferred to lie in the range 10–100 kpc (see recent review [8] and references therein). Such fields certainly do induce large deflections of UECR protons that cross clusters of galaxies. However, galaxy clusters fill only a tiny fraction of the volume of the universe, so that we may expect them to produce large deflections at best over a small portion of the sky [9, 10]. Outside clusters, only upper limits on the IGMF strength are available. They are at the level of 1–10 nG for fields extending over cosmological distances with coherence lengths in the range from 50 to 1 Mpc, respectively [11]. These bounds do not hold for MFs in clustered

---

[¶]This article was submitted by the authors in English.

regions, like filaments connecting galaxy clusters, where the field might be as large as 10^{-7} G. In principle, either a weak all pervading smooth field or stronger fields localized in a complex web of filaments may produce sizable deflections of UECRs over a large portion of the sky. It is hence evident that a better knowledge of the large-scale magnetic structure of the universe is called for.

In this letter, we approach this problem by means of numerical simulations of cosmic structure formation, where we combine the collisionless dynamics of the dark matter component with the magnetohydrodynamics (MHD) of the magnetized gas. Our basic hypothesis is that the MFs observed in rich clusters of galaxies are the outcome of an MHD amplification process powered by the hierarchical formation of clusters. This assumption is supported by the results of previous simulations which, under the same hypothesis that we adopt here, succeeded in reproducing the general features of RMs in several observed clusters [12]. The tiny seed field required to initiate the amplification process may be either of primordial origin [13] or the result of a battery associated with the initial stages of structure formation [14].

Simulations of the magnetic structure of the Universe and of the UECR propagation within it have been previously attempted by several authors [14–16]. A novel achievement of our work is that we have performed *constrained simulations*, which reproduce the observed large scale structures in the nearby universe, leaving essentially no ambiguity for the choice of observer position. This is quite relevant in the present context, since it has been shown [16] that the angular distribution, as well as the energy spectrum, of UECRs reaching an observer located in a weakly magnetized region may differ considerably from that seen by a strongly magnetized one. Furthermore, by tracing UECR trajectories in the simulated magnetic structures, we are able to construct maps of expected UECR deflections as a function of distance that, for the first time, account for the actual large-scale structure as seen from the Galaxy.

MHD simulations of the Local Universe. We use initial conditions that were constructed from the IRAS 1.2-Jy galaxy survey by first smoothing the observed galaxy density field on a scale of 7 Mpc, evolving it linearly back in time, and then using it as a Gaussian constraint for an otherwise random realization of the ΛCDM cosmology. In [19], it was shown that these constrained initial conditions, when evolved to the present time, reproduce the observed density and velocity field of the Local Universe. In addition, they allow a direct identification of prominent clusters (Virgo, Coma, Centaurus, Hydra, Perseus, A3627, and Pavo) with counterparts formed in the simulation, which are found at the right places, and with approximately the correct observed masses. We extended the initial conditions of [19] by adding gas, together with an initial MF. The volume filled by high resolution particles within

our simulation is a sphere of radius ~115 Mpc centered on the Milky Way. This region comfortably includes the entire local super cluster (LSC) and is modeled with a maximum spatial resolution of 10 kpc. The simulation uses 51 million gas particles of mass 6.9×10^8 M$_\odot$, 51 million high-resolution dark matter particles, and an additional 7 million boundary particles in the distant low-resolution region.

We evolved the initial conditions with the newest version of the GADGET code [17], adding the magnetic smoothed particle hydrodynamics (MSPH) technique [12] to follow MF evolution. Previous work [12] showed that magnetic seed fields in the range of $(1–5) \times 10^{-9}$ G at redshift $z_* \simeq 20$ will be amplified due to the structure formation process and reproduce RMs in clusters of galaxies. This corresponds to $B(z_*)(1 + z_*)^{-2} \simeq 0.2 – 1 \times 10^{-11}$ G at the present time in the unclustered intergalactic medium (IGM). It was also demonstrated that the MF amplification process completely erases any memory of the initial field configuration in high density regions like galaxy clusters. Therefore, we can safely set the coherence length $l_c(z_{in})$ of the initial seed field to be infinite in our simulation. Although this assumption is probably unrealistic, it does not lead to underestimation of the UECR deflections. Concerning the initial strength of the MF, we used the highest value which still allowed previous MSPH simulations to successfully reproduce RMs in clusters; i.e., the results presented here give safe upper bounds on UECR deflections.

Clusters are generally connected by magnetized filamentary structures of gas and dark matter, where high-density filaments often harbor small clusters or groups. We find that shock fronts and shear flows are ubiquitous in these filaments, giving rise to substantial MHD amplification in these structures, boosting the MF intensity far above the expectation of adiabatic compression alone, as pointed out in [12]. We also identified low density filaments where the MF is roughly aligned along their axis, with a strength of ~10^{-4} µG. This is consistent with a purely adiabatic amplification of the seed MF due to the compression of field lines. We find no significant MF in the neighborhood of the Milky Way's position, which is contrained to lie within a sphere of 7 Mpc around the origin. We find a group of four halos aligned within the super galactic plane in this region, corresponding to the Local Group. Due to the lack of small-scale constraints, it is not certain which of the four galaxies should be best associated with the Milky Way, but this does not affect our results. Because it is a small galaxy group, the MFs associated with the group are sufficiently weak to not lead to significant deflections, despite covering a large fraction of the sky.

Deflections of charged UECRs. Having obtained a 3D model of MFs in the Local Universe, we can construct an associated map of deflections of charged particles under the action of the Lorentz force. We consider here only protons with energy $E = 4 \times 10^{19}$ eV. This is
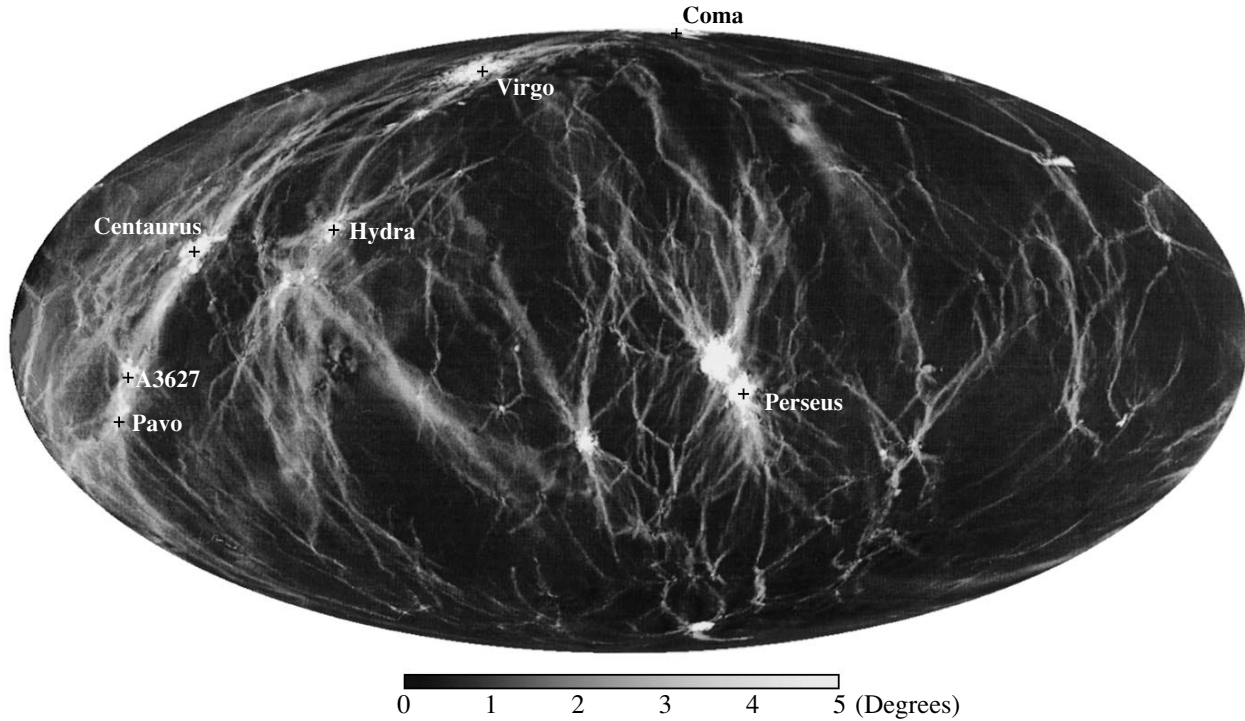
Fig. 1. Full sky map (area preserving projection) of deflection angles for UECRs with energy 4×10^{19} eV using a linear color scale. All structure within a radius of 107 Mpc around the position of the Galaxy was used. The coordinate system is galactic, with the galactic anticenter in the middle of the map. Positions of identified clusters are marked using the locations of the corresponding halos in the simulation. Note that deflections internal to the Milky Way have not been included

the threshold value for the process of photo-pion production in collisions with cosmic microwave background (CMB) photons ($p + \gamma_{CMB} \longrightarrow p(n) + \pi^{0(+)}$). The energy loss length is large, $l_E \sim 1000$ Mpc (for a recent review, see, e.g., [18]), and initially higher proton energies quickly degrade into this range. Neglecting energy losses and taking $E = 4 \times 10^{19}$ eV to be the energy at detection, we obtain upper bounds for the deflections of protons with higher energy, since the deflection angle decreases, linearly increasing the energy.

We do not follow particle trajectories directly; instead, we compute accumulated deflections along rectilinear paths. This is a reasonable simplification since we are not interested in actual source positions but rather in finding directions with small deflections. In Fig. 1, we show a deflection map obtained by tracing an isotropic distribution of protons from a maximal distance of $d_{max} = 107$ Mpc to the observer. Recall that Fig. 1 represents a map of deflections, not a distribution of arrival directions. The former is independent of the assumed distribution of UECR sources.

The pattern of clusters and filaments is clearly visible in Fig. 1. Large deflections are produced only when protons cross the central regions of galaxy clusters, and most of these strong deflections are found along a strip which can be approximately identified with the Great Attractor. The observed positions of Virgo, Coma, Hydra, and Centaurus lie in this region. Their locations

quite precisely coincide with regions where the deflections exceed 4°. Perseus and other minor clusters produce large deflections in other well-delineated regions of the sky. Outside clusters, which occupy only a small fraction of the sky, deflections of 1°–2° occur along an intricate network of filaments, covering a larger area.

The regions with $\delta \ll 1°$ correspond to voids where the MF strength is even smaller than 10^{-11} G.

In order to investigate the relative importance of deflectors at different distances, we also produced deflection maps that only included deflectors up to some maximum distance. We observe no significant deflections produced at distances smaller than 7 Mpc. Massive clusters at large distances (~100 Mpc) produce large deflections but cover only a negligible fraction of the sky, so that the bulk of the deflections is produced by passages through filaments.

In Fig. 2, we plot the fraction of the sky, $A(\delta_{th})$, over which deflections larger than δ_{th} are found for different propagation distances. We see that deflections larger than 1° are to be expected over less than 20% of the sky up to the distance $d = 107$ Mpc. For large distances d, we find that $A(\delta_{th}, d)$ approaches a self-similar behavior, viz. $A(\delta_{th}, d) = A_0(\delta_{th} \times (d_0/d)^\alpha)$. Numerically, we observe $\alpha = 0.8$ for $70 < d/\text{Mpc} < 110$. Self-similarity is consistent with the assumption that the density of deflectors (filaments) reaches a constant value at large distances. Since MFs are uncorrelated in different fila-
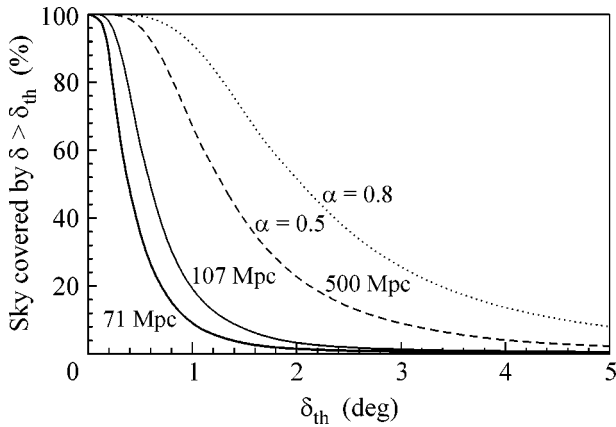
Fig. 2. Cumulative fraction of the sky with deflection angle larger than δ_{th} for several values of propagation distance (solid lines). We also include an extrapolation to 500 Mpc, assuming self-similarity with $\alpha = 0.5$ (dashed line) or $\alpha = 0.8$ (dotted line). The assumed UECR energy for all lines is 4.0×10^{19} eV.

ments, multiple filament crossings should produce a "random walk" in the deflection angle, resulting in $\alpha = 0.5$. The value of $\alpha = 0.8$ we observe may hence indicate that the regime of multiple filament crossings is not yet reached over the distances probed by our simulation. We include an extrapolation of $A(\delta_{th}, d)$ up to a distance of 500 Mpc in Fig. 2, shown for two values of α, the observed one of $\alpha = 0.8$, and the expected one for large propagation distances, $\alpha = 0.5$. We expect that these two curves bracket the range of true deflections at $E \sim 4 \times 10^{19}$ eV.

We comment finally on the potential effect of the unclustered component of the IGMF, i.e., the field in voids and low-density regions outside clusters and filaments, the coherence length of which, l_c, is unconstrained by our simulations. If $l_c \ll d$ the proton trajectory makes a random walk through the magnetic domains, and the overall deflection is given by

$$\delta \simeq 0.2° \left(\frac{B_0}{E} \frac{4 \times 10^{19} \text{ eV}}{10^{-11} \text{ G}} \right) \left(\frac{d}{1 \text{ Gpc}} \right)^{\frac{1}{2}} \left(\frac{l_c}{1 \text{ Mpc}} \right)^{\frac{1}{2}}.$$

Hence, observable deflections are not produced by the unclustered component of the IGM if l_c is smaller than a few tens of Mpc. Note that such small coherence lengths are expected from most of the proposed generation mechanisms of seed IGMFs [13]. The few mechanisms predicting larger l_c generally give rise to MFs which are too weak to produce observable deflections of UECRs. Furthermore, an unclustered IGMF does not exist at all if the seed field is generated by a battery powered by structure formation [14].

CONCLUSIONS

We presented the first map of UECR deflections in the Local Universe that is based on a simulation that realistically reproduces the known large-scale structure around the Galaxy while simultaneously following the MHD amplification of MFs during cosmic structure formation. The positions and masses of the most prominent clusters are reproduced well in our simulation. This is an important advantage of our technique. Since local structures subtend large angles on the sky, it is important to be able to reliably identify "bad" regions of expected large deflections, a task that can be accomplished using our map, thereby providing important guidance for UECR source identification. Provided our basic hypothesis about the origin of IGMF is correct, our results should be understood as upper bounds for the expected deflection angles, because we have used the largest seed field still compatible with the RM in clusters, and secondly, we neglected UECR energy losses on the path to the detector. The actual observation of stronger deflections would imply that the evolution of the IGMF is not merely passive, possibly indicating a pollution of the IGM by physical process such as galactic winds.

We have also extrapolated the distribution of deflection angles to very large source distances in a statistical manner. Out to 500 Mpc and at $E \geq 4 \times 10^{19}$ eV, typical deflections are smaller than the angular resolution of current ground array UECR detectors over more than half of the sky (but may exceed the angular resolution of stereo fluorescent detectors). This result is consistent with an observed small-scale clustering of UECR arrival directions [20][1] and with evidence for a BL Lacs–UECR correlation [24] in the energy range $E \sim 4 \times 10^{19}$ eV being due to protons [25]. On the other hand, our results do not support models which invoke strong MFs in the Local Universe to solve the GZK anomaly as well as models which explain small-scale clustering by magnetic lensing.

We conclude that charged particle astronomy should in principle be possible regardless of the way the GZK problem is resolved.

REFERENCES

1. http://www.auger.org.
2. http://www.euso-mission.org.

---

[1] There is no clustering in the current HiRes data [21, 22], which became available after the submission of our paper. However, with the current statistics, there is no contradiction yet [22, 23].

3. K. Greisen, Phys. Rev. Lett. **16**, 748 (1966); G. T. Zatsepin and V. A. Kuzmin, Pis'ma Zh. Éksp. Teor. Fiz. **4**, 144 (1966) [JETP Lett. **4**, 99 (1966)].

4. D. J. Bird *et al.*, Astrophys. J. **441**, 144 (1995); M. Takeda *et al.*, Phys. Rev. Lett. **81**, 1163 (1998).

5. A. A. Mikhaĭlov, Pis'ma Zh. Éksp. Teor. Fiz. **79**, 175 (2004) [JETP Lett. **79**, 141 (2004)].

6. M. Ave, J. A. Hinton, R. A. Vazquez, *et al.*, Phys. Rev. Lett. **85**, 2244 (2000).

7. P. Tinyakov and I. Tkachev, astro-ph/0305363.

8. C. L. Carilli and G. B. Taylor, Ann. Rev. Astron. Astrophys. **40**, 319 (2002).

9. V. Berezinsky, A. Z. Gazizov, and S. I. Grigorieva, astro-ph/0210095.

10. P. Blasi and D. De Marco, astro-ph/0307067.

11. P. Blasi, S. Burles, and A. V. Olinto, Astrophys. J. **514**, L79 (1999).

12. K. Dolag, M. Bartelmann, and H. Lesch, Astron. Astrophys. **387**, 383 (2002).

13. D. Grasso and H. R. Rubinstein, Phys. Rep. **348**, 163 (2001).

14. R. M. Kulsrud, R. Cen, J. P. Ostriker, and D. Ryu, Astrophys. J. **480**, 481 (1997).

15. D. Ryu, H. Kang, and P. L. Biermann, Astron. Astrophys. **335**, 19 (1998).

16. G. Sigl, F. Miniati, and T. A. Ensslin, Phys. Rev. D **68**, 043002 (2003); astro-ph/0309695.

17. V. Springel, N. Yoshida, and S. D. M. White, New Astron. **6**, 79 (2001).

18. L. Anchordoqui, T. Paul, S. Reucroft, and J. Swain, Int. J. Mod. Phys. A **18**, 2229 (2003).

19. H. Mathis *et al.*, Mon. Not. R. Astron. Soc. **333**, 739 (2002).

20. N. Hayashida *et al.*, Phys. Rev. Lett. **77**, 1000 (1996); M. Takeda *et al.*, Astrophys. J. **522**, 225 (1999); P. G. Tinyakov and I. I. Tkachev, Pis'ma Zh. Éksp. Teor. Fiz. **74**, 3 (2001) [JETP Lett. **74**, 1 (2001)].

21. R. U. Abbasi *et al.* (The High Resolution Fly's Eye Collab., HIRES), astro-ph/0404137.

22. R. U. Abbasi *et al.* (The High Resolution Fly's Eye Collab., HIRES), astro-ph/0404366.

23. H. Yoshiguchi, S. Nagataki, and K. Sato, astro-ph/0404411.

24. P. G. Tinyakov and I. I. Tkachev, Pis'ma Zh. Éksp. Teor. Fiz. **74**, 499 (2001) [JETP Lett. **74**, 445 (2001)].

25. P. G. Tinyakov and I. I. Tkachev, Astropart. Phys. **18**, 165 (2002).

26. K. M. Gorski, E. Hivon, and B. D. Wandelt, in *Proceedings of the MPA/ESO Cosmology Conference Evolution of Large-Scale Structure*, Ed. by A. J. Banday, R. S. Sheth, and L. Da Costa (Print Partners Ipskamp, NL, 1999), p. 37; http://www.eso.org/science/healpix/.

$a_0^0(980)$–$f_0(980)$ Mixing and Spin Asymmetry in the $\pi^- p \longrightarrow \eta\pi^0 n$ Reaction

N. N. Achasov* and G. N. Shestakov

Laboratory of Theoretical Physics, Sobolev Institute of Mathematics, Siberian Division, Russian Academy of Sciences,
Universitetskiĭ pr. 4, Novosibirsk, 630090 Russia
* e-mail: achasov@math.nsc.ru
Received May 5, 2004

The mass difference between the K^+ and K^0 mesons induces mixing of the $a_0^0(980)$ and $f_0(980)$ resonances. The mixing amplitude is large, on the order of $m_K(m_{K^0}^2 - m_{K^+}^2)^{1/2} \approx \sqrt{\alpha} m_K^2$ near the $K\bar{K}$ thresholds, and its phase changes sharply by 90°. A high-energy experiment on the $\pi^- p \longrightarrow \eta\pi^0 n$ reaction in a polarized target is proposed. In this experiment, the presence of $a_0^0(980)$–$f_0(980)$ mixing can be unambiguously and simply identified by the presence of a large jump in the azimuthal asymmetry of the cross section for production of the $\eta\pi^0$ system in the S wave near the $K\bar{K}$ thresholds. Our estimates of the magnitude of the polarization effect, which is expected to be observed in the experiment, are almost model-independent. © 2004 MAIK "Nauka/Interperiodica".

PACS numbers: 13.75.Gx; 13.88.+e; 14.40.Cs

The determination of the nature of light scalar resonances is one of the main problems of nonperturbative QCD. Indeed, their nature is important for the understanding of basic consequences of QCD for hadron world: confinement physics and the way of realizing chiral asymmetry for low energies. Practically nobody refutes the nontrivial nature of well-identified light scalar resonances. In particular, there is much evidence of their four-quark ($q^2\bar{q}^2$) structure (see, e.g., [1] and references cited therein). In this work, a new method of studying the nature of $a_0(980)$ and $f_0(980)$ resonances in polarization experiments is proposed. This method is based on the $a_0^0(980)$–$f_0(980)$-mixing phenomenon, which, in particular, carries important information about the relation of these resonances to the $K\bar{K}$ channels.

The mixing of the $a_0^0(980)$ and $f_0(980)$ resonances was theoretically found as a threshold phenomenon in the late 1970s [2]. Interest in the $a_0^0(980)$–$f_0(980)$ mixing has recently been renewed [3–16]. However, the existence of this phenomenon has not yet been corroborated in direct experiment. This work presents a qualitatively new proposal on a search for the $a_0^0(980)$–$f_0(980)$-mixing effect. We propose a high-energy experiment on the $\pi^- p \longrightarrow \eta\pi^0 n$ reaction in a polarized tar-

get. In this experiment, the presence of the $a_0^0(980 - f_0(980)$ mixing can be unambiguously and simply identified by the presence of a large jump in the azimuthal (spin) asymmetry of the cross section for the production of the $\eta\pi^0$ system in the S wave near the $K\bar{K}$ thresholds.

In view of parity conservation, the differential cross section for the $\pi^- p \longrightarrow (\eta\pi^0)_S n$ reaction[1] on polarized protons with fixed momentum $P_{\text{lab}}^{\pi^-}$ of incident π^- mesons has the form

$$\frac{d^3\sigma}{dt\,dm\,d\psi} = \frac{1}{2\pi}\left(\frac{d^2\sigma}{dt\,dm} + I(t, m)P\cos\psi\right). \qquad (1)$$

Here, t is the square of the 4-momentum transfer from π^- to $\eta\pi^0$; m is the invariant mass of the $\eta\pi^0$ system; ψ is the angle between the normal to the reaction plane, formed by the momenta of the π^- meson and $\eta\pi^0$ system, and the proton polarization transverse to the π^- beam; P is the degree of this polarization; $d^2\sigma/dt\,dm = |M_{++}|^2 + |M_{+-}|^2$ is the cross section on unpolarized protons, where M_{++} and M_{+-} are the s-channel helicity amplitudes without and with the flip of the nucleon helicity; and $I(t, m) = 2\,\text{Im}(M_{++}M_{+-}^*)$ is the contribution

---

[1] The subscript S indicates that the $\eta\pi^0$ system has relative orbital angular momentum $L = 0$, i.e., is in the S wave.

responsible for the azimuthal asymmetry of a cross section. The dimensionless normalized asymmetry $A(t, m) = I(t, m)/[d^2\sigma/dtdm] - 1 \leq A(t, m) \leq 1$ is determined using the experimentally measured quantities $I(t, m)$ and $d^2\sigma/dtdm$. Asymmetry is related to a certain t interval or a certain m interval and is specified by the ratio of the corresponding integrals of $I(t, m)$ and $d^2\sigma/dtdm$ with respect to t or m, respectively. We are interested only in the range $m \approx 1$ GeV, where, according to the experiments on the $\pi^- p \longrightarrow \eta\pi^0 n$ reaction in nonpolarized targets for $P_{lab}^{\pi^-} =$ (BNL) 18.3 [3, 17, 18], (ITEP) 38 [19, 20], (IHEP) 32 [20], and (CERN) 100 [20] GeV, the production of the $a_0^0(980)$ resonance dominates the mass spectrum of the $(\eta\pi^0)_S$ system; i.e., $\pi^- p \longrightarrow a_0^0(980)n \longrightarrow (\eta\pi^0)_S n$.

In view of G-parity conservation, t-channel exchanges with the quantum numbers of the b_1 and ρ_2 Regge poles contribute to the M_{+-} and M_{++} amplitudes, respectively, for high energies and low $-t$ values [4]. We denote these amplitudes as $M_{+-}^{b_1}$ and $M_{++}^{\rho_2}$. The mixing of the a_0^0 and $f_0(980)$ resonances breaks G-parity conservation. Thus, exchange by the π Regge pole becomes possible in the $\pi^- p \longrightarrow (\eta\pi^0)_S n$ reaction due to the $\pi^- p \longrightarrow f_0(980)n \longrightarrow a_0^0(980)n \longrightarrow (\eta\pi^0)_S n$ process [2, 4].[2] As is known, the π-exchange amplitude is large for low $-t$ values. In addition, the absolute value and phase of the $a_0^0(980)$–$f_0(980)$ transition amplitude depend drastically on m near the $K\bar{K}$ thresholds. All these properties of the $\pi^- p \longrightarrow (\eta\pi^0)_S n$ reaction lead to important physical consequences, which can easily be observed in polarization experiments due to the unique possibility of observing the interference between the amplitudes of the ρ_2 and π exchanges.

We turn to quantitative estimates of the expected polarization effect. Virtually all information about the π-exchange amplitude M_{+-}^{π} breaking G parity is known, including its absolute normalization [2, 4, 21]:

$$M_{+-}^{\pi} = e^{-i\pi\alpha_\pi(t)/2} \frac{\sqrt{t}}{t - m_\pi^2} e^{\Lambda_\pi(t - m_\pi^2)/2}$$
$$\times a_\pi e^{i\delta_B(m)} G_{a_0 f_0}(m)[2m^2\Gamma_{a_0\eta\pi^0}(m)/\pi]^{1/2}. \quad (2)$$

Here, $\alpha_\pi(t) = \alpha_\pi(0) + \alpha'_\pi t \approx 0.8(t - m_\pi^2)/$GeV^2 is the π Regge-pole trajectory; $a_\pi = g_{\pi NN}g_{f_0\pi^+\pi^-}/\sqrt{8\pi}\, s$;

---

[2] This process can also proceed due to a_1 exchange. However, estimates based on [21] show that the corresponding amplitude $M_{++}^{a_1}$ is negligible compared to other contributions.

$g_{\pi NN}^2/4\pi \approx 14.3$; $g_{f_0\pi^+\pi^-}$ is the coupling constant of $f_0(980)$ with the $\pi^+\pi^-$ channel; $s \approx 2m_p P_{lab}^{\pi^-}$; $\Lambda_\pi/2 = \Lambda_\pi^0/2 + \alpha'_\pi \ln(s/s_0)$ is the residue slope; $s_0 = 1$ GeV^2; $\delta_B(m)$ is the smooth and large (about $90°$) phase of elastic background under the $f_0(980)$ resonance in the S-wave $\pi\pi \longrightarrow \pi\pi$ reaction in the channel with the isospin $I = 0$ [2, 21]; $G_{a_0 f_0}(m) = \Pi_{a_0 f_0}(m)/[D_{a_0}(m)D_{f_0}(m) - \Pi_{a_0 f_0}^2(m)]$, where the off-diagonal element $\Pi_{a_0 f_0}(m)$ of the polarization operator describes the $a_0^0(980)$–$f_0(980)$-transition amplitude [2]; $1/D_r(m)$ is the propagator of the nonmixed resonance $r = [a_0(980), f_0(980)]$ with mass m_r; $D_r(m) = m_r^2 - m^2 + \sum_{ab}[\text{Re}\Pi_r^{ab}(m_{f_0}) - \Pi_r^{ab}(m)]$; $ab = (\eta\pi^0, K^+K^-, K^0\bar{K}^0)$ and $(\pi^+\pi^-, \pi^0\pi^0, K^+K^-, K^0\bar{K}^0)$ for $r = a_0(980)$ and $f_0(980)$, respectively; the diagonal element $\Pi_r^{ab}(m)$ of the polarization operator of the resonance r corresponds to the contribution of the intermediate state ab [21]; and $\Gamma_{rab}(m) = \text{Im}[\Pi_r^{ab}(m)]/m = g_{rab}^2\rho_{ab}(m)/16\pi m$ is the $r \longrightarrow ab$ decay width, where g_{rab} is the coupling constant of r to the ab channel (here, $g_{f_0\pi^0\pi^0}^2 = g_{f_0\pi^+\pi^-}^2/2$), $\rho_{ab}(m) = [(m^2 - m_+^2)(m^2 - m_-^2)]^{1/2}/m^2$, and $m_\pm = m_a \pm m_b$. Since the $a_0^0(980)$ and $f_0(980)$ resonances are close to the $K\bar{K}$ thresholds and strongly coupled to the $K\bar{K}$ channels, the $a_0^0(980)$–$f_0(980)$-transition amplitude $\Pi_{a_0 f_0}(m)$ must be greatly determined by the contributions from the K^+K^- and $K^0\bar{K}^0$ intermediate states [2]. With allowance for isotopic symmetry of the coupling constants, the sum of the loop diagrams $f_0(980) \longrightarrow K^+K^- \longrightarrow a_0^0(980)$ and $f_0(980) \longrightarrow K^0\bar{K}^0 \longrightarrow a_0^0(980)$ gives [2]

$$\Pi_{a_0 f_0}(m) = \frac{g_{a_0 K^+K^-}g_{f_0 K^+K^-}}{16\pi}\left[i(\rho_{K^+K^-}(m) - \rho_{K^0\bar{K}^0}(m)) \right.$$
$$- \frac{\rho_{K^+K^-}(m)}{\pi}\ln\frac{1 + \rho_{K^+K^-}(m)}{1 - \rho_{K^+K^-}(m)}$$
$$\left. + \frac{\rho_{K^0\bar{K}^0}(m)}{\pi}\ln\frac{1 + \rho_{K^0\bar{K}^0}(m)}{1 - \rho_{K^0\bar{K}^0}(m)} \right], \quad (3)$$

where $m \geq 2m_{K^0}$ and $\rho_{K\bar{K}}(m)$ should be replaced by $i|\rho_{K\bar{K}}(m)|$ in the range $0 \leq m \leq 2m_K$. Figure 1 shows the resonance behavior of the (a) absolute value and (b) phase of expression (3). We note that, for the
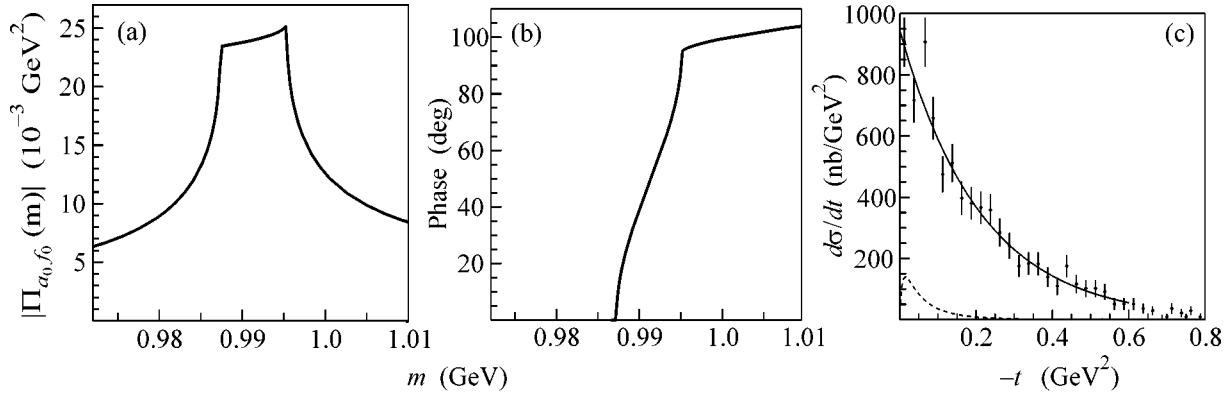
Fig. 1. (a) Absolute value and (b) phase of the $a_0^0(980)$–$f_0(980)$ transition amplitude given by Eq. (3); (c) the BNL data for $d\sigma/dt$ for the $\pi^- p \longrightarrow a_0^0(980)n \longrightarrow (\eta\pi^0)_S n$ reaction [3, 4] (footnote 2); the solid line is a fit of these data in the ρ_2-exchange model, and the dotted line is $d\sigma^\pi/dt$ for the $\pi^- p \longrightarrow f_0(980)n \longrightarrow a_0^0(980)n \longrightarrow (\eta\pi^0)_S n$ reaction related to the π exchange, for $P_{lab}^{\pi^-} = 18.3$ GeV.

8-MeV-wide m range between the K^+K^- and $K^0\bar{K}^0$ thresholds, $|\Pi_{a_0 f_0}(m)| \approx |g_{a_0 K^+ K^-} g_{f_0 K^+ K^-}/16\pi|[(m_{K^0}^2 - m_{K^+}^2)/m_{K^0}^2]^{1/2} \approx 0.1265|g_{a_0 K^+ K^-} g_{f_0 K^+ K^-}/16\pi|$, which is equal in order of magnitude to $m_K(m_{K^0}^2 - m_{K^+}^2)^{1/2} \approx \sqrt{\alpha} m_K^2$. From Eqs. (2) and (3), it also follows that the contribution of the M_{+-}^π amplitude to $d^2\sigma/dtdm$ in this range is primarily determined by the product of the ratios of coupling constant squared; i.e., $|M_{+-}^\pi|^2 \propto (\pi^+\pi^- \longrightarrow \eta\pi^0) \propto (g_{f_0 K^+ K^-}^2/g_{f_0 \pi^+ \pi^-}^2)(g_{a_0 K^+ K^-}^2/g_{a_0 \eta\pi^0}^2)$.

Using the Regge-pole model, we write the $M_{+-}^{b_1}$ and $M_{++}^{\rho_2}$ amplitudes in the form

$$M_{+-}^{b_1} = ie^{-i\pi\alpha_{b_1}(t)/2}\sqrt{-t}\,e^{\Lambda_{b_1}t/2}(s/s_0)^{\alpha_{b_1}(0)-1}$$
$$\times a_{b_1}G_{a_0}(m)[2m^2\Gamma_{a_0\eta\pi^0}(m)/\pi]^{1/2}, \tag{4}$$

$$M_{++}^{\rho_2} = e^{-i\pi\alpha_{\rho_2}(t)/2}e^{\Lambda_{\rho_2}t/2}(s/s_0)^{\alpha_{\rho_2}(0)-1}$$
$$\times a_{\rho_2}G_{a_0}(m)[2m^2\Gamma_{a_0\eta\pi^0}(m)/\pi]^{1/2}. \tag{5}$$

Here, $\alpha_j(t) = \alpha_j(0) + \alpha_j' t$, a_j, and $\Lambda_j/2 = \Lambda_j^0/2 = \alpha_j' \ln(s/s_0)$ are the trajectory, residue, and the residue slope of the jth Regge pole, respectively [one can approximately take $\alpha_{b_1}(t) \approx -0.21 + 0.8t/\text{GeV}^2$ and $\alpha_{\rho_2}(t) \approx -0.31 + 0.8t/\text{GeV}^2$], and $G_{a_0}(m) = D_{f_0}(m)/[D_{a_0}(m)D_{f_0}(m) - \Pi_{a_0 f_0}^2(m)]$ is the propagator

of the $a_0^0(980)$ resonance with allowance for mixing [2]. The real situation is very interesting. The available BNL [3], IHEP [19, 20], and CERN [20] data on the t distributions of $\pi^- p \longrightarrow a_0^0(980)n \longrightarrow (\eta\pi^0)_S n$ events integrated with respect to m near the $a_0^0(980)$ peak formally do not require the introduction of the b_1-exchange amplitude. In the range $0 \le -t \le (0.6{-}0.8)$ GeV^2, all these data are well approximated by the simple exponential $C\exp(\Lambda t)$ [4, 19, 20], which implies that they can be described by using only the $M_{++}^{\rho_2}$ amplitude nonvanishing at $t \longrightarrow 0$ [4]. For example, the corresponding fit of the normalized BNL data [3] on the differential cross section $d\sigma/dt$ for the $\pi^- p \longrightarrow a_0^0(980)n \longrightarrow (\eta\pi^0)_S n$ reaction (see Fig. 1c)[3] gives $\chi^2/n.d.f = 15.75/22$ and $d\sigma/dt = [(945.8 \pm 46.3) \text{ nb/GeV}^2]\exp[t(4.729 \pm 0.217)/\text{GeV}^2]$. Therefore, it is natural to estimate first the contributions only from the ρ_2 and π exchange mechanisms.

The dotted line in Fig. 1c shows the differential cross section $d\sigma^\pi/dt = \int|M_{+-}^\pi|^2 dm$ caused by the π exchange and corresponding to the range $0.8 \le m \le 1.2$ GeV

---

[3] Experimental points in Fig. 1c are the BNL dN/dt data for $P_{lab}^{\pi^-} = 18.3$ GeV [3], which are normalized to the cross section for $a_2^0(1320)$ formation in the $\pi^- p \longrightarrow a_2^0(1320)n$ reaction, as was done in [4]. According to the estimate obtained in [4], the total cross section for the $\pi^- p \longrightarrow a_0^0(980)n \longrightarrow (\eta\pi^0)_S n$ reaction at 18.3 GeV is approximately equal to 200 nb. We attribute this value to the m range from 0.8 to 1.2 GeV and to the entire range $t \le 0$. Note that this value agrees well with the estimate given for σ in [19].
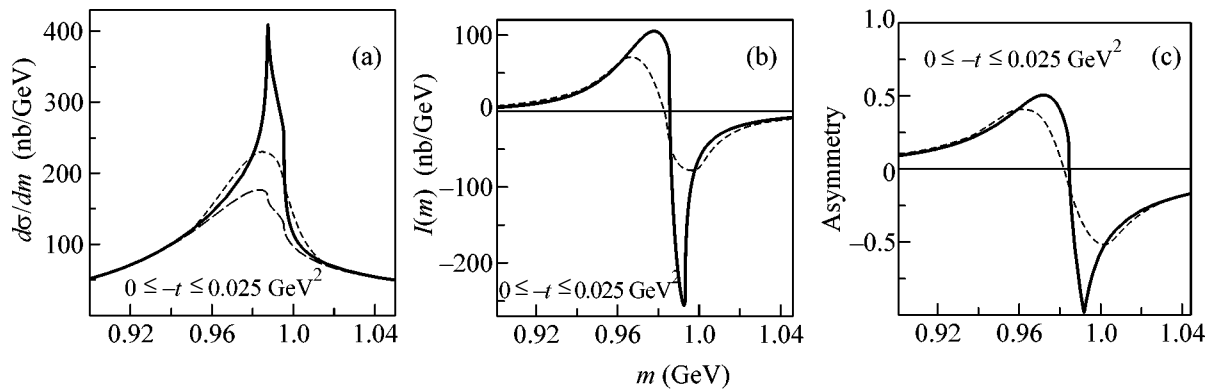
Fig. 2. Manifestation of the $a_0^0(980)$–$f_0(980)$ mixing in the $\pi^- p \longrightarrow a_0^0(980)n \longrightarrow (\eta\pi^0)_S n$ reaction on a polarized target for $P_{\text{lab}}^{\pi^-} = 18.3$ GeV in the model including the ρ_2 and π exchanges. The solid lines are (a) $d\sigma/dm$ and (b) $I(m)$ for $0 \le -t \le 0.025$ GeV^2 and (c) the corresponding asymmetry A $(0 \le -t \le 0.025$ GeV^2, m). The common sign of $I(m)$ and asymmetry is taken arbitrarily. The long-dashed line in (a) is the ρ_2-exchange contribution. The short-dashed lines are (a) $d\sigma/dm$ and (b) $I(m)$ smoothed using Gaussian distribution in m with a dispersion of 10 MeV and (c) the corresponding asymmetry.

and $P_{\text{lab}}^{\pi^-} = 18.3$ GeV, i.e., to the BNL energy for which $\Lambda_\pi/2 \approx 4.5$ GeV^{-2} [22, 23]. When drawing this line for $d\sigma^\pi/dt$, quantity $|\Pi_{a_0 f_0}(m)|$ in Fig. 1a, and lines in Fig. 2 illustrating the expected polarization effect, we use the following approximate parameters of the $f_0(980)$ and $a_0(980)$ resonances: $m_{f_0} \approx 0.980$ GeV, $g_{f_0\pi^+\pi^-}^2/16\pi \approx \frac{2}{3} 0.1$ GeV^2, $g_{f_0 K^+K^-}^2/16\pi \approx \frac{1}{2} 0.4$ GeV^2, $\delta_B(m) \approx 35.5° + 47°m$/GeV, $m_{a_0} \approx 0.9847$ GeV, $g_{a_0 K^+K^-}^2/16\pi \approx$ $g_{f_0 K^+K^-}^2/16\pi \approx \frac{1}{2} 0.4$ GeV^2, and $g_{a_0\eta\pi^0}^2/16\pi \approx 0.25$ GeV^2; see, additionally, [2, 21, 24–28]. We note that the sharp 90° change in the phase of the amplitude $\Pi_{a_0 f_0}(m)$ between the $K\overline{K}$ thresholds, which is of crucial importance for the polarization phenomena, is independent of the parameters of the $f_0(980)$ and $a_0^0(980)$ resonances (see Fig. 1b and Eq. (3)). The integration of $d\sigma^\pi/dt$ with respect to t yields $\sigma^\pi \approx 10.9$ nb; i.e., the π-exchange contribution to the total cross section for the $\pi^- p \longrightarrow$ $a_0^0(980)n \longrightarrow (\eta\pi^0)_S n$ reaction, which is approximately equal to 200 nb for 18.3 GeV [4], is equal to about 5.5%. We emphasize that the indicated value of cross section σ^π should be treated as a very reliable lower estimate [2, 4]. The cross section $d\sigma^\pi/dt$ at the maximum positioned at $t \approx -0.0149$ GeV^2 is approximately equal to 139 nb/GeV^2, comprises approximately 14.7% of $(d\sigma/dt)|_{t \approx 0}$ (Fig. 1c). However, the main conclusion is that virtually the whole $d\sigma^\pi/dt$ value comes from the narrow m range near the $K\overline{K}$ thresholds

(Fig. 1a), whereas the total cross section $d\sigma/dt$ comes from the integration over an m range that is at least an order of magnitude wider. Thus, for low $-t$ values and m values near the $K\overline{K}$ thresholds, the π-exchange contribution can be comparable with the basic ρ_2-exchange contribution allowed in G parity. Figure 2 shows $d\sigma/dm = \int [|M_{++}^{\rho_2}|^2 + |M_{+-}^\pi|^2] dt$, $d\sigma^{\rho_2}/dm = \int |M_{++}^{\rho_2}|^2 dt$, and $I(m) = \int I(t, m) dt = \int 2\text{Im}[M_{++}^{\rho_2}(M_{+-}^\pi)^*] dt$ for $P_{\text{lab}}^{\pi^-} = 18.3$ GeV to $-t$ values from 0 to 0.025 GeV^2, as well as the corresponding asymmetry A $(0 \le -t \le 0.025$ GeV^2, $m)$. The parameters of the ρ_2 exchange, which are substituted into Eq. (5), correspond to the fit of the BNL data discussed above (Fig. 1c). Since the relative sign of the ρ_2 and π exchanges is unknown, $I(m)$ and asymmetry are determined except for the sign. As is seen in Fig. 2, the polarization effect due to the interference between the $M_{++}^{\rho_2}$ and M_{+-}^π amplitudes is large. It can be measured by the characteristic jump of asymmetry in the m range from 0.965 to 1.01 GeV. The corresponding difference between the maximal and minimal values of asymmetry, which is smoothed due to finite resolution in m (see caption to Fig. 2), is equal to 0.95 (Fig. 2c). We note that the obtained pattern does not noticeably change if the BNL data shown in Fig. 1c are refitted such that the fixed pion-exchange contribution shown in this figure is added to the ρ_2-exchange contribution. We illustrate the effect only in the $-t$ range from 0 to 0.025 GeV^2 for brevity. Figures similar to Fig. 2 were drawn for ranges $0 \le -t \le 0.05$, 0.1, and 0.2 GeV^2, where the relative value of the polarization effect remains virtually unchanged. Moreover, we carefully examined the situation arising when a b_1-exchange contribution of up to 40% of the total reaction cross section

is included. However, even in this case, the b_1-exchange contribution is immaterial for low $-t$ values. The main conclusion for this range is that the asymmetry relating to any of the ranges $0 \leq -t \leq 0.025, \ldots, 0.1$ GeV^2 shows a jump by a value close to 1 in the m range from 0.965 to 1.01 GeV owing to the π-exchange admixture.

We emphasize that the detection of an asymmetry jump does not require high resolution in the invariant mass of the $\eta\pi^0$ system, which would be absolutely necessary for the detection of the manifestation of the $a_0^0(980)$–$f_0(980)$ mixing in the $\eta\pi^0$ mass spectrum in experiments with nonpolarized targets.

At present, experiments with polarized beams and targets are on the rise. Therefore, the above proposal seems to be opportune. Due to the closeness of the π, ρ_2, and b_1 Regge trajectories, the indicated polarization effect can be studied for any high energy, e.g., in the range from 8 to 100 GeV. The corresponding experiments on the $\pi^- p \longrightarrow \eta\pi^0 n$ reaction on polarized protons can be carried out at KEK, BNL, IHEP, CERN (COMPASS), ITEP, FNAL, and Institut für Kernphysik (Jülich). The observation of the $a_0^0(980)$–$f_0(980)$ mixing would open one more interesting page in the investigation of the mysterious $a_0^0(980)$ and $f_0(980)$ states. The general concept of using polarization phenomena as an effective tool for the observation of the $a_0^0(980)$–$f_0(980)$ mixing is based on a large change ($\approx 90°$) in the phase of the $a_0^0(980)$–$f_0(980)$-transition amplitude in a narrow m range (8 MeV) between the K^+K^- and $K^0\bar{K}^0$ thresholds and naturally applies to other reactions.

REFERENCES

1. N. N. Achasov, Nucl. Phys. A **728**, 425 (2003); Yad. Fiz. **65**, 573 (2002) [Phys. At. Nucl. **65**, 546 (2002)].

2. N. N. Achasov, S. A. Devyanin, and G. N. Shestakov, Phys. Lett. B **88**, 367 (1979); Yad. Fiz. **33**, 1337 (1981) [Sov. J. Nucl. Phys. **33**, 715 (1981)]; Usp. Fiz. Nauk **142**, 361 (1984) [Sov. Phys. Usp. **27**, 161 (1984)].

3. A. R. Dzierba, in *Proceedings of the Second Workshop on Physics and Detectors for DAΦNE'95, Frascati, 1995*, Ed. by R. Baldini *et al.* (INFN, Frascati, 1996), Frascati Phys. Ser., Vol. 4, p. 99.

4. N. N. Achasov and G. N. Shestakov, Phys. Rev. D **56**, 212 (1997).

5. O. Krehl, R. Rapp, and J. Speth, Phys. Lett. B **390**, 23 (1997).

6. B. Kerbikov and F. Tabakin, Phys. Rev. C **62**, 064601 (2000).

7. F. E. Close and A. Kirk, Phys. Lett. B **489**, 24 (2000).

8. A. E. Kudryavtsev and V. E. Tarasov, Pis'ma Zh. Éksp. Teor. Fiz. **72**, 589 (2000) [JETP Lett. **72**, 410 (2000)].

9. V. Yu. Grishina *et al.*, Phys. Lett. B **521**, 217 (2001).

10. N. N. Achasov and A. V. Kiselev, Phys. Lett. B **534**, 83 (2002).

11. D. Black, M. Harada, and J. Schechter, Phys. Rev. Lett. **88**, 181603 (2002).

12. A. E. Kudryavtsev, V. E. Tarasov, J. Haidenbauer, *et al.*, Phys. Rev. C **66**, 015207 (2002); Yad. Fiz. **66**, 1994 (2003) [Phys. At. Nucl. **66**, 1946 (2003)].

13. M. Buescher *et al.*, hep-ph/0301126.

14. L. A. Kondratyuk, E. L. Bratkovskaya, V. Yu. Grishina, *et al.*, Yad. Fiz. **66**, 155 (2003) [Phys. At. Nucl. **66**, 152 (2003)].

15. C. Hanhart, in *Scalar Mesons: An Interesting Puzzle for QCD, Utica, N.Y., 2003*, Ed. by A. H. Fariborz (AIP, Melvill, N.Y., 2003), AIP Conf. Proc., Vol. 688, p. 61.

16. M. Buescher, nucl-ex/0311018; nucl-ex/0401010.

17. S. Teige *et al.*, Phys. Rev. D **59**, 012001 (1999).

18. A. R. Dzierba *et al.*, Phys. Rev. D **67**, 094015 (2003).

19. S. A. Sadovsky, in *Proceedings of Seventh International Conference on Hadron Spectroscopy, Upton, N.Y., 1997*, Ed. by S. U. Chung and H. J. Willutzki (AIP, Woodbury, N.Y., 1998), AIP Conf. Proc., Vol. 432, p. 774.

20. D. Aldi *et al.,* Yad. Fiz. **62**, 462 (1999) [Phys. At. Nucl. **62**, 421 (1999)].

21. N. N. Achasov and G. N. Shestakov, Phys. Rev. D **58**, 054011 (1998); N. N. Achasov, S. A. Devyanin, and G. N. Shestakov, Yad. Fiz. **32**, 1098 (1980) [Sov. J. Nucl. Phys. **32**, 566 (1980)].

22. J. Gunter *et al.*, Phys. Rev. D **64**, 072001 (2001).

23. N. N. Achasov and G. N. Shestakov, Phys. Rev. D **67**, 114018 (2003).

24. K. Hagiwara *et al.* (Particle Data Group), Phys. Rev. D **66**, 010001 (2002).

25. A. D. Martin, E. N. Ozmutlu, and E. J. Squires, Nucl. Phys. B **121**, 514 (1977).

26. N. N. Achasov, S. A. Devyanin, and G. N. Shestakov, Phys. Lett. B **96**, 168 (1980).

27. N. N. Achasov and V. V. Gubin, Phys. Rev. D **63**, 094007 (2001); N. N. Achasov and A. V. Kiselev, Phys. Rev. D **68**, 014006 (2003).

28. P. Colangelo and F. De Fazio, Phys. Lett. B **559**, 49 (2003).

Translated by R. Tyapaev

Radiative Muon Pair Production in High-Energy Electron–Positron Annihilation Process¶

A. B. Arbuzov, V. V. Bytev, and E. A. Kuraev*

Joint Institute for Nuclear Research, Dubna, 141980 Russia
*e-mail: kuraev@thsun1.jinr.ru
Received May 5, 2004

The lowest order radiative correction to the differential cross section of process of muon pair production with the emission of a hard photon at high energy electron–positron annihilation are calculated. Taking into account the emission of additional soft and hard photon, the cross section can be put in the form of the Drell–Yan process in leading logarithmical approximation. Applying the crossing transformation, we obtain the cross section of the radiative electron–muon high-energy scattering process. Virtual and soft photon emission contributions of the nonleading form are tabulated for several typical kinematical points. The limit of the small invariant mass of a muon pair is in agreement with our previous analysis. © 2004 MAIK "Nauka/Interperiodica".

PACS numbers: 13.66.De; 13.66.Lm; 13.40.-f

The process of muon pair production, as well as radiative muon pair production, at high energy in electron–positron collisions is commonly used for calibration purposes. This process was investigated in detail in the Born approximation in a series of papers of Baier and Khoze [1], where the mechanism of returning to resonant region was found.

One of the motivations of our investigation is the high theoretical accuracy required for the description of the differential cross section. Additional interest appears in the case of small invariant mass of the muon pair. For this case the radiative muon pair production is provided for by the initial state hard photon emission kinematics. It can be used as a calibration process in studying the hadronic systems of small invariant masses created by a virtual photon. The lowest order radiative corrections (RCs) in that kinematics to the Born cross section as well as the leading logarithmic (LL) and next-to-leading (NL) contributions in all orders of perturbation theory (PT), were considered in our recent paper [2].

Besides the practical applications [3, 4], we pursue another aim in this paper. The problem is to check the validity renormalization group (RG) predictions concerning hard processes of type $2 \longrightarrow 3$.

Basing on exact (with power accuracy $O(M_\mu^2/s)$) calculations, we confirm the Drell–Yan form of the cross section of radiative muon pair production in LL. Estimation of nonleading contributions for several kinematics points are given as well.

¶This article was submitted by the authors in English.

In conclusion, we set the cross section for crossing processes: radiative electron–muon scattering and muon pair production by photon on electron in LL.

1. Born cross section and RC. In this paper, for the process

$$e^+(p_+) + e^-(p_-) \longrightarrow \mu^+(q_+) + \mu^-(q_-) + \gamma(k_1) \quad (1)$$

we use the following kinematics:

$$\chi_\pm = 2k_1 p_\pm, \quad \chi'_\pm = 2k_1 q_\pm, \quad s = (p_- + p_+)^2,$$

$$s_1 = (q_- + q_+)^2, \quad t = (p_- - q_-)^2, \quad t_1 = (p_+ - q_+)^2,$$
$$u = (p_- - q_+)^2, \quad u_1 = (p_+ - q_-)^2, \quad (2)$$

$$p_\pm^2 = m^2, \quad q_\pm = M^2,$$

where $M(m)$ is muon (electron) mass. Here, all kinematical invariants are much larger than the muon (electron) mass, but we take into account terms of order $\ln(M/m)$:

$$s_1 \sim s \sim -t \sim -t_1 \sim -u \sim -u_1 \sim \chi_\pm \gg M^2 \gg m^2, \quad (3)$$
$$s + s_1 + t + t_1 + u + u_1 = 0.$$

The differential cross section of the process with the lowest order RC has the form

$$\frac{d\sigma_0}{d\Gamma} = \frac{\alpha^3}{2\pi^2 s} m_0 \left[1 + \frac{\alpha}{\pi}(\Delta_{\text{vac}} + \Delta_{ff} + \Delta_{\text{vert}} + \Delta_{\text{box}} + \Delta_{\text{soft}}) \right],$$

$$d\Gamma = \frac{d^3 q_+ d^3 q_- d^3 k_1}{\varepsilon_+ \varepsilon_- \omega_1} \delta^4(p_+ + p_- - q_+ - q_- - k_1). \quad (4)$$

It's convenient to separate starting from the Born level definite contributions from hard photon emission by electron and muon block and their interference:

$$m_0 = m_0^e + m_0^\mu + m_0^{\text{int}}, \tag{5}$$

where [5]

$$m_0^e = A\frac{s}{\chi_-\chi_+}, \quad m_0^\mu = A\frac{s_1}{\chi_-'\chi_+'}, \tag{6}$$

$$m_0^{\text{int}} = A\left[-\frac{t}{\chi_-\chi_-'} - \frac{t_1}{\chi_+\chi_+'} + \frac{u_1}{\chi_+\chi_-'} + \frac{u}{\chi_-\chi_+'}\right],$$

$$A = \frac{t^2 + t_1^2 + u^2 + u_1^2}{ss_1}.$$

The standard evaluation of additional soft photon emission contribution gives [6]

$$\frac{d\sigma_{\text{soft}}}{d\sigma_0} = -\frac{\alpha}{4\pi^2}\int\frac{d^3k_2}{\omega_2}$$

$$\times\left(-\frac{p_-}{p_-k_2} + \frac{p_+}{p_+k_2} + \frac{q_-}{q_-k_2} - \frac{q_+}{q_+k_2}\right)^2\Bigg|_{\omega_2 < \Delta\varepsilon \ll \varepsilon} \tag{7}$$

$$= \frac{\alpha}{\pi}(\Delta_s^e + \Delta_s^\mu + \Delta_s^{\text{int}}) = \frac{\alpha}{\pi}\Delta_{\text{soft}}.$$

Here, we denote

$$\Delta_s^e = 2(\rho_s + L - 1)\ln\frac{m\Delta\varepsilon}{\lambda\varepsilon} + \frac{1}{2}(\rho_s + L)^2 - \frac{\pi^2}{3},$$

$$\Delta_s^\mu = 2(\rho_{s1} - L - 1)\ln\frac{M\Delta\varepsilon}{\lambda\sqrt{\varepsilon_+\varepsilon_-}} + \frac{1}{2}(\rho_{s1} - L)^2$$

$$-\frac{1}{2}\ln^2\frac{\varepsilon_+}{\varepsilon_-} - \frac{\pi^2}{3} + \text{Li}_2\left(\frac{1+c}{2}\right),$$

$$\Delta_s^{\text{int}} = \frac{1}{2}(\rho_{t_1} + \rho_u)\ln\frac{t_1}{u} + \frac{1}{2}(\rho_t + \rho_{u_1})\ln\frac{t}{u_1} \tag{8}$$

$$+ 2\ln\frac{t_1}{u}\ln\frac{\sqrt{mM}\Delta\varepsilon}{\lambda\sqrt{\varepsilon\varepsilon_+}} + 2\ln\frac{t}{u_1}\ln\frac{\sqrt{mM}\Delta\varepsilon}{\lambda\sqrt{\varepsilon\varepsilon_-}}$$

$$+ \text{Li}_2\left(\frac{1+c_-}{2}\right) + \text{Li}_2\left(\frac{1-c_+}{2}\right) - \text{Li}_2\left(\frac{1+c_+}{2}\right) - \text{Li}_2\left(\frac{1-c_+}{2}\right),$$

where

$$L = \ln\frac{M}{m}, \quad \rho_\lambda = \ln\frac{mM}{\lambda^2}, \quad \rho_s = \ln\frac{s}{mM},$$

$$\rho_{s_1} = \ln\frac{s_1}{mM}, \quad \rho_t = \ln\frac{-t}{mM}, \quad \rho_{t_1} = \ln\frac{-t_1}{mM},$$

$$\rho_u = \ln\frac{-u}{mM}, \quad \rho_{u_1} = \ln\frac{-u_1}{mM}, \tag{9}$$

$$\text{Li}_2(z) = -\int_0^z\frac{dx}{x}\ln(1-x),$$

$$c_\pm = \cos(\mathbf{p}_-\mathbf{q}_\pm), \quad c = \cos(\mathbf{q}_+\mathbf{q}_-),$$

and ε, $\varepsilon_\pm$ are the energies (in cms) of electron and muon and λ is "photon mass."

Let us now consider RCs arising from the Dirac form factor of leptons and vacuum polarization (the Pauli form factor contribution is suppressed in our kinematics). They are

$$\Delta_{ff} + \Delta_{\text{vac}} = \frac{2m_0^e + m_0^{\text{int}}}{m_0}\left(\text{Re}\,\Gamma\left(\frac{s_1}{M^2}\right) + \text{Re}\,\Pi(s_1)\right)$$

$$+ \frac{2m_0^\mu + m_0^{\text{int}}}{m_0}\left(\text{Re}\,\Gamma\left(\frac{s}{m^2}\right) + \text{Re}\,\Pi(s)\right) \tag{10}$$

with [6]

$$\text{Re}\,\Gamma\left(\frac{s}{m^2}\right) = \left(\ln\frac{m}{\lambda} - 1\right)(1 - \rho_s - L)$$

$$-\frac{1}{4}(\rho_s + L)^2 - \frac{1}{4}(\rho_s + L) + \frac{\pi^2}{3},$$

$$\text{Re}\,\Gamma\left(\frac{s_1}{M^2}\right) = \left(\ln\frac{M}{\lambda} - 1\right)(1 - \rho_{s_1} + L)$$

$$-\frac{1}{4}(\rho_{s_1} - L)^2 - \frac{1}{4}(\rho_{s_1} - L) + \frac{\pi^2}{3}, \tag{11}$$

$$\text{Re}\,\Pi(s_i) = \text{Re}\,\Pi^e(s_j) + \text{Re}\,\Pi^\mu(s_j)$$

$$+ \text{Re}\,\Pi^\tau(s_j) + \text{Re}\,\Pi^h(s_j),$$

$$\text{Re}\,\Pi^e(s_j) = \frac{1}{3}(\rho_{s_j} + L) - \frac{5}{9},$$

$$\text{Re}\,\Pi^\mu(s_j) = \frac{1}{3}(\rho_{s_j} - L) - \frac{5}{9}.$$

Here, s_j is the kinematical invariant s or s_1. The contributions from the vacuum polarization from the heavy lepton τ and hadrons Π^τ, Π^h are given in [7].

2. Calculations of box-type RCs. Consider now amplitudes arising from box-type Feynman Diagrams (FDs). There are twelve such FDs, or 48 squared matrix elements. In calculation we restrict ourselves to consideration of only three box-type FDs. Really, the total contribution of interference of box-type and Born amplitudes can be expressed in the form

$$\text{Re}\,\Sigma M_{\text{box}}M_0^*$$

$$= (1 + P_1)[(1 - P_2)B^e(M_0^e)^* + (1 + P_2)B^e(M_0^\mu)^*], \tag{12}$$

where $M_0^e + M_0^\mu = M_0$, $M_0^e(M_0^\mu)$ are electron (muon) block emission part of the Born matrix element, and B^e
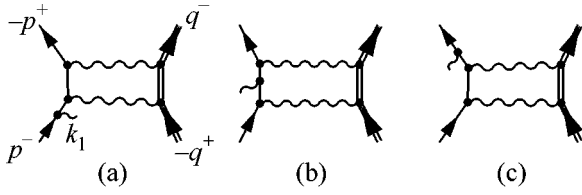
Fig. 1. Set of box-type FDs used in calculation.

is the electron emission part of contribution to the box-type amplitude with uncrossed photon legs (see Fig. 1). Note that, calculating the B^e, we must consider the pentagon-type FD (see Fig. 1b) and two remaining ones (see FD Figs. 1a, 1c).

The substitution operators $P_{1,2}$ work as

$$P_1 f(p_+, p_-; q_+, q_-, k_1) = f(q_+, q_-; p_+, p_-; -k_1);$$
$$P_2 f(p_+, p_-; q_+, q_-, k_1) = f(p_+, p_-; q_-, q_+; k_1). \quad (13)$$

The operator P_1 "changes" the photon emission from electron line to muon line. The application of operator P_2 makes it possible to obtain the contribution from FD in Fig. 1 FD with crossed virtual photon lines. As a result we obtain

$$\Delta_{\text{box}} = -(\rho_s + \rho_\lambda) \ln \frac{tt_1}{uu_1} + \Delta_B^{NL}. \quad (14)$$

The expression for Δ_B^{NL} is rather cumbersome. The whole contribution to Δ_{NL} (which does not contains large logarithms) would be given in form of the table below.

3. Vertex-type FDs. Let now consider the contribution arising from FDs with vertex-type insertions V^e (see Fig. 2). The other vertex contributions appear from these by using substitutions

$$\text{Re}\Sigma M_{\text{vert}} M_0^* = (1 + P_1)(1 + P_3) V^e (M_0^e)^*, \quad (15)$$

with operator P_3 denned as

$$P_3 f(p_+, p_-; q_+, q_-, k_1) = f(p_-, p_+; q_+, q_-;, k_1). \quad (16)$$

The total answer for vertex-type contribution reads

$$\Delta_{\text{vert}} = -\frac{1}{2} \frac{m_e + \frac{1}{2} m_i}{m_0} [(\rho_s + L)^2$$
$$+ 2(\rho_s + L)(\rho_\lambda + L) - 3(\rho_s + L) + \Delta_v^{NL}(s)]$$
$$- \frac{1}{2} \frac{m_\mu + \frac{1}{2} m_i}{m_0} [(\rho_{s_1} - L)^2 \quad (17)$$
$$+ 2(\rho_{s_1} - L)(\rho_\lambda - L) - 3(\rho_{s_1} - L) + \Delta_v^{NL}(s_1)].$$

4. Master formula. Extracting the explicate dependence on vacuum polarization in the form $1/|1 - \Pi|^2$ and
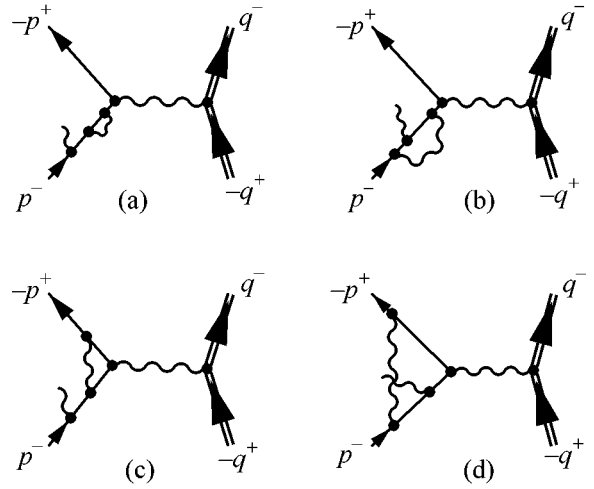

Fig. 2. Set of vertex FDs used in our calculation.

collecting the leading and nonleading terms arising from soft photon emission, vertex and box-type FD contributions, as well as lepton form factors, we arrive at the formula

$$\Delta_{\text{soft}} + \Delta_{\text{box}} + \Delta_{\text{vert}} + \Delta_{ff} = \Delta_{\text{lead}} + \Delta_{NL}. \quad (18)$$

This expression is free from the infrared singularities, as well as from squares of large logarithms. The form of Δ_{lead} is consistent with renormalization group prescriptions,

$$1 + \frac{\alpha}{\pi} \Delta_{\text{lead}} = \left(1 + \frac{\alpha}{2\pi} \ln \frac{s}{m_e^2} P_\Delta(\varepsilon)\right)^2$$
$$+ \left(1 + \frac{\alpha}{2\pi} \ln \frac{s_1}{M^2} P_\Delta(\varepsilon_+)\right)\left(1 + \frac{\alpha}{2\pi} \ln \frac{s_1}{M^2} P_\Delta(\varepsilon_-)\right) + O(\alpha^2), \quad (19)$$

with P_Δ being the δ part of the kernel of the evolution equation,

$$P_\Delta(\varepsilon) = 2 \ln \frac{\Delta\varepsilon}{\varepsilon} + \frac{3}{2},$$
$$P_\Delta(\varepsilon_\pm) = 2 \ln \frac{\Delta\varepsilon}{\varepsilon_\pm} + \frac{3}{2}. \quad (20)$$

Numerical estimation of the Δ_{NL} part of the K factor excluding nonleading terms arising from hard noncollinear photon emission (which depends on experimental setups) and the terms proportional to $\ln\Delta\varepsilon/\varepsilon$, $\ln\Delta\varepsilon/\varepsilon_\pm$ arising from soft photon emission

N	e_-	e_+	c_-	c_+	Δ_{NL}
1	0.59	0.66	0.29	−0.66	6.77
2	0.67	0.67	0.50	0.30	3.24
3	0.68	0.65	0.69	−0.50	8.68
4	0.59	0.56	−0.30	−0.30	8.35

An additional hard photon emission contribution in leading logarithmical order can be taken into account using the quasi-real electron method [8]. It results in the replacement P_2 by the whole kernel of evolution equation of twist 2 operators

$$P(z) = P^{(1)}(z) = \lim_{\Delta \to 0}[P_\Delta \delta(1-z) + P_\Theta(z)],$$

$$P_\Delta = 2\ln\Delta + \frac{3}{2}, \quad P_\Theta(z) = \Theta(1-\Delta-z)\frac{1+z^2}{1-z}. \quad (21)$$

As a result we arrive at the compact form of the cross section

$$\frac{d\sigma^{e^+e^- \to \mu^+\mu^-\gamma}(p_-, p_+, q_-, q_+, k_1)}{d\Gamma}$$

$$= \int\limits_{x_m}^1 dx_1 \int\limits_{x_m}^1 dx_2 \int\limits_{y_-}^1 \frac{dz_-}{z_-} \int\limits_{y_+}^1 \frac{dz_+}{z_+} D_e(x_1, s) D_e(x_2, s)$$

$$\times D_\mu\left(\frac{y_-}{z_-}, s_1\right) \times D_\mu\left(\frac{y_+}{z_+}, s_1\right) \frac{\left(1+\frac{\alpha}{\pi}K\right)}{|1-\Pi(sx_1x_2)|^2} \quad (22)$$

$$\times \frac{d\sigma^{e^+e^- \to \mu^+\mu^-\gamma}(x_1p_-, x_2p_+, Q_-, Q_+, k_1)}{d\Gamma_1},$$

$$Q_\pm = \frac{z_\pm}{y_\pm}q_\pm, \quad y_\pm = \frac{\varepsilon_\pm}{\varepsilon},$$

and the structure functions $D(x, s)$ having the standard form [9]

$$D_e(x, s) = \delta(1-x) + \frac{\alpha}{2\pi}P^{(1)}(x)\ln\frac{s}{m^2} + \dots,$$

$$D_\mu(y, s_1) = \delta(1-y) + \frac{\alpha}{2\pi}P^{(1)}(y)\ln\frac{s_1}{M^2} + \dots. \quad (23)$$

The phase volumes entering the left and right parts of the master equation are different:

$$d\Gamma = \frac{d^3q_-d^3q_+d^3k_1}{\varepsilon_-\varepsilon_+\omega_1}\delta(p_+ + p_- - q_+ - q_- - k_1),$$

$$d\Gamma_1 = \frac{d^3Q_-d^3Q_+d^3k_1}{E_-E_+\omega_1}$$

$$\times \delta(x_2p_+ + x_1p_- - Q_+ - Q_- - k_1), \quad (24)$$

$$E_\pm = \frac{z_\pm}{y_\pm}\varepsilon_\pm.$$

The lower limits of the energy fractions integrations x_m, y_m are determined by the experiment setup conditions. The quantity K (so called K factor) collects all the nonleading contributions. It has contributions from virtual,

soft, and hard photon emission terms. In the table below, we give its value for typical experimental points of the considered process, keeping all contributions except ones arising from additional hard photon emission.

5. CONCLUSIONS

Our consideration was devoted to the lowest order RCs. Nevertheless, the result obtained reveals the lowest order expansion of the structure functions D. So, the general Drell–Yan form of cross section is established, which is valid in all orders of PT. The order of magnitude of nonleading terms can be estimated from the table.

Without additional calculations, we can obtain by analogy with the result given above the cross section of crossing process—radiative electron–muon scattering:

$$e_-(p_1) + \mu_-(q_1) \longrightarrow e_-(p_2) + \mu_-(q_2) + \gamma(k_1) + (\gamma). \quad (25)$$

It can be constructed in complete analogy with the Drell–Yan form of cross section of the above process $e_+e_- \longrightarrow \mu_+\mu_-\gamma$, using in the right-hand side as a hard subprocess the Born cross section:

$$\frac{d\sigma_B^{e\mu\gamma}}{d\Gamma_{e\mu\gamma}}(p_1, q_1; p_2, q_2, k_1) = \frac{\alpha^3}{16\pi^2(p_1q_1)}$$

$$\times \frac{(p_1q_2)^2 + (p_1q_1)^2 + (p_2q_1)^2 + (p_2q_2)^2}{(p_1p_2)(q_1q_2)}W, \quad (26)$$

with

$$d\Gamma_{e\mu\gamma} = \frac{d^3q_2}{q_{20}}\frac{d^3p_2}{p_{20}}\frac{d^3k_1}{\omega_1}\delta^4(p_1 + q_1 - p_2 - q_2 - k_1);$$

$$W = -\left(\frac{p_1}{p_1k_1} + \frac{q_1}{q_1k_1} - \frac{p_2}{p_2k_1} - \frac{q_2}{q_2k_1}\right)^2. \quad (27)$$

It is worth noting that the value of the K factor for the last process is not known.

All the 1-loop integrals used of scalar, vector, and tensor types were published in our previous papers [10]. It is important to note that numerical values of nonleading terms for process of radiative muon pair production for the case of small muon invariant mass we find completely in agreement with the result of our paper devoted to this kinematical situation [2], where it was calculated analytically.

REFERENCES

1. V. N. Baier and V. A. Khoze, Zh. Éksp. Teor. Fiz. **48**, 946 (1965) [Sov. Phys. JETP **21**, 629 (1965)]; Zh. Éksp. Teor. Fiz. **48**, 1708 (1965) [Sov. Phys. JETP **21**, 1145 (1965)]; V. N. Baier and V. A. Khoze, Yad. Fiz. **2**, 287 (1965) [Sov. J. Nucl. Phys. **2**, 205 (1966)].

2. A. Arbuzov, V. Bytev, and E. Kuraev, hep-ph/0308292.

3. G. Rodrigo, H. Czyz, and J. H. Kuhn, hep-ph/0205097.

4. V. A. Khoze *et al.*, hep-ph/0202021; Eur. Phys. J. C **18**, 481 (2001).

5. F. A. Berends and R. Kleiss, Nucl. Phys. B **177**, 237 (1981).

6. A. I. Akhiezer and V. B. Berestetskiĭ, *Quantum Electrodynamics*, 4th ed. (Nauka, Moscow, 1981; Wiley, New York, 1965).

7. S. Eidelman and F. Jegerlehner, Z. Phys. C **67**, 585 (1995).

8. P. Kessler, Nuovo Cimento **17**, 809 (1960); V. N. Baier, V. S. Fadin, and V. A. Khoze, Nucl. Phys. B **65**, 381 (1973); V. N. Baier, V. S. Fadin, V. A. Khoze, and E. A. Kuraev, Phys. Rep. **78**, 293 (1981).

9. E. A. Kuraev and V. S. Fadin, Sov. J. Nucl. Phys. **41**, 466 (1985); O. Nikrosini and L. Trentadue, Phys. Lett. B **196**, 551 (1987).

10. V. V. Bytev, E. A. Kuraev, and B. G. Shaikhatdenov, Preprint No. E2-2002-56, JINR (Joint Inst. for Nuclear Research, Dubna, 2002).

Searching for Family-Number Conserving Neutral Gauge Bosons from Extra Dimensions[¶]

J. M. Frère[1], M. V. Libanov[2], E. Ya. Nugaev[2, *], and S. V. Troitsky[2]

[1] *Service de Physique Théorique, Université Libre de Bruxelles, B-1050, Brussels, Belgium*
[2] *Institute for Nuclear Research, Russian Academy of Sciences, Moscow, 117312 Russia*
* *e-mail: emin@ms2.inr.ac.ru*
Received April 20, 2004; in final form, May 6, 2004

Previous studies have shown how the three generations of the Standard Model fermions can arise from a single generation in more than four dimensions and how off-diagonal neutral couplings arise for gauge-boson Kaluza–Klein recurrences. These couplings conserve family number in the leading approximation. While an existing example, built on a spherical geometry, suggests a high compactification scale, we conjecture that the overall structure is generic and work out possible signatures at colliders compatible with rare decays data. © 2004 MAIK "Nauka/Interperiodica".

PACS numbers: 14.70.Pw; 14.80.-j

1. INTRODUCTION

One reason to invoke more than four space-time dimensions is to obtain elegant solutions for several long-standing problems of particle physics [1] (see [2] for a review). In particular, in the frameworks of "large extra dimensions," models have been suggested [3, 4] and studied [5] where three generations of the Standard Model (SM) fermions appear as three zero modes localized in the four-dimensional core of a defect with topological number three. When both fermions and Higgs boson are localized on a brane, the overlaps of their wave functions may result in a hierarchical pattern of fermion masses and mixings [6]. This occurs naturally in the models under discussion [3]. If the gauge fields are not localized on a brane (localization of them is a complicated issue [7]), then their Kaluza–Klein (KK) modes mediate flavor-changing processes. For the case of the compactification of two extra dimensions on a sphere [8], and with one particular pattern of charge assignments, the constraints from a flavor violation were discussed in [9]. A distinctive feature of the models of this class is the (approximate) conservation of the family number. This letter aims to discuss, without appealing to a particular model, the phenomenology of flavor-violating KK bosons in this class of theories, to be searched in future experiments.

2. DISTINCTIVE FEATURES OF "SINGLE-GENERATION" EXTRA-DIMENSIONAL MODELS

If our four-dimensional world is nothing but a core of a topological defect in $(4 + D)$ dimensions, then spe-

cific interactions of matter fields with the defect may induce localization of massless modes of these fields inside the core of the defect. Identification of the SM fields with these (almost massless compared to the scale of the defect) modes allows the extra dimensions to be large but unobserved (see [2] for a review and list of references). In particular, the index theorem guarantees the existence of N linearly independent chiral zero modes of each fermion field in the bosonic background with topological number N. This suggests to use $N = 3$ to obtain three generations of the SM fermions from a single one in extra dimensions. Quite nontrivially, the linear independence of the three modes results in their different behavior at the origin, which may give rise to a naturally hierarchical pattern of masses of the fermions of three generations. We concentrate here on the most elaborated example of two extra dimensions ($D = 2$), though our qualitative results hold for a more involved case of higher dimensions as well.

With $D = 2$, the two extra dimensions can be parametrized in terms of one radial, r, and one angular, ϕ, variable. The location of the defect corresponds to $r = 0$; we suppose that the compactification preserves rotational invariance and allow ϕ to vary from 0 to 2π. The defect itself has a structure of the $U(1)$ vortex. The definition of r and its maximal value depend on the compactification scheme. The three light four-dimensional families of particles arising from a single family in six dimensions are characterized then by different winding properties in ϕ: three families enumerated by $n = 1, 2, 3$ have the following wave functions,

$$\psi_n \sim f_n(r)e^{i(3-n)\phi}.$$

These wave functions correspond, in four dimensions, to the *gauge* eigenstates of the SM fermions. To

---

[¶]This article was submitted by the authors in English.

the first approximation, both the theory and the background possess rotational invariance (shifts in ϕ supplemented by $U(1)$ transformations). The fermion mass matrix originates from a ϕ-independent scalar field and is thus perfectly diagonal, while the mass spectrum results from the (in principle calculable) overlap of the wave functions of the scalar and fermions, giving the usual hierarchy between families. At this level, the mass and gauge eigenstates coincide, the family number corresponds to the six-dimensional angular momentum and is thus exactly conserved (note that this still does not forbid processes where both quark and lepton flavors change oppositely, e.g. $K \longrightarrow \mu \bar{e}$). Mixing between fermions of different species, leading to the desired Kobayashi–Maskawa (K–M) matrix, arises as a suppressed, second-order effect controlled by an auxiliary scalar field with winding number one, which generates transitions between adjoining generations.

We will be concerned here with the gauge interactions. The lowest mode of the gauge bosons in four dimensions left massless by the vortex localization of the fermions eventually acquires mass by the Brout–Englert–Higgs formalism. The electrically neutral such bosons stay as usual diagonal in their interactions with the fermionic mass eigenstates. The charge universality is provided by the fact that the lowest mode of a gauge boson is constant in transverse dimensions and overlap integrals of the normalized fermionic wave functions with this mode coincide with each other. This is not the case for the higher KK modes of the vector particles; their profiles in (r, ϕ) are determined by

$$A_{lm}(r, \phi) = a_{lm}(r)e^{im\phi},$$

where $l = 1, 2, \ldots$ and $-l \le m \le l$. Nontrivial profiles a_{lm} cause different overlaps with fermions of different families, while nonzero windings result in transitions between generations.

Angular excitation of, for example, the first KK mode of Z boson behaves in six dimensions as

$$Z' \sim e^{\pm i\phi}.$$

After integration in extra dimensions, we obtain an effective four-dimensional Lagrangian with complex vector field Z', which generates "horizontal" transitions between families in which the generation number changes by one unit.

Such transitions are of course severely limited by the high mass of the excitations, but also, in the first approximation (neglecting the K–M mixing), they do conserve the family number. For instance, the following processes are possible:

$$s + \bar{d} \Rightarrow Z' \Rightarrow s + \bar{d},$$

$$s + \bar{d} \Rightarrow Z' \Rightarrow \mu + \bar{e},$$

$$s + \bar{d} \Rightarrow Z' \Rightarrow \tau + \bar{\mu}.$$

The first process in the first order in Z' exchange thus conserves strangeness (and only small corrections linked to Cabibbo mixing would affect this), but the second, while conserving family number, is a typical flavor-changing neutral current (FCNC) interaction, violating both strangeness and electron number. While the last reaction is only possible in collisions, the study of rare K_L decay puts strong limits on the mass and coupling constant of the Z' [9] (similar relations hold for the photon and gluon angular excitations).

For the time being, we wish to retain these main characteristics of the model: families are associated to some "winding number," conserved in excited boson exchanges up to small Kobayashi–Maskawa corrections. The detailed spectrum and strength of coupling of the gauge boson excitations will depend on the exact geometrical implementation. A fully worked-out example was presented in detail in [9], leading however to a particularly high mass spectrum.

We conjecture that the same structure would remain intact in other implementations. In [9], we supposed that the wave functions of fermions and the first KK mode of the gauge boson overlap strongly. Then, the effective Lagrangian for the interaction between fermions and flavor-changing bosons contains the same coupling constant as interaction with the lowest KK modes, i.e., the usual gauge bosons. However, in particular models the profiles of fermionic wave functions can be shifted, which means more freedom in couplings. Let us denote the absolute value of the overlap integral in extra dimensions between the wave functions ψ_i, ψ_j of the fermions of generations i, j and the wave function $\psi_{Z'}$ of the Z excitation as

$$\left| \int \psi_{Z'} \psi_i \psi_j d^2 x \right| = \kappa_{ij}.$$

Then, $(\bar{e}, \mu)$ interaction through Z' is described by

$$\frac{g_{EW}\kappa_{12}}{2\cos\theta_W} Z'_\mu \left[\frac{1}{2}\bar{e}\gamma_\mu\gamma_5\mu - \left(\frac{1}{2} - 2\sin^2\theta_W \right)\bar{e}\gamma_\mu\gamma_5\mu \right].$$

The structure of this term coincides with the interaction of $\bar{e}$, e, and Z in SM with the strength $g = g_{EW}\kappa_{12}$. Interactions of other leptons and quarks arise in a similar way.

The main restriction on the mass scale of the model with $\kappa_{ij} \simeq \delta_{i, i+1}$ arises from the limit on the branching ratio for the process $K_L \longrightarrow \bar{\mu} e$. Taking into account that κ_{12} can be different from 1, the strongest restriction from the rare processes gives [9]

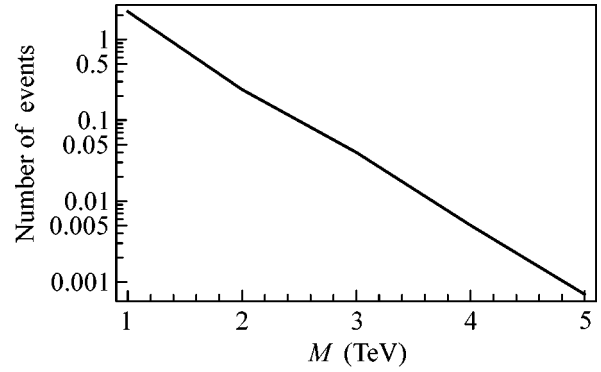$$M_{Z'} \gtrsim \kappa_{12} \times 100 \text{ TeV}.$$

In the simplest case when all $\kappa_{ij} \sim \kappa\delta_{i, i+1}$,

$$\kappa \lesssim \frac{M_{Z'}}{100 \text{ TeV}}.$$

The decay width of the excited Z and photon results mainly from their decay into fermions (with the possi-
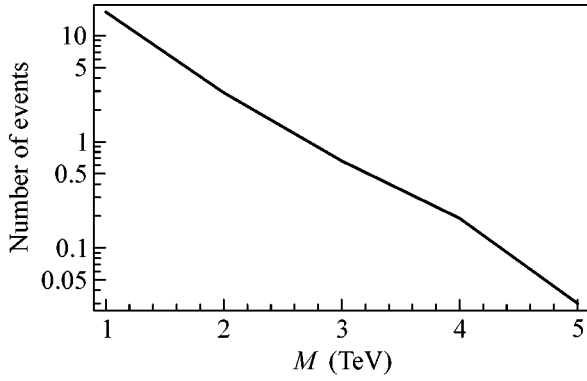
Fig. 1. Number of events for $(\mu^+ e^-)$ pairs production as a function of the vector bosons mass M with $\kappa = M/100$ TeV.

Fig. 2. Number of events for $(\mu^- e^+)$ pairs production as a function of the vector bosons mass M with $\kappa = M/100$ TeV.

bility of model-dependent additional scalar decay channels) and, by simple counting of modes, is estimated as

$$\Gamma(Z') = \kappa^2 \frac{M_{Z'}}{M_Z} \times 12.5 \Gamma_{Z \to \bar{\nu}\nu} \cong \kappa^2 \frac{M_{Z'}}{M_Z} \times 1.8 \text{ GeV}.$$

Similarly, the width of the first photon angular excitation is given by

$$\Gamma(\gamma') = \frac{16}{3} \kappa^2 \sin^2 2\theta_W \frac{M_{\gamma'}}{M_Z} \Gamma_{Z \to \bar{\nu}\nu} \cong \kappa^2 \frac{M_{\gamma'}}{M_Z} \times 1.3 \text{ GeV}.$$

The first KK excitation of the gluon is wider due to the larger coupling constant,

$$\Gamma(G') \cong \kappa^2 \frac{M_{G'}}{M_Z} \times 7.2 \text{ GeV}.$$

A typical value of Γ is of order 10^{-3} GeV for $\kappa \simeq 10^{-2}$ and $M_{Z'} = 1$ TeV. In what follows, we will assume that the masses of all the FCNC bosons are equal,

$$M_{Z'} = M_{\gamma'} = M_{g'} = M,$$

as in the case of spherical model of [9].

3. COLLIDER SEARCHES

The vector bosons discussed here can, in principle, be observed at colliders due to the flavor-changing decay modes into (μe) and $(\tau \mu)$ pairs. The corresponding process is very similar to the Drell–Yan pair production. A typical feature of the latter is the suppression of the cross section with increasing resonance mass at a fixed center-of-mass energy [10]. This suppression is due to the falloff of the structure functions at large momenta of quarks.

The flavor-changing decays of this kind have a distinctive signature: antimuon and electron (or their antiparticles) with equal and large transverse momenta in the final state. Observation of just a few such pairs with the same invariant masses would give a strong argument in flavor of the flavor-changing boson in the s channel and would help to distinguish the effects dis-

cussed here from, say, (loop-induced) flavor violation in supersymmetry. Even stronger evidence would be provided by the observation of higher KK modes (which of course requires larger center-of-mass energy).

We estimate the number of events for the case of pp collisions with the help of the CompHEP package [11]. For our calculation, we use the expected LHC value of 100 fb^{-1} for luminosity and $\sqrt{s} = 14$ TeV. The number of $(\mu^+ e^-)$ events is presented in Fig. 1 for different values of the vector bosons mass M and κ adjusted to $\kappa = M/100$ TeV. The same plot for $(\mu^- e^+)$ pairs is given in Fig. 2.

Note that production of $(\mu^+ e^-)$ pairs is more probable than $(\mu^- e^+)$, because the former process can use valence u and d quarks in the proton, while the latter only involves partons from the sea. The same numbers are also representative for the $(\mu^- \tau^+)$ channel.

There are also other signatures of FCNC effects, in particular, with hadronic final states, when $(\bar{t}, c)$ or $(\bar{b}, s)$ jets are produced. The dominant contribution to these processes arises from the interactions with higher KK modes of gluons, which have large coupling constant. For a mass of $M_{G'} = 1$ TeV, we estimate the number of events as $N = 1.2 \times 10^3$. But, potentially large SM backgrounds should be carefully considered for such channels.

4. CONCLUSIONS

We have considered FCNC effects in models with approximate family-number conservation mediated by the heavy vector bosons in a class of models. From our estimations, there is reason for searching for such FCNC bosons with masses of order 1 TeV at LHC. The main signature is the production of $(\mu^+ e^-)$ or $(\mu^- \tau^+)$ pairs with equal and large transverse momenta of leptons. Production of $(\bar{t} c)$ quarks is more probable but

less clear-cut due to the large background from SM processes.

On the other hand, the models with heavy vector bosons, whose interactions conserve the family number, can be tested in experiments studying rare processes. The strongest and least model-independent limit on the mass of these bosons arises from the limit on $K_L \longrightarrow \mu^{\pm} e^{\mp}$ branching ratio (in this process, the family number does not change). Discovery of this decay without signs of rare processes which violate the generation number (such as μe conversion) would support significantly the models discussed here. Future experiments on the search of lepton-flavor violating kaon decays are thus of great importance (see [12] for relevant discussion).

REFERENCES

1. N. Arkani-Hamed, S. Dimopoulos, and G. R. Dvali, Phys. Lett. B **429**, 263 (1998); hep-ph/9803315; K. Akama, Lect. Notes Phys. **176**, 267 (1982); hep-th/0001113; V. A. Rubakov and M. E. Shaposhnikov, Phys. Lett. B **125B**, 136 (1983); G. W. Gibbons and D. L. Wiltshire, Nucl. Phys. B **287**, 717 (1987); I. Antoniadis, Phys. Lett. B **246**, 377 (1990); A. Nakamura and K. Shiraishi, Acta Phys. Pol. B **21**, 11 (1990).

2. V. A. Rubakov, Usp. Fiz. Nauk **171**, 913 (2001) [Phys. Usp. **44**, 871 (2001)]; hep-ph/0104152.

3. M. V. Libanov and S. V. Troitsky, Nucl. Phys. B **599**, 319 (2001); hep-ph/0011095.

4. J. M. Frere, M. V. Libanov, and S. V. Troitsky, Phys. Lett. B **512**, 169 (2001); hep-ph/0012306.

5. J. M. Frere, M. V. Libanov, and S. V. Troitsky, J. High Energy Phys. **0111**, 025 (2001); hep-ph/0110045; M. V. Libanov and E. Y. Nougaev, J. High Energy Phys. **0204**, 055 (2002); hep-ph/0201162.

6. N. Arkani-Hamed and M. Schmaltz, Phys. Rev. D **61**, 033005 (2000); hep-ph/9903417.

7. G. Dvali and M. Shifman, Phys. Lett. B **475**, 295 (2000); hep-ph/0001072; S. Dubovsky and V. Rubakov, Int. J. Mod. Phys. A **16**, 4331 (2001); hep-th/0105243; M. Giovannini, H. Meyer, and M. E. Shaposhnikov, Nucl. Phys. B **619**, 615 (2001); hep-th/0104118; M. Giovannini, Phys. Rev. D **66**, 044016 (2002); hep-th/0205139; S. Randjbar-Daemi and M. Shaposhnikov, J. High Energy Phys. **0304**, 016 (2003); hep-th/0303247.

8. J. M. Frere, M. V. Libanov, E. Y. Nugaev, and S. V. Troitsky, J. High Energy Phys. **0306**, 009 (2003); hep-ph/0304117.

9. J.-M. Frere, M. V. Libanov, E. Y. Nugaev, and S. V. Troitsky, J. High Energy Phys. **03**, 001 (2004); hep-ph/0309014.

10. S. D. Drell and T. M. Yan, Phys. Rev. Lett. **25**, 316 (1970); Phys. Rev. Lett. **25**, 902(E) (1970).

11. A. Pukhov *et al.*, hep-ph/9908288.

12. L. G. Landsberg, Yad. Fiz. **65**, 1795 (2002) [Phys. At. Nucl. **65**, 1749 (2002)].

Absorption in Ultraperipheral Nucleus–Atom Collisions in Crystal¶

V. R. Zoller

Institute for Theoretical and Experimental Physics, Moscow, 117218 Russia
e-mail: zoller@itep.ru
Received May 11, 2004; in final form, May 17, 2004

The Glauber theory description of particle– and nucleus–crystal Coulomb interactions at high energy is developed. The allowance for the lattice thermal vibrations is shown to produce a strong absorption effect, which is of prime importance for quantitative understanding of the coherent Coulomb excitation of ultrarelativistic particles and nuclei passing through the crystal. © 2004 MAIK "Nauka/Interperiodica".

PACS numbers: 25.75.-q; 11.80.-m

In this communication, we discuss the origin and estimate the strength of the absorption effect in coherent particle– and nucleus–crystal Coulomb interactions at high energy.

Generally, the multiloop corrections generate the imaginary part of the scattering amplitude even if the three-level amplitude is purely real. For example, the purely real Born amplitude of the high-energy Coulomb scattering in crystal acquires the imaginary part due to the multiple scattering (MS) effects [1]. However, in the widely used static/frozen lattice approximation (SL approximation), the account of rescatterings alters only the overall real phase of the full amplitude, thus producing no absorption effect [2]. Indeed, to the SL approximation, the exact scattering matrix placed between the ground states of crystal $\langle \exp(i\chi) \rangle$ is approximated by $\exp(i\chi)$ and the imaginary part of the scattering amplitude

$$1 - \langle \exp(i\chi) \rangle,$$

which is

$$\sim \frac{i}{2}[\langle \chi^2 \rangle - \langle \chi \rangle^2],$$

disappears. With the allowance for the lattice thermal vibrations, the Coulomb phase shift function gets a nonvanishing imaginary part which is interpreted as an absorption effect, the phenomenon related to the creation and annihilation of excited intermediate states of crystal and as such manifesting itself only beyond the SL approximation.

The account of the lattice thermal vibrations provides a natural ultraviolet (UV) regulator of the theory and, as we shall see, enables quantitative understanding of the phenomenon of the coherent Coulomb excitation of relativistic particles and nuclei passing through the

---

¶This article was submitted by the author in English.

crystal. The latter is the goal we pursue in this communication.

We start with the well-known example of the coherent Coulomb elastic scattering of charged particle or nucleus (charge Z_1) by a linear chain of N identical atoms in a crystal target. The interatomic distances in crystal, a, are large compared to the Thomas–Fermi screening radius r_0, $a \sim 3$–5 Å $\gg r_0 = r_B Z_2^{-1/3} \sim 0.1$ Å, where Z_2 is the atomic number of the target atom and r_B is the Bohr radius [3]. The relevant impact parameters, b, satisfy the condition $b \ll a$, and the amplitudes of scattering by different atomic chains parallel to a given crystallographic axis are incoherent.

In the eikonal approximation [1], the phase shift function is the sum of the phase shifts contributed by the individual atoms,

$$\chi = \sum_{j=1}^{N} \chi(\mu|\mathbf{b} - \mathbf{s_j}|).$$

The ground state of crystal we describe by the uncorrelated wave function

$$\Psi = \prod_{j=1}^{N} \psi(\mathbf{r_j}),$$

where the positions of the N atoms which make up the target are defined by the 3D vectors $\mathbf{r_j}$, $j = 1, \ldots, N$, and the 2D vectors $\mathbf{s_j}$ are the projections of these vectors on the impact parameter plane. Hence, the amplitude of small-angle elastic scattering has the following form:

$$F(q) = ip\int b\,db\,J_0(qb)\{1 - \langle \exp[i\chi(\mu b)]\rangle^N\}. \quad (1)$$

where q is the 2D vector of the momentum transfer, and the incident particle momentum p is assumed to be large enough to satisfy the condition of applicability of

the straight paths approximation, $p/q^2 \gg aN$. The latter condition ensures the coherence of interactions with different atoms. In Eq. (1), the screened Coulomb phase shift contributed by the individual atom is

$$\chi(\mu b) = -\beta K_0(\mu b), \qquad (2)$$

with $\beta = 2\alpha Z_1 Z_2$ and $\mu = r_0^{-1}$. Hereafter, $J_v(x)$, $I_v(x)$, and $K_v(x)$ are the Bessel functions. The brackets $\langle \, \rangle$ signify that an average is to be taken over all configurations of atoms in the ground state of crystal.

After the azimuthal integration, the term $\langle \exp(i\chi) \rangle$ takes the form

$$\langle \exp(i\chi) \rangle = \int d^2 s \rho(s) \exp[i\chi(\mu|\mathbf{b} - \mathbf{s}|)]$$

$$= \exp(-\Omega^2 b^2) \int dx \exp(-x) \qquad (3)$$

$$\times I_0(2b\Omega\sqrt{x}) \exp[-i\beta K_0(\mu\sqrt{x}/\Omega)].$$

The 2D vector s describes the position of the target atom in the impact parameter plane. The one-particle probability distribution $\rho(s)$ is as follows:

$$\rho(s) = \int dz |\psi(\mathbf{s}, z)|^2 = (\Omega^2/\pi) \exp(-\Omega^2 \mathbf{s}^2). \qquad (4)$$

For the most commonly studied elements at room temperature, the ratio μ/Ω varies in a wide range, from $\mu/\Omega \sim 0.1$ to $\mu/\Omega \sim 1$ [3]. Consider first the region of small impact parameters. For $b \ll 1/2\Omega$, only small s such that $\mu s \lesssim 1$ contribute. One can set then in Eq. (3) $K_0(\mu s) \simeq \log(1/\mu s)$ and integrate over s. The result is

$$\langle \exp(i\chi) \rangle = \left(\frac{\mu}{\Omega}\right)^{i\beta} \Gamma\left(1 + \frac{i\beta}{2}\right) \Phi\left(-\frac{i\beta}{2}; 1; -\Omega^2 b^2\right). \quad (5)$$

In Eq. (5), $\Phi(a, b; z)$ is the confluent hypergeometric function. From (5), it follows, in particular, that

$$|\langle \exp(i\chi) \rangle|_{b=0} = \left[\frac{\pi\beta}{2\sinh(\pi\beta/2)}\right]^{1/2} \qquad (6)$$

and in the weak coupling regime, $\beta \ll 1$,

$$|\langle \exp(i\chi) \rangle|_{b=0} \simeq 1 - \frac{\pi^2 \beta^2}{48}, \qquad (7)$$

while, for $\beta \gtrsim 1$,

$$|\langle \exp(i\chi) \rangle|_{b=0} \simeq \sqrt{\pi\beta} \exp\left(-\frac{\pi\beta}{4}\right). \qquad (8)$$

Therefore, at small impact parameters, $b \lesssim \Omega^{-1}$, the intensity of outgoing nuclear waves as a function of N exhibits exponential attenuation.

The absorption effect becomes weaker toward the region of large impact parameters $b \gtrsim 1/2\Omega$,

$$|\langle \exp(i\chi) \rangle|^N \simeq |\langle \exp(i\chi) \rangle|_{b=0}^N$$

$$\times \left[1 + \frac{N\beta^2}{16}(\Omega b)^4 + \dots\right]. \qquad (9)$$

For still larger b, $b \gg 1/2\Omega$, making use of the asymptotic form $I_0(z) \simeq (2\pi z)^{-1/2} \exp(z)$ and the condition

$$\omega = \frac{d\chi}{db} = \mu\beta K_1(\mu b) \ll \Omega \qquad (10)$$

yields

$$\langle \exp(i\chi) \rangle$$

$$\simeq 2\Omega \int \frac{s\,ds}{\sqrt{\pi b s}} \exp[-\Omega^2(b-s)^2] \exp[i\chi(\mu s)] \quad (11)$$

$$\simeq \exp(i\chi) \exp[-\omega^2/4\Omega^2].$$

From (11), (5), (1), it follows that the absorption is especially strong for impact parameters

$$b \lesssim b_a = \frac{1}{2\mu} \log \frac{\pi\mu^2 \beta^2 N}{4\Omega^2}. \qquad (12)$$

For $b \lesssim b_a$, the atomic chain acts like an opaque "black" disc. Certainly, the value of this finding differs for different observables and for different processes proceeding at different impact parameters.

Integrating once by parts reduces $F(q)$ to the form convenient for evaluation of the total cross section,

$$F(q) = \frac{ip\mu N}{q}$$

$$\times \int_0^\infty b\,db\, J_1(qb) \langle i\chi' \exp(i\chi) \rangle \langle \exp(i\chi) \rangle^{(N-1)}. \qquad (13)$$

At small q and large N, only large impact parameters, $b \gg \mu^{-1}$, may contribute to $F(q)$. This is the multiple scattering effect [1, 2], which gives rise to the dominance of ultraperipheral collisions in the coherent particle–crystal interactions. Then, for $q \lesssim q_0 = \mu/\xi$ and $\xi \gg 1$, the steepest descent from the saddle-point

$$b_0 = \mu^{-1}[\xi + i\pi/2] \qquad (14)$$

in Eq. (13) yields

$$F(q) \simeq \frac{ipb_0}{q} J_1(qb_0). \qquad (15)$$

The effect of lattice thermal vibrations at small q appears to be marginal and reduces to the factor $\exp(\mu^2/4\Omega^2 N)$ in (15), which is irrelevant in the region of large N, where the amplitude $F(q)$ coincides with the elastic scattering amplitude given by the SL approximation [2].

If $q \gtrsim q_0$, the stationary phase approximation gives the elastic scattering amplitude of the form

$$F(q) \simeq \frac{-ip\sqrt{\eta}}{\mu q}\exp\left(-\frac{iq\eta}{\mu}\right)\exp\left(-\frac{q^2}{4\Omega^2 N}\right), \qquad (16)$$

where $\eta = \log(\mu\beta N/q) \gg 1$. This is the lattice vibrations, which provide a natural momentum cutoff and ensure the convergence of the integral for the coherent elastic scattering cross section,

$$\sigma_{el} = \frac{\pi}{p^2}\int dq^2 |F(q)|^2 \approx \frac{\pi\xi^2}{\mu^2}\int_0^{q_0^2}\frac{dq^2}{q^2}J_1^2\left(\frac{q\xi}{\mu}\right) \\ + \frac{\pi}{\mu^2}\int_{q_0^2}^{\infty}\frac{dq^2}{q^2}\log\left(\frac{\mu\beta N}{q}\right)\exp\left(-\frac{q^2}{2\Omega^2 N}\right), \qquad (17)$$

which, for $\xi \gg 1$, is simply

$$\sigma_{el} \approx \frac{\pi}{\mu^2}\xi^2. \qquad (18)$$

From Eq. (15), by means of the optical theorem, we find the total cross section

$$\sigma_{\text{tot}} = \frac{4\pi}{p}\text{Im}F(0) \approx \frac{2\pi}{\mu^2}\xi^2. \qquad (19)$$

Consequently, at high energy and for $\xi \gg 1$, $\sigma_{el} \approx \frac{1}{2}\sigma_{\text{tot}}$.

Now, let us turn to the process of the coherent Coulomb excitation of ultrarelativistic particles and nuclei passing through the crystal. This way of the experimental study of rare processes was proposed in [4–10].

The ultrarelativistic projectile nucleus (mass number A, charge Z_1, and four-momentum p) moving along a crystal axis undergoes a correlated series of soft collisions, which give rise to diagonal ($A \longrightarrow A, A^* \longrightarrow A^*$) and off-diagonal ($A \longrightarrow A^*, A^* \longrightarrow A$) transitions. In [4, 5, 9], it was proposed to study the electric dipole transition in ^{19}F, the excitation of the state $|J^\pi = 1/2^-\rangle$ from the ground state $|1/2^+\rangle$. The phenomenological matrix element of the transition $1/2^+ \longrightarrow 1/2^-$ is [11]

$$\mathcal{M} = \frac{1}{2}d\bar{u}(p')\gamma_5(\hat{q}\hat{\varepsilon} - \hat{\varepsilon}\hat{q})u(p), \qquad (20)$$

where both $u(p')$ and $u(p)$ are bispinors of initial and final states of the projectile, d is the transition dipole moment, and ε is the photon polarization vector. The transverse and longitudinal components of the 4-vector $p - p'$ are denoted by $\mathbf{q}$ and κ, respectively. In what follows, $q = |\mathbf{q}|$. Because of the large value of the lifetime of the 110 keV level $^{19}F(1/2^-)$ [12], the decay of excited state inside the target crystal can be safely neglected. Due to the smallness of the transition dipole moment, $d \simeq 5 \times 10^{-8}$ keV^{-1}, the excitation amplitude is much smaller than the elastic Coulomb amplitude for all q up

to $q \sim \sqrt{4\pi\alpha}\, Z_1/d$ and can be considered as a perturbation [11]. Thus, the multichannel problem reduces to the one-channel one.

The high-energy helicity-flip Born amplitude of the transition $1/2^+ \longrightarrow 1/2^-$ in collision of the projectile-nucleus with N bound atoms in crystal reads

$$F_{ex}^B(\mathbf{q}) = S(\kappa)\frac{p}{2\pi}\frac{g(\boldsymbol{\sigma q})}{q^2 + \lambda^2}\exp\left(-\frac{q^2}{4\Omega^2}\right), \qquad (21)$$

where $\boldsymbol{\sigma} = (\sigma_1, \sigma_2, \sigma_3)$ is the Pauli spin vector, $\{\sigma_i, \sigma_j\} = 2\delta_{ij}$, and the amplitude we constructed is to be regarded as an operator which transforms the initial helicity state of the projectile into its final state. In the denominator of Eq. (21), $\lambda^2 = \mu^2 + \kappa^2$. In the Glauber approximation, the longitudinal momentum transfer, which determines the coherency length, $l_c \sim \kappa^{-1}$, reads [13]

$$\kappa = \frac{M\Delta E}{p}, \qquad (22)$$

where M is the mass of projectile and ΔE is the excitation energy.[1]

The structure factor of crystal $S(\kappa)$ to the first order in g is

$$S(\kappa) = \exp\left[-\frac{\kappa^2}{4\Omega^2}\right]\frac{\sin(\kappa Na/2)}{\sin(\kappa a/2)}. \qquad (23)$$

If the projectile momentum satisfies the resonance condition [4, 5, 7, 9],

$$\frac{M\Delta E}{p} = \frac{2\pi n}{a}, \quad n = 0, 1, 2\ldots, \qquad (24)$$

$S(\kappa) \sim N$. Then, to the first order in g (Born approximation), the cross section of the coherent excitation of the projectile in scattering on a chain of N atoms in crystal is

$$\sigma_{ex}^B = \frac{\pi}{p^2}\int dq^2\left|F_{ex}^B(\mathbf{q})\right|^2 \propto \frac{g^2 N^2}{4\pi}, \qquad (25)$$

where $g = \sqrt{4\pi\alpha}\, dZ_2$. The central idea of [4–10] based on the Born approximation is that the transition rate can be enhanced substantially due to coherency of interactions, which is assumed to be sustained over the large distance scale. The law $\sigma_{ex} \propto N^2$ is expected to hold true up to the crystal thicknesses $N = L/a \sim 10^5$–10^6 in tungsten target. In [10], the Born approximation for the coherent excitation of Σ^+ in high-energy proton–crystal interactions $p\gamma \longrightarrow \Sigma^+$ was assumed to be valid up to $N \sim 10^8$. However, the account of the initial- and final-state Coulomb interactions dramatically changes the dependence of σ_{ex} on N. For example, even in the dia-

---

[1] The Fresnel corrections to the Glauber approximation which are neglected here become important for large N or large q, diminishing the coherency length and bringing about an additional suppression of coherent processes [14].

mond crystal,

$$\sigma_{ex} \sim \sigma_{ex}^B\left(1 - \frac{N\omega^2}{2\Omega^2}\right) \qquad (26)$$

and $\omega^2/2\Omega^2 \simeq 2\beta^2\mu^2/\Omega^2 \sim 1/20$ (see [15] for more details). Thus, the Born approximation becomes irrelevant already at $N \gtrsim 10$.

The evaluation of the transition amplitude on a chain of N identical atoms including all the multiphoton t-channel exchanges reads

$$F_{ex}(\mathbf{q}) = \frac{p}{\pi}\int d^2\mathbf{b}\exp(i\mathbf{q}\mathbf{b})$$
$$\times \langle f_{ex}^B\exp(i\chi)\rangle\langle\exp(i\chi)\rangle^{N-1}. \qquad (27)$$

Equation (27) contains two bracketed factors. The first one corresponds to the nuclear excitation amplitude in scattering on the atom bound in crystal. At small impact parameters, $b \lesssim 1/2\Omega$,

$$\langle f_{ex}^B\exp(i\chi)\rangle$$
$$\simeq S(\kappa)\frac{g}{2\pi b}(\boldsymbol{\sigma}\mathbf{n_b})\sinh\left(\frac{1}{2}\Omega^2 b^2\right)\exp\left(-\frac{1}{2}\Omega^2 b^2\right). \qquad (28)$$

Because of both the multiple scattering effect and absorption, only $b \gg \mu^{-1}$ may contribute to $F_{ex}(\mathbf{q})$. In this region of impact parameters,

$$\langle f_{ex}^B\exp(i\chi)\rangle$$
$$\simeq S(\kappa)\frac{g}{4\pi}(\boldsymbol{\sigma}\mathbf{n_b})\lambda K_1(\lambda b)\exp(i\chi)\exp\left(-\frac{\omega^2}{4\Omega^2}\right). \qquad (29)$$

The second factor in (27) describes the initial- and final-state interactions of the projectile and has been calculated above. Then,

$$F_{ex}(\mathbf{q}) \approx \frac{gp}{2\pi}S(\kappa)(\boldsymbol{\sigma}\mathbf{n_q})\int_{1/\mu}^{\infty} b\,db\,J_1(qb)$$
$$\times \lambda K_1(\lambda b)\exp(iN\chi)\exp(-N\omega^2/4\Omega^2), \qquad (30)$$

where $\mathbf{n_q} = \mathbf{q}/|\mathbf{q}|$. The contribution of the domain $q \lesssim q_0 = \mu/\xi$ to the excitation cross section can be neglected as far as $F_{ex} \propto q$ for $q \lesssim q_0$. If $q \gg q_0$ and $\xi \gg 1$, the stationary phase approximation gives the coherent excitation amplitude of the form

$$F_{ex}(\mathbf{q}) \approx \frac{ipg(\boldsymbol{\sigma}\mathbf{n_q})}{2\pi\beta}\frac{S(\kappa)}{N}\frac{\lambda}{\mu}\sqrt{\eta}\exp(-\delta\eta)$$
$$\times \exp\left(-\frac{iq\eta}{\mu}\right)\exp\left(-\frac{q^2}{4\Omega^2 N}\right). \qquad (31)$$

We see that the helicity-flip dynamics removes the factor $1/q$ from elastic amplitude (16), thus making the UV regularization of the excitation cross section indispensable. The latter is evaluated as

$$\sigma_{ex} = \frac{\pi}{p^2}\int dq^2|F_{ex}(\mathbf{q})|^2 \sim \frac{g^2 N^{1-\delta}}{8\pi}C\log\left(\frac{N}{\delta\gamma}\right), \qquad (32)$$

where $C = \gamma^\Delta\Delta^2\Gamma(\Delta)$, $\gamma = 2\Omega^2/\beta^2\mu^2$, $\Delta = \lambda/\mu$, and $\delta = \Delta - 1 \sim \kappa^2/2\mu^2 \ll 1$. In (32), we set simply $S(\kappa) = N$. Thus, the account of multiple scatterings and absorption turns the Born approximation cross section $\sigma_{ex} \propto N^2$ into $\sigma_{ex} \propto N^{1-\delta}\log N$. In the limit of $p \longrightarrow \infty$ and $\delta \longrightarrow 0$,

$$\sigma_{ex} \sim \frac{g^2 N}{8\pi}\gamma\log\left(\frac{N}{\gamma}\right). \qquad (33)$$

The dependence of σ_{ex} on N differs from that of fully unitarized $\sigma_{el} \propto \log^2 N$. The reason is that, in σ_{ex}, we sum the eikonal diagrams to all orders in β but only to the first order in g. Such a unitarization procedure is, of course, incomplete, but this is of no importance for practical purposes since the smallness of $d^2\Omega^2$ makes the next-to-leading-order corrections negligibly small up to $N \sim \alpha Z_1^2/\delta\Omega^2 d^2 \sim 10^{12}$.

REFERENCES

1. R. J. Glauber, in *Lectures in Theoretical Physics*, Ed. by W. E. Brittin *et al.* (Interscience, New York, 1959), Vol. 1, p. 315.

2. N. P. Kalashnikov, E. A. Koptelov, and M. I. Ryazanov, Sov. Phys. JETP **63**, 1107 (1972); N. P. Kalashnikov and V. D. Mur, Sov. J. Nucl. Phys. **16**, 613 (1973).

3. D. S. Gemmel, Rev. Mod. Phys. **46**, 1 (1974).

4. V. V. Okorokov, Sov. J. Nucl. Phys. **2**, 719 (1966); V. V. Okorokov, Yu. L. Pivovarov, A. A. Shirokov, and S. A. Vorobev, *Proposal of Experiment on Coherent Excitation of Relativistic Nuclei in Crystals* (Moscow, 1990), ITEP-90-49, Fermilab Library Only.

5. V. V. Okorokov and S. V. Proshin, *Investigation of the Coherent Excitation of the Relativistic Nuclei in a Crystal* (Moscow, 1980), ITEP-13-1980.

6. Yu. L. Pivovarov, H. Geissel, Yu. M. Filimonov, *et al.*, *On the Resonant Coherent Excitation of Relativistic Heavy Ions* (Darmstadt, 1995), GSI-95-38.

7. Yu. L. Pivovarov and A. A. Shirokov, Sov. J. Nucl. Phys. **37**, 653 (1983).

8. Yu. L. Pivovarov, A. A. Shirokov, and S. A. Vorobev, Nucl. Phys. A **509**, 800 (1990).

9. R. Fusina and J. C. Kimball, Nucl. Instrum. Methods Phys. Res. B **33**, 77 (1988).

10. A. Dubin, Yad. Fiz. **52**, 1243 (1990) [Sov. J. Nucl. Phys. **52**, 790 (1990)].

11. V. R. Zoller, Pis'ma Zh. Éksp. Teor. Fiz. **75**, 147 (2002) [JETP Lett. **75**, 119 (2002)].

12. F. Ajzenberg-Selove, Nucl. Phys. A **190**, 1 (1972).

13. V. N. Gribov, Sov. Phys. JETP **29**, 483 (1969); Sov. Phys. JETP **29**, 709 (1970).

14. V. R. Zoller, Phys. Lett. B **416**, 447 (1998).

15. V. R. Zoller, *Ultra-Relativistic Nuclei in Crystal Channel: Coulomb Scattering, Coherence and Absorption* (2004), ITEP-PH-2/2004.

On the Chiral Phase Transition in Hadronic Matter[¶]

M. N. Chernodub and B. L. Ioffe

Institute of Theoretical and Experimental Physics, Moscow, 117218 Russia

Received May 20, 2004

A qualitative analysis of the chiral phase transition in QCD with two massless quarks and nonzero baryon density is performed. It is assumed that, at zero baryonic density, $\rho = 0$, the temperature phase transition is of the second order. Due to a specific power dependence of baryon masses on the chiral condensate, the phase transition becomes of the first order at the temperature $T = T_{ph}(\rho)$ for $\rho > 0$. At temperatures $T_{cont}(\rho) > T > T_{ph}(\rho)$, there is a mixed phase consisting of the quark phase (stable) and the hadron phase (unstable). At the temperature $T = T_{cont}(\rho)$, the system experiences a continuous transition to the pure chirally symmetric phase. © 2004 MAIK "Nauka/Interperiodica".

PACS numbers: 12.38.Mh; 25.75.Nq; 11.30.Rd

It is well known that chiral symmetry is valid in perturbative quantum chromodynamics (QCD) with massless quarks. It is expected also that chiral symmetry takes place in full-perturbative and nonperturbative QCD at high temperatures ($T \gtrsim 200$ MeV) if heavy quarks (c, b, t) are ignored. Chiral symmetry is strongly violated, however, in hadronic matter, i.e., in QCD at $T = 0$ and low density. What is the order of phase transition between two phases of QCD with broken and restored chiral symmetry with varying temperature and density is not completely clear now. There are different opinions about this subject (for a detailed review, see [1, 2] and references therein).

In this paper, we discuss the phase transitions in QCD with two massless quarks, u and d. Many lattice calculations [3–6] indicate that, at zero chemical potential, the phase transition is of the second order. It will be shown below that the account of baryon density drastically changes the situation and the transition becomes of the first order, and, at high density, the matter is always in the chirally symmetric phase (see also [7]).

Let us first consider the case of zero baryonic density and suppose that the phase transition from chirality-violating phase to the chirality-conserving one is of the second order. The second-order phase transition is generally characterized by the order parameter η. The order parameter is a thermal average of some operator, which may be chosen in various ways. The physical results are independent of the choice of the order parameter. In QCD, the quark condensate, $\eta = |\langle 0|\bar{u}u|0\rangle| = |\langle 0|\bar{d}d|0\rangle| \geq 0$, may be taken as such a parameter. In the confinement phase, the quark condensate is nonzero, while in the deconfinement phase, it is vanishing.

The quark condensate has the desired properties: as was demonstrated in the chiral effective theory [8, 9], η

decreases with increasing temperature and an extrapolation of the curve $\eta(T)$ to higher temperatures indicates that η vanishes at $T = T_c^{(0)} \approx 180$ MeV. Here, the superscript "0" indicates that the critical temperature is taken at zero baryon density. The same conclusion follows from the lattice calculations [3, 6, 10], where it was also found that the chiral condensate η decreases with an increase of the chemical potential [11, 12].

Apply the general theory of the second-order phase transitions [13] and consider the thermodynamical potential $\Phi(\eta)$ at the temperature T near $T_c^{(0)}$. Since η is small in this domain, $\Phi(\eta)$ may be expanded in η:

$$\Phi(\eta) = \Phi_0 + \frac{1}{2}A\eta^2 + \frac{1}{4}B\eta^4, \quad B > 0. \tag{1}$$

For the moment, we neglect possible derivative terms in the potential.

The terms proportional to η and η^3 vanish for general reasons [13]. In QCD with massless quarks, the absence of η and η^3 terms can be proved for any perturbative Feynman diagrams. At small $t = T - T_c^{(0)}$, the function $A(t)$ is linear in t: $A(t) = at$, $a > 0$. If $t < 0$, the thermodynamical potential $\Phi(\eta)$ is minimal at $\eta \neq 0$, while at $t > 0$, the chiral condensate vanishes, $\eta = 0$. At small t, the t dependence of the coefficient $B(t)$ is insignificant and may be neglected. The minimum, $\bar{\eta}$, of the thermodynamical potential can be found from the condition, $\partial\Phi/\partial\eta = 0$:

$$\bar{\eta} = \begin{cases} \sqrt{-at/B}, & t < 0; \\ 0, & t > 0. \end{cases} \tag{2}$$

It corresponds to the second-order phase transition, since the potential is quartic in η and, if the derivative

---

[¶]This article was submitted by the authors in English.

terms are included in the expansion, the correlation length becomes infinite at $T = T_c^{(0)}$.

Turn now to the case of finite but small baryon density ρ (by ρ, we mean here the sum of baryon and antibaryon densities). For the moment, consider only one type of baryon, i.e., the nucleon. The temperature of the phase transition, T_{ph}, is, in general, dependent on the baryon density, $T_{\mathrm{ph}} = T_{\mathrm{ph}}(\rho)$, with $T_{\mathrm{ph}}(\rho = 0) \equiv T_c^{(0)}$. At $T < T_{\mathrm{ph}}(\rho)$, the term proportional to $E\rho$, where $E = \sqrt{p^2 + m^2}$ is the baryon energy, must be added to thermodynamical potential (1). As was shown in [14, 15], the nucleon mass m (as well as the masses of other baryons) rises due to the spontaneous violation of the chiral symmetry and is approximately proportional to the cubic root of the quark condensate: $m = c\eta^{1/3}$, with $c = (8\pi^2)^{1/3}$ for a nucleon. At small temperatures T, the baryon contribution to Φ is strongly suppressed by the Boltzmann factor $e^{-E/T}$ and is negligible. Below, we assume that the proportionality $m \sim \eta^{1/3}$ is valid in a broad temperature interval. Arguments in favor of such an assumption are based on the expectation that the baryon masses vanish at $T = T_{\mathrm{ph}}(\rho)$ and on dimensional grounds. Near the phase transition point, $E = \sqrt{p^2 + m^2} \approx p + c^2\eta^{2/3}/2p$. At $\eta \longrightarrow 0$, all baryons are accumulating near zero mass and a summation over all baryons gives us, instead of Eq. (1), the following:

$$\Phi(\eta, \rho) = \Phi_0 + \frac{1}{2}at\eta^2 + \frac{1}{4}B\eta^4 + C\eta^{2/3}\rho, \qquad (3)$$

where $C = \sum_i c_i^2/2p_i$. The term $\rho\sum_i p_i$ is absorbed into Φ_0 since it is independent on the chiral condensate η. The typical momenta are of the order of the temperature, $p_i \sim T$. Thus, Eq. (3) is valid in the region $\eta \ll T^3$. In the leading approximation, the term C can be considered to be independent of the temperature at $T \sim T_c^{(0)}$.

Due to the last term in Eq. (3), the thermodynamical potential *always* has a local minimum at $\eta = 0$, since the condensate η is always nonnegative. At small $t < 0$, there also exists a local minimum at $\eta > 0$, which is a solution of the equation

$$\frac{\partial \Phi}{\partial \eta} \equiv (at + B\eta^2)\eta + \frac{2}{3}C\rho\eta^{-1/3} = 0. \qquad (4)$$

At small enough baryon density ρ, Eq. (4) (visualized in Fig. 1a) has, in general, two roots, $\eta_1 < \eta_0$ and $\eta_2 > \eta_0$, where $\eta_0 = (-at/3B)^{1/2}$ is the minimum of the first term in the right-hand side of Eq. (4). The calculation of the second derivative $\partial^2\Phi/\partial\eta^2$ shows that the second root η_2 (if it exists) corresponds to a minimum of $\Phi(\eta)$ and, therefore, is a local minimum of Φ. The point $\eta = \eta_1$ corresponds to a local maximum of the thermodynamical potential since, at this point, the second derivative is always nonpositive.
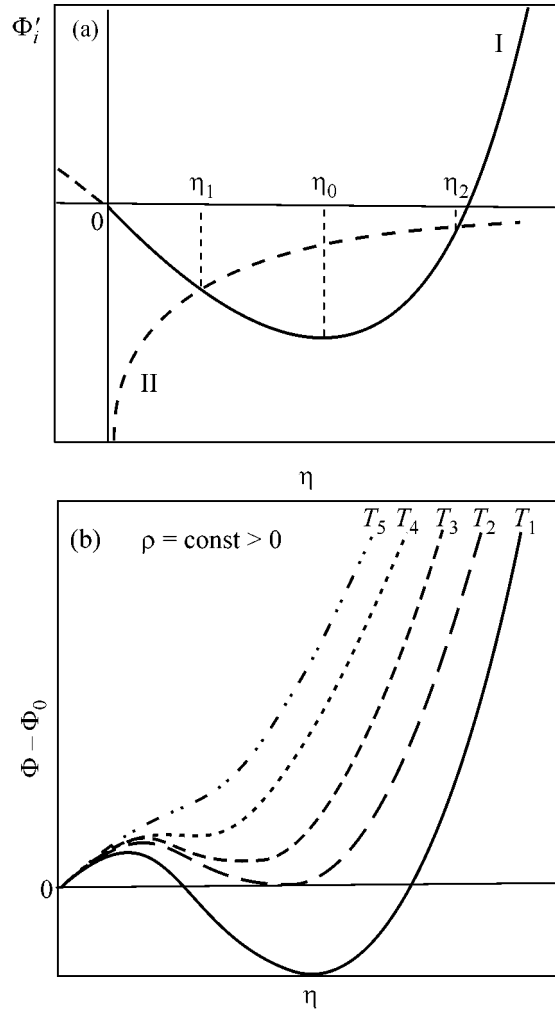
Fig. 1. (a) Graphical representation of Eq. (4): I is the first term and II the second term (with the opposite sign) in the right-hand side of the equation. (b) The thermodynamic potential (3) vs. the chiral condensate at a fixed baryon density $\rho > 0$. At low enough temperatures, $T = T_1$, the system resides in the chirally broken (hadron) phase. The first-order phase transition to the quark phase takes place at $T_{\mathrm{ph}} = T_2 > T_1$. At somewhat higher temperatures, $T_3 > T_{\mathrm{ph}}$, the system is in a mixed state. The temperature $T_4 \equiv T_{\mathrm{cont}}$ corresponds to a continuous transition to the pure quark phase, in which the thermodynamic potential has the form T_5.

The thermodynamical potential $\Phi(\eta, \rho)$ at (fixed) nonzero baryon density ρ has the form plotted in Fig. 1b. At low enough temperatures (curve T_1), the potential has a global minimum at $\eta > 0$ and the system resides in the chirally broken (hadron) phase. As the temperature increases, the minima at $\eta = 0$ and $\eta = \bar{\eta}_2 > 0$ become equal in height (curve $T_2 \equiv T_{\mathrm{ph}}$). At this point, the first-order phase transition to the quark phase takes place. At somewhat higher temperatures, $T = T_3 > T_{\mathrm{ph}}$, the $\eta > 0$ minimum of the potential still exist but $\Phi(\eta = 0) < \Phi(\bar{\eta}_2)$. This is a mixed phase, in which the bubbles of the hadron phase may still exist. However, as
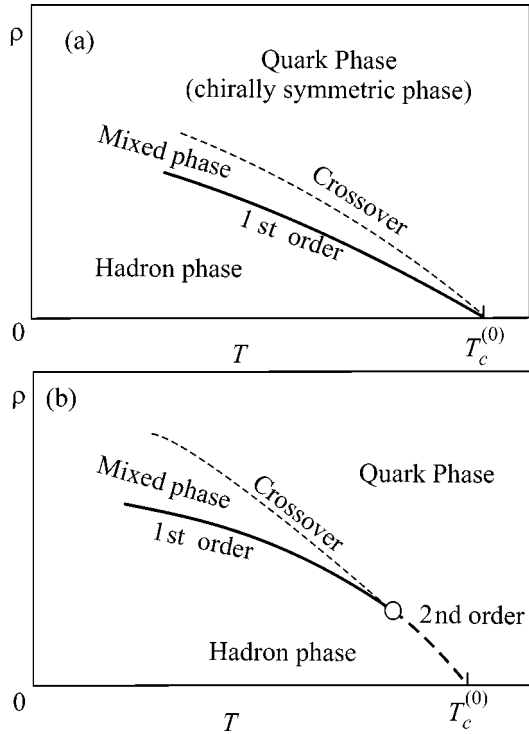
Fig. 2. The qualitative phase diagram at finite baryon density and temperature based on the analysis (a) without and (b) with indication of the approximate second-order transition domain.

the temperature increases further, the second minimum disappears (curve $T_4 \equiv T_{\text{cont}}$). This temperature corresponds to a continuous transition to the pure quark phase, in which the thermodynamic potential has the form T_5.

Let us calculate the temperature of the phase transition, $T_{\text{ph}}(\rho)$, at nonzero baryon density ρ. The transition corresponds to the curve T_2 in Fig. 1b, which is defined by the equation $\Phi(\bar{\eta}_2, \rho) = \Phi(\eta = 0, \rho)$, where $\bar{\eta}_2$ is the second root of Eq. (4) as discussed above. The solution is

$$T_{\text{ph}}(\rho) = T_c^{(0)} - \frac{5}{a}\left(\frac{2C\rho}{3}\right)^{3/5}\left(\frac{B}{4}\right)^{2/5}, \quad (5)$$

and the second minimum of the thermodynamic potential is at $\bar{\eta}_2 = (4a(T^{(0)} - T_{\text{ph}}(\rho))/5B)^{1/2}$.

At a temperature slightly higher than $T_{\text{ph}}(\rho)$, the potential is minimal at $\eta = 0$, but it also has an unstable minimum at some $\eta > 0$. The existence of metastable state is also a common feature of the first-order phase transition (e.g., the overheated liquid in the case of a liquid–gas system). With a further increase of the density ρ (at a given temperature), the intersection of the two curves in Fig. 1a disappears and the two curves only touch one another at one point, $\eta = \bar{\eta}_4$. At this temperature, a continuous transition (crossover) takes

place. The corresponding potential has the characteristic form denoted as T_4 in Fig. 1a. The temperature $T_4 \equiv T_{\text{cont}}$ is defined by the condition that the first (4) and the second derivatives of Eq. (3) vanish,

$$T_{\text{cont}}(\rho) = T_c^{(0)} - \frac{5}{a}\left(\frac{2C\rho}{9}\right)^{3/5}\left(\frac{B}{2}\right)^{2/5}, \quad (6)$$

and the value of the chiral condensate, where the second local minimum of the potential disappears, is given by $\bar{\eta}_4 = (2a(T_{\text{cont}}(\rho) - T_c^{(0)})/5B)^{1/2}$. At temperatures $T > T_{\text{cont}}(\rho)$, the potential has only one minimum and the matter is in the state with the restored chiral symmetry. Thus, in QCD with massless quarks, the type of phase transition with the restoration of the chiral symmetry strongly depends on the value of baryonic density ρ. At a fixed temperature, $T < T_c^{(0)}$, the phase transition occurs at a certain critical density, ρ_{ph}. According to Eq. (5), the critical density has a kind of a "universal" dependence on the temperature, $\rho_{\text{ph}}(T) \propto [T_c^{(0)} - T]^{5/3}$, the power of which does not depend on the parameters of the thermodynamic potential, a and B.

The expected phase diagram is shown qualitatively in Fig. 2a. This diagram does not contain an endpoint, which was found in lattice simulations of the QCD with a finite chemical potential [16, 17]. We expect that this happens because, in our approach, a possible influence of the confinement on the order of the chiral restoration transition was ignored. Intuitively, it seems that, at low baryon densities, such an influence is absent indeed: the deconfinement phenomenon refers to the large quark–antiquark separations, while the restoration of the chiral symmetry appears due to fluctuations of the gluonic fields in the vicinity of the quark. However, the confinement phenomenon dictates the value of the baryon size, which cannot be ignored at high baryon densities, when the baryons are overlapping. If the melting of the baryons occurs in the hadron phase depicted in Fig. 2a, then, at high enough density, the nature of the transition could be changed. This may give rise to the appearance of the endpoint observed in [16, 17]. The domain where the inequality $|at| \gg C\rho\eta^{2/3}$, $\rho \neq 0$, is fulfilled has specific features. In this domain, the phase transition looks like a smeared second-order phase transition: the specific heat has (approximately) a discontinuity at the phase transition point, $\Delta C_p = a^2 T_c/B$. The correlation length increases as $(T - T_c^{(0)})^{-1/2}$ at $T - T_c^{(0)} \longrightarrow 0$. The latter rises if we include the derivative terms in the effective thermodynamical potential. The phase diagram with this domain indicated may appear as shown in Fig. 2b. Note that the applicability of our considerations is limited to the region $|T - T_c^{(0)}|/T_c^{(0)} \ll 1$ and low baryon densities.

In real QCD, the massive heavy quarks (the quarks c, b, t) do not influence on this conclusion, since their

concentration in the vicinity of $T \approx T_c^{(0)} \sim 200$ MeV is small. However, the strange quarks, the mass of which $m_s \approx 150$ MeV is just of order of expected $T_c^{(0)}$, may change the situation. This problem deserves further investigation.

REFERENCES

1. A. V. Smilga, in *At the Frontier of Particle Physics: Handbook of QCD, Boris Ioffe Festschrift*, Ed. by M. Shifman (World Sci., Singapore, 2001), Vol. 3, p. 2033.

2. K. Rajagopal and F. Wilczek, in *Handbook of Quantum Chromodynamics*, Ed. by M. Shifman (World Sci., Singapore, 2001), Vol. 3, p. 2061.

3. F. Karsch, Phys. Rev. D **49**, 3791 (1994).

4. F. Karsch and E. Laermann, Phys. Rev. D **50**, 6954 (1994).

5. S. Aoki *et al.* (JLQCD Collab.), Phys. Rev. D **57**, 3910 (1998).

6. A. Ali Khan *et al.* (CP-PACS Collab.), Phys. Rev. D **63**, 034502 (2001).

7. I. I. Kogan, A. Kovner, and B. Tekin, Phys. Rev. D **63**, 116007 (2001).

8. H. Leutwyler, Nucl. Phys. B (Proc. Suppl.) **4**, 248 (1988).

9. P. Gerber and H. Leutwyler, Nucl. Phys. B **321**, 387 (1989).

10. F. Karsch, Nucl. Phys. A **590**, 367C (1995).

11. J. B. Kogut, D. K. Sinclair, S. J. Hands, and S. E. Morrison, Phys. Rev. D **64**, 094505 (2001).

12. J. B. Kogut, D. Toublan, and D. K. Sinclair, Nucl. Phys. B **642**, 181 (2002).

13. L. D. Landau and E. M. Lifshitz, *Course of Theoretical Physics*, Vol. 5: *Statistical Physics*, 3rd ed. (Nauka, Moscow, 1976; Pergamon Press, Oxford, 1980), Part 1.

14. B. L. Ioffe, Nucl. Phys. B **188**, 317 (1981); Nucl. Phys. B **191**, 591(E) (1981).

15. V. M. Belyaev and B. L. Ioffe, Zh. Éksp. Teor. Fiz. **83**, 876 (1982) [Sov. Phys. JETP **56**, 493 (1982)]; Zh. Éksp. Teor. Fiz. **84**, 1236 (1983) [Sov. Phys. JETP **57**, 716 (1983)].

16. Z. Fodor and S. D. Katz, J. High Energy Phys. **0203**, 014 (2002).

17. Z. Fodor and S. D. Katz, hep-lat/0402006.

Electromagnetoacoustic Transparency of a Paramagnetic Crystal

A. V. Gulakov and S. V. Sazonov*

Kaliningrad State University, Kaliningrad, 236041 Russia
*e-mail: nst@alg.kaliningrad.ru
Received April 15, 2004

The possibility of synchronously controlling the hypersound and light propagation in a low-temperature paramagnet under the action of a high-power resonance optical pumping is studied theoretically. The effect combines the properties of electromagnetic and acoustic induced transparencies. It is shown that, for certain values of control parameters (external electric field strength and pumping intensity), the paramagnet may become transparent simultaneously to light and sound. The group velocities of sound and light may become comparable in magnitude. © 2004 MAIK "Nauka/Interperiodica".

PACS numbers: 42.50.Gy; 32.80.Qk; 43.25.Ed

Historically, after the discovery of optical coherent effects, their acoustic analogues were discovered within a few years. For example, acoustic self-induced transparency [1, 2] was predicted and discovered a few years after the discovery of optical self-induced transparency [3]. A similar situation took place with electromagnetically induced transparency (EIT) [4–6] and its analogue, i.e., acoustic induced transparency (AIT) [7]. In both cases, a three-level resonant medium becomes transparent at the center of the absorption line under the action of high-power pumping. The main difference between AIT and EIT is the extent to which the group velocity decreases. In the EIT case, this velocity can be six orders of magnitude lower than the velocity of light c in vacuum [4–6], while the decrease in the velocity of sound in the AIT case amounts to only a few tenths of a percent [7]. In the EIT case, the group velocity of light in a medium may become equal to the velocity of sound. Consequently, an effective interaction between light and sound is possible. It was shown, for example, in [8] that, if the velocities of light and sound are close, the Mandelstam–Brillouin scattering changes qualitatively. The question arises: what happens to light and sound in the case of their resonance with the transitions in a single atom? Paramagnetic ions implanted into a crystal matrix are a suitable object for such investigations. It is well known that paramagnetic ions can effectively interact with lattice vibrations, as well as with coherent light [9, 10].

The possibility of coherent propagation of light and hypersound in a system of paramagnetic impurities under the EIT conditions will be discussed in this study.

Let us consider a system of paramagnetic ions situated in a cubic crystal in the form of impurities. It should be emphasized that paramagnetic ions with an effective spin $S = 1$ experience the strongest interaction

with lattice vibrations [9, 10]. When the crystal is placed in an external magnetic field B_0 directed along the z axis (which is one of the fourfold axes of the crystal), the electron ground level splits into three Zeeman sublevels. Examples of such ions are Fe^{2+} and Ni^{2+} ions in the MgO crystal matrix [1, 9, 10]. Optical (probe and pump) fields induce quantum transitions between the given Zeeman triplet and the upper-lying electronic level, which is assumed to be a singlet and, hence, does not exhibit the Zeeman splitting. Let us suppose that high-power resonant electromagnetic pumping occurs at the transition $2 \longleftrightarrow 3$ and weak (electromagnetic and longitudinal acoustic) resonant signal pulses operate at transitions $1 \longleftrightarrow 3$ and $1 \longleftrightarrow 2$, respectively (Fig. 1). The pump and signal pulses propagate at right angles to the external magnetic field along the y axis, which is also a fourfold axis. The characteristic frequencies of acoustic and optical probe fields belong to
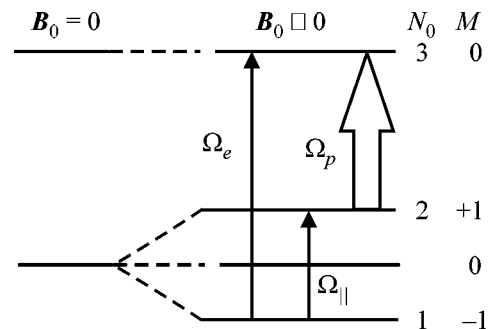
Fig. 1. Energy level diagram for a paramagnetic ion, where N_0 is the level number, M is the magnetic quantum number, and arrows indicate the transitions induced by high-power resonant electromagnetic pumping Ω_p and by the signal components of the electromagnetic (Ω_e) and acoustic ($\Omega_\parallel$) fields.

the ranges $\omega_{21} \sim 10^{11}$–10^{12} s^{-1} and $\omega_{31} \sim 10^{14}$–10^{15} s^{-1}. The pump frequency ω_{32} is close to frequency ω_{31}. We disregard the transition induced by longitudinal relaxation, in which the middle level of the Zeeman triplet is involved; i.e., we can effectively speak of a three-level system, in which all transitions are allowed.

The Hamiltonian of the interaction between an atom and the aforementioned fields has the form

$$\hat{V} = -\hbar\hat{\Omega} = \hbar\begin{pmatrix} \omega_{31} & \tilde{\Omega}_p & \tilde{\Omega}_e \\ \tilde{\Omega}_p & \omega_{21} & \tilde{\Omega}_\| \\ \tilde{\Omega}_e & \tilde{\Omega}_\| & 0 \end{pmatrix}. \qquad (1)$$

Here,

$$\tilde{\Omega}_p = \frac{d_{32}}{\sqrt{2}\hbar}E_p, \quad \tilde{\Omega}_e = \frac{d_{31}}{\sqrt{2}\hbar}E_e, \quad \tilde{\Omega}_\| = -\frac{3G_{11}}{2\hbar}\varepsilon_{yy},$$

where $\hbar$ is the Planck's constant; d_{3j} ($j = 1, 2$) is the dipole moment of transition $j \longleftrightarrow 3$; E_p and E_e are the strengths of the optical pump field and the signal component, respectively; G_{11} is the spin–phonon interaction tensor component, connecting the paramagnetic ion with the longitudinal component of the deformation field [9, 10]; and ε_{yy} is the strain of the crystal under the action of hypersound.

We will use the semiclassical approach [11, 12], in which atoms are described quantum-mechanically with the help of the equation for the density matrix

$$\frac{\partial\hat{\rho}}{\partial t} = -i[\hat{\Omega}, \hat{\rho}], \qquad (2)$$

and fields are described by the classical wave equations [7]. The equations for the acoustic wave and the signal component of the electromagnetic field have the form

$$\frac{\partial\tilde{\Omega}_\|}{\partial t} + a\frac{\partial\tilde{\Omega}_\|}{\partial y} = -\frac{9G_{11}^2 n}{16\hbar\rho}\frac{\partial}{\partial y}\int_{-\infty}^{+\infty}(\rho_{21} + \rho_{21}^*)f(\Delta)d\Delta, \quad (3)$$

$$\frac{\partial\tilde{\Omega}_e}{\partial y} + \frac{1}{c}\frac{\partial\tilde{\Omega}_e}{\partial t} = -\frac{\sqrt{2}\pi n d_{31}^2}{\hbar c^2}\frac{\partial}{\partial t}(\rho_{31} + \rho_{31}^*), \qquad (4)$$

respectively, where a is the velocity of longitudinal sound in a crystal free of paramagnetic impurities, n is the concentration of paramagnetic ions, ρ is the mean density of the crystal, $f(\Delta)$ is the inhomogeneously broadened contour at transition $1 \longleftrightarrow 2$, and Δ is the acoustic frequency detuning from the central frequency of the inhomogeneously broadened contour. We disregard the inhomogeneous broadening of transition $1 \longleftrightarrow 3$, since the transition frequency is much higher than the inhomogeneously broadened width. We assume that the homogeneous broadening is predominant at this transition.

Equations (3) and (4) were derived from the initial wave equations using the procedure for reducing the

equation order from second to first [13], in view of the fact that the concentration of paramagnetic ions is so low that $\eta_\| = 9G_{11}^2 n/8\hbar\omega_{21}\rho a^2 \ll 1$ and $\eta_e = \sqrt{2}d_{31}^2 n/\hbar\omega_{31} \ll 1$. Assuming that $a \approx 5 \times 10^5$ cm/s, $\omega_{31} \sim 10^{14}$ s^{-1}, $\omega_{21} \sim 10^{12}$ s^{-1}, $\rho \approx 2$ g/cm^3, $G_{11} \sim 10^{-13}$ erg, $n \sim 10^{17}$ cm^{-3}, and $d_{31} \sim 10^{-18}$ CGSE units for Ni^{2+} ions in a MgO crystal [1], we obtain $\eta_\| \sim \eta_e \sim 10^{-6}$.

In Eq. (2) for the density matrix, we pass to envelopes by representing the fields acting on an atom and the nondiagonal elements of the density matrix in the form

$$\tilde{\Omega}_p = \Omega_p\exp[i(\omega_{32}t - k_{32}y)] + \text{c.c.},$$

$$\tilde{\Omega}_e = \Omega_e\exp[i(\omega_{31}t - k_{31}y)] + \text{c.c.},$$

$$\tilde{\Omega}_\| = \Omega_\|\exp[i(\omega_{21}t - k_{21}y)] + \text{c.c.}, \qquad (5)$$

$$\rho_{32} = R_{32}\exp[-i(\omega_{32}t - k_{32}y)],$$

$$\rho_{31} = R_{31}\exp[-i(\omega_{31}t - k_{31}y)],$$

$$\rho_{21} = R_{21}\exp[-i(\omega_{21}t - k_{21}y)].$$

Here, Ω_p, Ω_e, $\Omega_\|$, and R_{ij} are slowly varying envelopes and ω_{ij} and k_{ij} are the transition frequencies and the corresponding wave numbers.

For the system of equation to remain consistent, the following synchronism conditions must be satisfied for the acoustic and optical probe waves:

$$\omega_{31} = \omega_{32} + \omega_{21}, \quad k_{31} = k_{32} + k_{21}. \qquad (6)$$

Taking these conditions into account, we can rewrite the system of constitutive Eqs. (2) in the form

$$\dot{\rho}_{22} = -i\Omega_p(R_{32} - R_{32}^*) + i\Omega_\|(R_{21} - R_{21}^*) \\ - \Gamma(\rho_{22} - W_2),$$

$$\dot{\rho}_{11} = -i\Omega_e(R_{31} - R_{31}^*) - i\Omega_\|(R_{21} - R_{21}^*) \\ - \Gamma(\rho_{11} - W_1),$$

$$\dot{R}_{32} = -i(\Delta_{32} - i\gamma_{32})R_{32} + i\Omega_p(\rho_{33} - \rho_{22}) \\ - i\Omega_e R_{21}^* + i\Omega_\| R_{31}, \qquad (7)$$

$$\dot{R}_{31} = -i(\Delta_{31} - i\gamma_{31})R_{31} - i\Omega_p R_{21} \\ + i\Omega_e(\rho_{33} - \rho_{11}) + i\Omega_\| R_{32},$$

$$\dot{R}_{21} = -i(\Delta_{21} - i\gamma_{21})R_{21} - i\Omega_p R_{31} \\ + i\Omega_e R_{32}^* + i\Omega_\|(\rho_{22} - \rho_{11}),$$

where Γ is the relaxation rate for diagonal elements (for simplicity, we use here the approximation of a single longitudinal relaxation time); γ_{ij} are the transverse relaxation rates at corresponding transitions; Δ_{ij} are the detunings of field frequencies from the atomic frequencies; and W_i are equilibrium populations of quantum
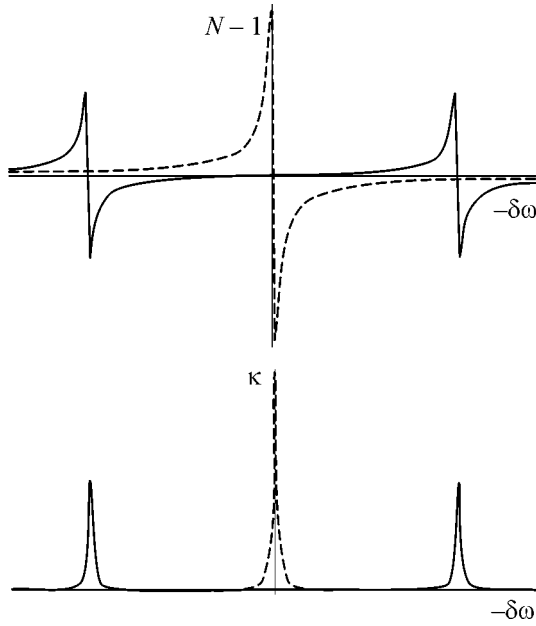
Fig. 2. Schematic diagram of the profiles of refractive index (upper graph) and absorption coefficient (lower graph) of hypersound and light in the absence (dashed curves) and presence (solid curve) of a high-power resonant electromagnetic pumping.

levels, which satisfy the following condition: $W_1 + W_2 = \rho_{11} + \rho_{22} + \rho_{33} = \text{const} \leq 1$. The equilibrium population W_3 of the third level can be set to zero. The middle level of the Zeeman triplet is occupied; however, we disregard the change in its population because of the relaxation process.

We consider the steady-state regime, where the left-hand side of equations in system (7) can be assumed to be zero. In addition, we take into account only the linear contribution Ω_e and $\Omega_\parallel$. As a result, assuming that $\Gamma \ll \gamma_{31}$ and $\Omega_p \geq \gamma_{32}, \gamma_{31}$, we obtain

$$R_{21} = -\frac{W_1 - W_2}{\alpha_{21}\alpha_{31} - \Omega_p^2}(\alpha_{31}\Omega_\parallel - \Omega_p\Omega_e), \qquad (8)$$

$$R_{31} = -\frac{W_1 - W_2}{\alpha_{21}\alpha_{31} - \Omega_p^2}(\alpha_{21}\Omega_e - \Omega_p\Omega_\parallel), \qquad (9)$$

where $\alpha_{ij} = \Delta_{ij} - i\gamma_{ij}$. To take into account the inhomogeneous broadening at transition $1 \longleftrightarrow 2$, we assume that the contour has the Lorentzian shape: $f(\Delta) = (\gamma/\pi)/(\gamma^2 + \Delta^2)$, where γ^{-1} is the dephasing time for elements ρ_{21} due to inhomogeneous broadening. We assume that $\Delta_{21} = \Delta + \delta\omega_{21}$, where $\delta\omega_{21}$ is the hypersound detuning from the center of the inhomogeneously broadened contour. As a result of integration with respect to detunings, and assuming that $\gamma \gg \gamma_{21}$ [1, 10], we arrive at the conclusion that the expression for R_{21} is formally preserved to within the substitution $\alpha_{21} \longrightarrow \beta_{21}$, where $\beta_{21} = \delta\omega_{21} - i\gamma$.

Substituting the obtained expressions for the elements of the density matrix into wave equations (3) and (4) and taking into account relations (5), we obtain the dispersion relation

$$
\begin{aligned}
(1 - \eta_\parallel\omega_{21}\alpha\alpha_{31})k^2 &- \left[\left(\frac{\omega_{31}}{c} + \frac{\omega_{21}}{a}\right)\right. \\
&+ \alpha\frac{\omega_{31}}{c}(\eta_e\omega_{31}\beta_{21} - \eta_\parallel\omega_{21}\alpha_{31} \\
&\left. - \eta_e\omega_{31}\eta_\parallel\omega_{21}(W_1 - W_2))\right]k \\
&+ \frac{\omega_{31}\omega_{21}}{ca}(1 + \eta_e\omega_{31}\alpha\beta_{21}) = 0,
\end{aligned}
\qquad (10)
$$

where the complex quantity α is defined as

$$\alpha = \frac{W_1 - W_2}{\alpha_{21}\alpha_{31} - \Omega_p^2}.$$

By solving this quadratic equation and neglecting the products $\eta_e\eta_\parallel$ as squares of small parameters, we obtain two independent dispersion branches, namely, optical k_e and acoustic $k_\parallel$:

$$
\begin{aligned}
k_e &= \frac{\omega_{31}}{c}(1 + \eta_e\omega_{31}\alpha\beta_{21}), \\
k_\parallel &= \frac{\omega_{21}}{a}(1 + \eta_\parallel\omega_{21}\alpha\alpha_{31}).
\end{aligned}
\qquad (11)
$$

In the dispersion equation, we managed to separate the optical and acoustic branches owing to the low concentration of paramagnetic impurities. For an arbitrary concentration, two photon–phonon dispersion branches are obtained from relations (11). Under these conditions, in contrast to our case, the properties of light cannot be separated from the properties of hypersound.

After the use of the second condition (6) and separation of the real and imaginary parts, we determine the relations connecting the detunings and the frequencies of the optical and acoustic probe fields:

$$\omega_{21} = \frac{8\sqrt{2}\pi d_{31}^2\rho a^3\gamma}{9G_{11}^2 c\gamma_{31}}\omega_{31}, \quad \delta\omega_{21} = \frac{\gamma}{\gamma_{31}}\Delta_{31}. \quad (12)$$

The first condition from (12) can be satisfied by varying magnetic field B_0 and, hence, by varying the transition frequency $\omega_{21}^{(0)} = g\mu_B B_0/\hbar$ (g is the Landé factor and μ_B is the Bohr magneton). The absorption curves for these waves completely coincide, while the dispersion curve for the electromagnetic wave is displaced upwards relative to the dispersion curve for sound by the constant $\omega_{31}/c - \omega_{21}/a$ (Fig. 2). The expressions for the group velocities $1/v_g = \partial k/\partial\omega$ can be obtained from relations (11) taking into account relation (12). We write these expressions for zero detunings, assuming that temperature T is much lower than $\hbar\omega_{21}/k_B$, where k_B is the

Boltzmann constant. In this case, we can assume that, prior to the action of pulses, only the ground level was populated; i.e., $W_1 = 1$ and $W_2 = 0$. Setting $\omega_{21} \sim 10^{12}$ s^{-1}, we draw the conclusion that this condition holds at $T \ll 10$ K. Then, for the group velocities of light and sound, we obtain

$$\frac{1}{v_{ge}} = \frac{1}{c} + \frac{\kappa}{\gamma_{31}}, \quad \frac{1}{v_{g\parallel}} = \frac{1}{a} + \frac{\kappa}{\gamma}, \quad (13)$$

respectively, where the absorption coefficients are given by

$$\kappa = \kappa_e = \kappa_\parallel = \frac{\omega_{31}^2 \eta_e \gamma}{c(\gamma\gamma_{31} + \Omega_p^2)} = \frac{\omega_{21}^2 \eta_\parallel \gamma_{31}}{a(\gamma\gamma_{31} + \Omega_p^2)}. \quad (14)$$

Relations (13) exactly coincide with the Loudon formula [14, 15] for the energy transfer rate.

Let us estimate the absorption lengths and the group velocities in the presence and absence of pumping. We consider two cases. In the first case, we use the parameters of medium for Ni^{2+} ions in a MgO crystal considered above and assume that [1] $\omega_{31} \sim 10^{14}$ s^{-1}, $\gamma \sim 10^8$ s^{-1}, $\gamma_{31} \approx 6 \times 10^7$ s^{-1}, and $\Omega_p \approx 4 \times 10^9$ s^{-1}, which corresponds to intensity $I \sim 10^{10}$ W/cm^2. Using relations (13), we obtain $\omega_{21} \sim 10^{12}$ s^{-1}. Under these conditions, the absorption coefficients for longitudinal sound and the signal component of the electromagnetic field are $\kappa \approx 10$ cm^{-1} in the presence of pumping and $\kappa_0 \approx 2 \times 10^4$ cm^{-1} in its absence ($\Omega_p = 0$). The corresponding absolute absorption lengths are $l \approx 0.1$ cm and $l_0 \approx 4 \times 10^{-5}$ cm. It can be seen that, in the presence of high-power pumping, the absorption length increases by three orders of magnitude, reaching a value of 1 mm. In this case, the group velocities of light and sound are $v_{ge} \approx 6 \times 10^6$ cm/s, $c/v_{ge} \approx 5 \times 10^3$, $v_{g\parallel} \approx 4.8 \times 10^5$ cm/s, $a/v_{g\parallel} \approx 1.05$. Thus, pumping creates a transparency region for the signal optical and acoustic components of the pulse. Light is slowed down by four orders of magnitude, while the velocity of sound virtually remains unchanged (its relative variation does not exceed 5%). However, in this case the absorption length is small. For this reason, we consider the second case, where light is slowed down to a smaller extent, but the absorption length is larger. We assume that the pumping intensity is $I \sim 10^{11}$ W/cm^2, i.e., $\Omega_p \sim 10^{10}$ s^{-1}. Then, the absolute absorption lengths are $l \sim 1$ cm and $l_0 \approx 4 \times 10^{-5}$ cm. For the group velocities, we obtain in this case $v_{ge} \approx 4 \times 10^7$ cm/s, $c/v_{ge} \approx 700$, $v_{g\parallel} \approx 5 \times 10^5$ cm/s, and the relative change in the velocity of sound is smaller than 1%.

Thus, we have predicted the propagation regime in which high-power electromagnetic pumping makes it possible to produce a transparency region for resonant light and sound. Under these conditions, the propagation of light and sound can be controlled simultaneously. In this case, the group velocity of the probe's electromagnetic component is substantially slowed down, unlike the acoustic component. This circumstance can be used to obtain synchronous propagation of light and hypersound in a system of paramagnetic impurities. In this case, the optical and acoustic waves can exchange energy, which can result in the formation of the coupled photon–phonon states. To describe such phenomena, it is necessary to take into account nonlinear effects in the propagation of optical and acoustic signal fields, as was done in [16] for EIT.

REFERENCES

1. N. S. Shiren, Phys. Rev. B **2**, 2471 (1970).
2. G. A. Denisenko, Zh. Éksp. Teor. Fiz. **60**, 2269 (1971) [Sov. Phys. JETP **33**, 1220 (1971)].
3. S. L. McCall and E. L. Hahn, Phys. Rev. Lett. **18**, 908 (1967).
4. K. J. Boller, A. Imamoglu, and S. E. Harris, Phys. Rev. Lett. **66**, 2593 (1991).
5. S. E. Harris, Phys. Rev. Lett. **70**, 552 (1993).
6. S. E. Harris, Phys. Today **50** (7), 36 (1997).
7. S. V. Sazonov, Pis'ma Zh. Éksp. Teor. Fiz. **76**, 176 (2002) [JETP Lett. **76**, 143 (2002)].
8. A. B. Matsko, Y. V. Rostovtsev, M. Fleischhauer, and M. O. Scully, Phys. Rev. Lett. **86**, 2006 (2001).
9. J. W. Tucker and V. W. Rampton, *Hypersound in Solid State Physics* (North-Holland, Amsterdam, 1972; Mir, Moscow, 1975).
10. S. A. Altshuler and B. M. Kozyrev, *Electron Paramagnetic Resonance of Transition Compounds* (Nauka, Moscow, 1972; Halsted, New York, 1975).
11. S. V. Sazonov, J. Phys.: Condens. Matter **6**, 6295 (1994).
12. S. V. Sazonov, Zh. Éksp. Teor. Fiz. **118**, 20 (2000) [JETP **91**, 16 (2000)].
13. M. B. Vinogradova, O. V. Rudenko, and A. P. Sukhorukov, *Theory of Waves*, 2nd ed. (Nauka, Moscow, 1990) [in Russian].
14. R. Loudon, *Quantum Theory of Light* (Clarendon Press, Oxford, 1973; Mir, Moscow, 1976).
15. S. Chu and S. Wong, Phys. Rev. Lett. **48**, 738 (1982).
16. N. A. Zharova, A. G. Litvak, and V. A. Mironov, Pis'ma Zh. Éksp. Teor. Fiz. **79**, 330 (2004) [JETP Lett. **79**, 272 (2004)].

Translated by N. Wadhwa

Structure of Light Scattering Spectra in Opal Photonic Crystals

S. G. Romanov

Ioffe Physicotechnical Institute, Russian Academy of Sciences, St. Petersburg, 194021 Russia
e-mail: sergeiromanov@list.ru
Received March 22, 2004; in final form, April 29, 2004

Spectra of light losses are studied at a fixed angle of incidence of a collimated beam on the surface of an opal anisotropic photon crystal at various observation angles. It is shown that the structure of the forward- and back-scattered light spectra is connected with the existence of several directional photonic forbidden bands. It is demonstrated that back scattering is enhanced and forward scattering is suppressed in the frequency region of photonic forbidden bands. It is suggested that a scattering band associated with photon localization at the photonic gap edge is observed. © *2004 MAIK "Nauka/Interperiodica"*.

PACS numbers: 42.25.Fx; 42.70.Qs

Light penetration from the free space into a photonic crystal (PhC) depends on the excitation of PhC eigenmodes by the light wave. This process is determined by the PhC symmetry, the direction of the beam incidence, and the light polarization. However, some of the PhC modes remain unexcited. Because the process of binding occurs through multiple scattering, a certain fraction of the incident electromagnetic (EM) wave intensity is lost in this case. On the contrary, photons scattered by defects inside a uniform PhC are transferred by all its modes. A comparison of the photon band structure parameters obtained from experiment with respect to external and internal light sources is of undoubted interest. The introduction of an additional light source into a PhC is connected with significant technological difficulties, and the data obtained are a complicated function of the emitter position in the unit cell, excitation conditions, and the spectral composition of radiation. An alternative source—lattice defects—leads to the appearance of modes that are not eigenmodes of a perfect lattice. As a result, radiation in a nonideal lattice is transferred by both diffuse and ballistic mechanisms. It is evident that this disadvantage is inherent in any experimentally designed PhCs because of their non-ideal ordering.

For a low concentration of defects, a borderline situation exists where the modes of PCs with perfectly packed and slightly disordered lattices differ insignificantly. Here, elastic scattering can be considered as a perturbation resulting in a photon jump to another eigenmode of the ordered PhC, that is, in redistribution of the light flux inside the PhC. Photonic band gaps (PBGs) are generated because of the formation of spatially closed photon trajectories [1]. Because scattering to free-space modes is insignificant in three-dimensional (3D) PhCs, this fact predetermines a strong lattice effect on the scattered light. In particular, in the case of a directional PBG, it could be expected that scattering depends on the observation direction because of the anisotropy of the PhC itself.

An artificial opal is a model 3D PhC with a directional PBG. In recent years, opal films were synthesized with a concentration of defects reduced by a factor of more than 100, as compared with jewelry opals [2]. These opals had as few as one defect per 100 unit cells [3]. In opal films, the mean free path of photons is comparable with or exceeds the crystal thickness, that is, ballistic photon propagation predominates. Hence, a substantial fraction of the scattered light is transferred by singly scattered photons [5], which behave as photons emitted by an internal source radiating in accordance with the PhC symmetry [4].

The known data on the effect of defects on light propagation in opals are related mainly to bulk opals with a high defect density [6, 7, 4], whereas the scattered light itself has seldom been a subject of investigation [6, 8]. Nevertheless, important parameters have been determined in recent studies, such as the light attenuation length in the opal PBG and the mean free path of photons outside the PBG. At present, data on film opals are fragmentary [9]. Our experiments demonstrated that scattered light spectra in bulk and film opals are radically different. For example, the structure of forward-scattered light spectra in films is determined by the PBG in the incidence and detection directions [5], whereas only the PBG in the exit direction is important in bulk opals [4].

In this work, a connection of the scattering spectra with the ordering of the opal lattice is demonstrated. The structure of back-scattered and forward-scattered light spectra is considered, and spectral features of the scattered light are compared with the transmission spectra as functions of the orientation of the opal lattice.
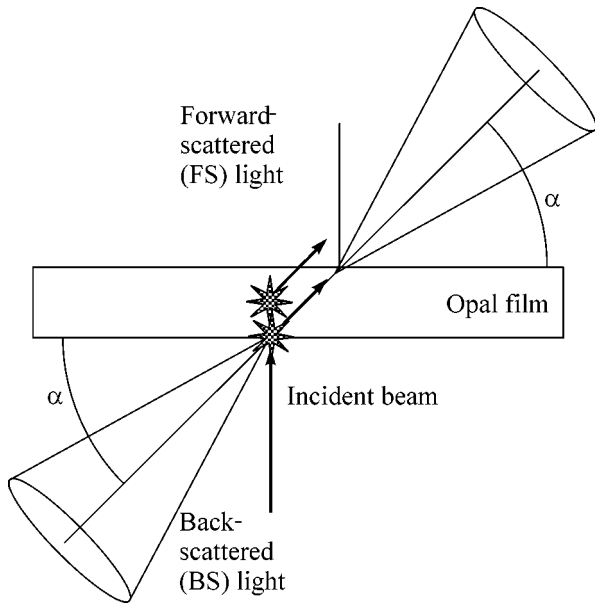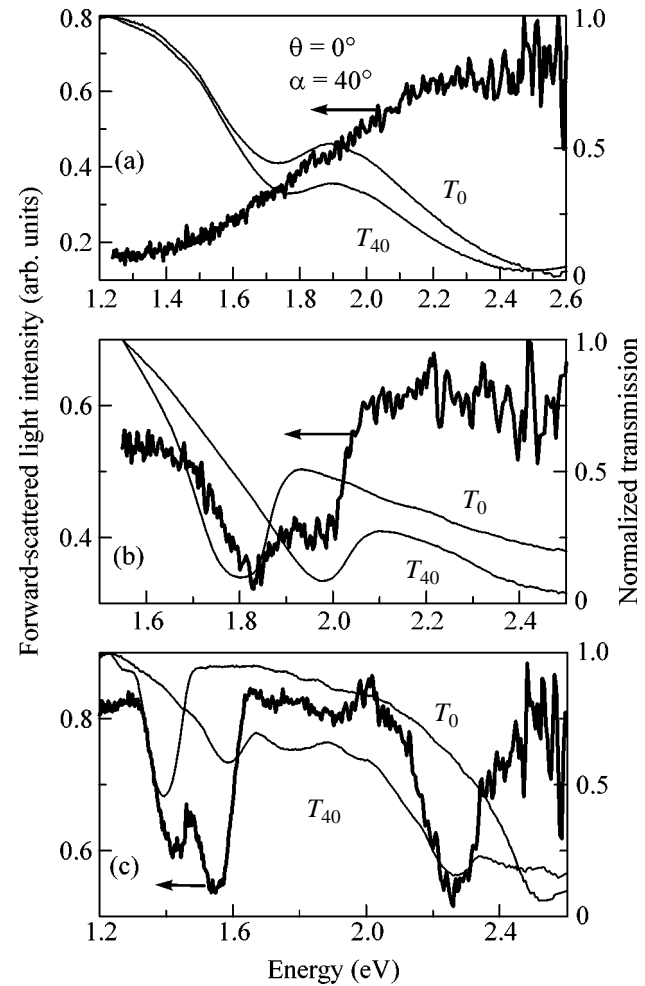
Fig. 1. Schematic diagram of the collection of forward- and back-scattered light at light incidence perpendicular to the opal film surface. Beam refraction at interfaces is not shown.

Fig. 2. Panels (a), (b), and (c), respectively, show forward-scattering (FS) spectra at $\theta = 0°$ and $\alpha = 40°$ for films of three types (thickened lines) in comparison with their transmission (T) spectra for (T_0) $\theta = 0°$ and (T_{40}) $\theta = 40°$.

Opal films were prepared either by drying a suspension of polymer spheres of the same diameter on a glass substrate or by crystallization in a meniscus upon pulling the substrate out of the suspension. Annealing at 80°C is used to stabilize opal. In both cases, the spheres are crystallized into a face-centered cubic lattice with the (111) growth plane parallel to the substrate. The films crystallized in the meniscus have a more perfect lattice, which is confirmed by the observation of a surface diffusion pattern [10]. For comparison, samples of three types were selected. Two of them were prepared by drying under either normal conditions (type 1) or increased humidity (type 2), and the other was prepared by crystallization in a meniscus (type 3). The diameters of spheres were 325, 300, and 348 nm for films of types 1, 2, and 3, respectively.

The measurements of light-scattering spectra were carried out upon illuminating the sample with a halogen incandescent lamp, whose light was collected into a parallel beam 1 mm in diameter. The FS and BS spectra were measured at the normal incidence of the probe beam ($\theta = 0°$). The scattered light was collected from a cone with a cone angle of about 10°. The angle α between the cone axis and the [111] axis of the opal lattice was varied at a step of 5° from 0° to 85° in forward scattering and from 35° to 85° in back scattering (Fig. 1). The light transmission was measured in a standard configuration, where the angle of incidence was equal to the angle of transmission, $\theta = \alpha$. The opal lattice was oriented in the type 3 film using the surface diffraction pattern in such a way that the angle of detection varied along the LKL' direction of the Brillouin zone [9].

The scattering act, which changes the photon propagation direction, can occur both at the entrance into the PhC and at a defect inside the PhC. Because of the small film thickness and the macroscopic method of light collection, the contributions to the detected signal from these two sources were not separated experimentally.

FS spectra obtained for angles $\theta = 0°$ and $\alpha = 40°$ for opals differing in the degree of ordering are compared with their transmission spectra for $\theta = 0°$ and 40° in Fig. 2. Assuming that the relative width of the PBG minimum $\Delta\omega/\omega_{0n}$, where $\hbar\omega_{0n}$ is the central frequency of the nth PBG in the transmission spectrum, is directly related to the lattice crystallinity, one can point to the ordering dependence of the scattering spectra. In the case of a weakly ordered opal film of type 1 (Fig. 2a), the (111) PBG minimum had $\Delta\omega/\omega_{01} \approx 0.17$, and its position weakly depends on the angle. It turned out that the FS spectrum of this sample had no features associated with the PBG. In the case of a more perfect lattice

of the type 2 opal with $\Delta\omega/\omega_{01} \approx 0.095$ (Fig. 2b), the FS spectrum has a split minimum for a certain observation angle. The position of its bands coincides well with $\hbar\omega_0$ of the PBG along the directions of light incidence and detection. The spectrum of the type 3 opal (Fig. 2c) is formed even better. It has $\Delta\omega/\omega_{01} \approx 0.08$, which is close to the theoretical value $\Delta\omega/\omega_{01} \approx 0.063$ [11]. The bands in the FS spectrum of this opal are comparable with the width of minima in the transmission spectrum.

The losses due to forward scattering in weakly ordered films grow with increasing frequency. On the contrary, the intensity of the FS light in films with a lower concentration of defects does not vary over the spectrum outside the PBG, counting in favor of the predominance of the frequency-independent scattering mechanism. This behavior excludes from consideration Rayleigh scattering, which is assumed to be the main mechanism of losses in weakly ordered opals [3].

Light passed through a medium with disorder has ballistic and diffuse components. If the mean free path exceeds the film thickness, then even a singly scattered photon can reach the detector ballistically. In this case, it can be considered that singly scattered photons carry information on the directional PBG, rather than the ballistic component of the transmission spectrum. Thus, the FS light spectrum along a certain direction is composed of singly and multiply scattered photons. The spectrum of singly scattered photons has an intensity modulation in accordance with the spectral position of the PBG [5], whereas multiply scattered photons compose a structureless background. In compliance with this fact, the differences in the FS spectra of opals of types 1, 2, and 3 are due to the masking contribution of the diffuse component. In the subsequent discussion, I will consider only the spectra of type 3 samples, because these spectra exhibit the lowest diffuse component.

It is natural to compare the scattering spectra with the opal transmission spectra. The minima of the transmission spectra in the LKL' direction correspond to diffraction by the (111) and ($\bar{1}11$) planes and also by the (220) planes [12]. The correspondence of the observed transmission spectra to the diagram of optical modes of opal is the subject of a separate investigation [10]. The dependence of $\hbar\omega_0$ of the opal PBG on the observation angle in the transmission spectra is described well within the Bragg approximation. The transmission spectrum at $\theta = 0°$ exhibits a well-defined minimum with $\hbar\omega_{01} = 1.39$ eV (Fig. 2c), which corresponds to the diffraction resonance by the (111) planes of the fcc opal lattice or to a weighted superposition of gaps between the first and fourth bands and the second and third bands, and also a sharp decrease at $\hbar\omega > 2.2$ eV. As the detection angle increases, the (111) minimum shifts toward high frequencies. Starting at angle $\theta \geq 20°$, a minimum arises from diffraction by the ($\bar{1}11$) planes at the frequency $\hbar\omega_{02}$, though the photonic gap in this direction is not opened. The departure from the Bragg model appears because of two-plane diffraction in the region of angles of incidence from 40° to 50°; with regard to the refraction of light in opal, this corresponds to the ΓK direction of the Brillouin zone. One more minimum appears in the transmission spectrum starting at $\theta = 35°$, near $\hbar\omega_{03} = 2.3$ eV, and remains virtually at the same frequency as the angle increases. This minimum may be assigned to the attenuation of transmission between the seventh and eighth opal modes [13].

Let us compare the FS and BS spectra of type 3 samples. The intensity of the FS light decreases for the directions and frequencies determined by the PBG (Fig. 2c). The intensity of the BS light increases in two bands. One of them is located near the low-frequency PBG edge along the direction of light incidence and is independent of the angle α, and the other shifts toward high frequencies as the angle α increases (Fig. 3a). The latter band of the BS spectrum is complementary to the dispersion minimum of the FS spectrum (Fig. 3b), whereas the former is shifted by 0.091 eV with respect to the nondirectional minimum in the FS spectrum.
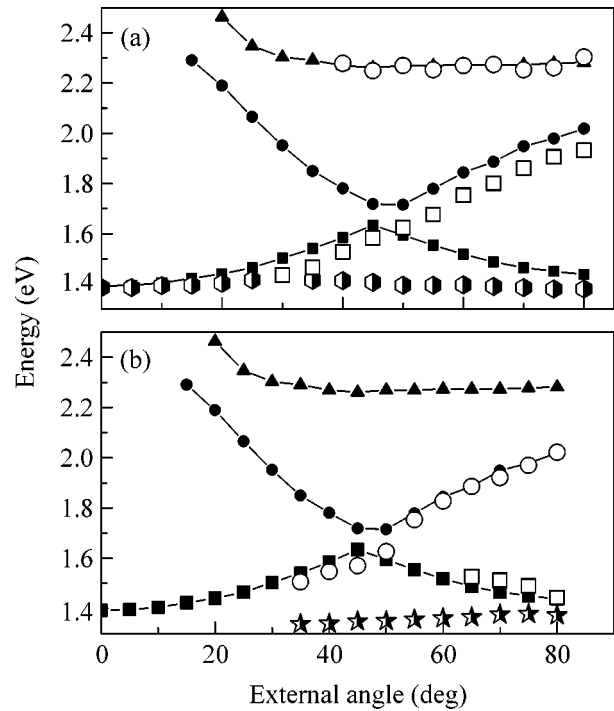
The angular dispersion of the features in the FS and BS spectra is shown in Fig. 4 in comparison with the dispersion of the minima in the transmission spectrum. The dispersion band in the FS spectrum complies well with the Bragg model, though its shift with respect to the corresponding minimum of the transmission spectrum is clearly defined. The most pronounced difference between the FS spectra and the transmission spectra is the absence of the minimum from diffraction by the ($\bar{1}11$) planes. It is unclear so far whether this distinction is of a fundamental nature or is associated with an insufficient resolution of the scattering spectra. The BS spectra exhibit a band due to the (111) PBG. Part of the branch from the ($\bar{1}11$) PBG can also be constructed, though the corresponding bands are very weak (Fig. 2c). It is interesting to note that no systematic shift of the BS band from the position of the (111) PBG is observed. There are bands in the FS and BS spectra that weakly depend on the observation angle (Fig. 4a). Both these bands correspond to light scattering along the direction of incidence; however, the dispersions of these bands are different.

Apparently, the main mechanism of the light scattering detected behind the opal film is the scattering by defects, whereas the losses at the air–opal interface are rather manifested in the back scattering. The minima in the FS light spectrum correspond to the decrease in the losses of the forward-scattered light by virtue of the effect of the opal PBG. The decrease in the forward scattering at the minimum corresponding to the PBG along the direction of light incidence is a consequence of the diffraction reflection in the [111] direction. Its central frequency is firmly fixed by the angle of light incidence. Similarly, the decrease in the intensity of the FS light at the frequencies of the (111) PBG along the
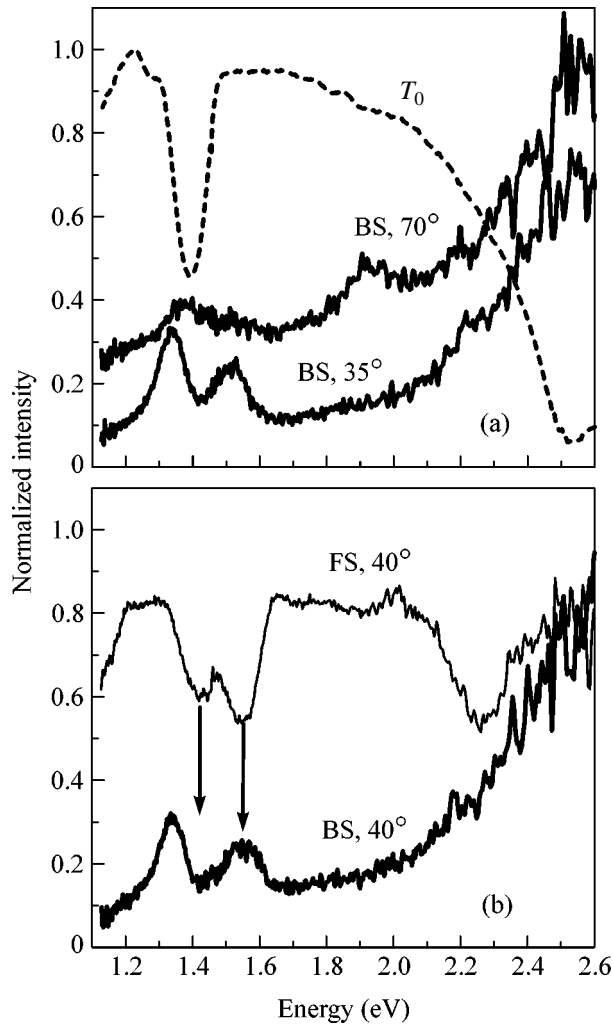
Fig. 3. (a) Back-scattering (BS) spectra at $\alpha = 35°$ and $70°$ (thickened lines, curves are shifted along the ordinate axis) in comparison with the transmission spectrum at $\theta = 0°$ (dashed curve). (b) BS and FS spectra at $\theta = 0°$ and $\alpha = 40°$.
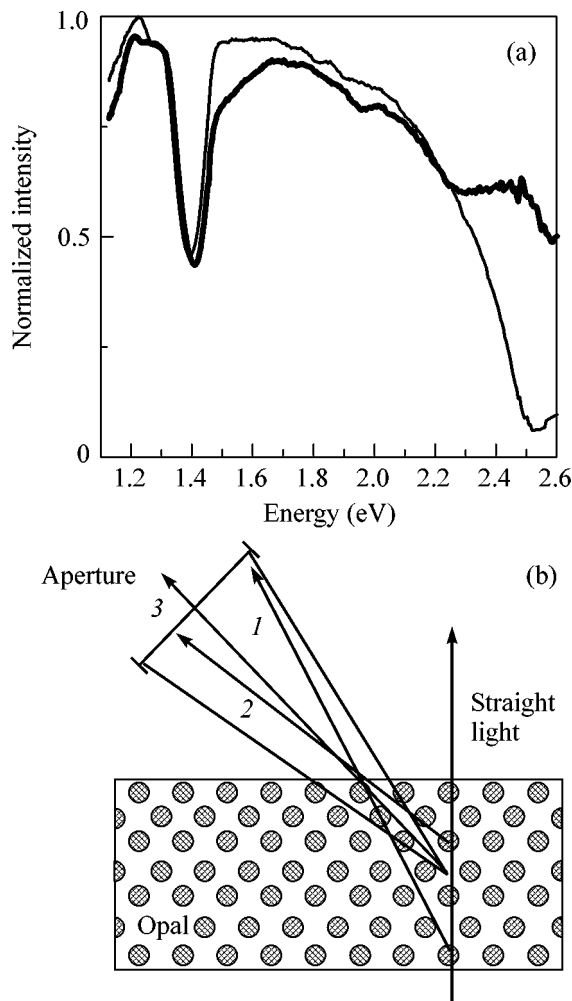

Fig. 4. (a) Angular dispersion of minima in the transmission spectrum (black symbols in panels (a) and (b)): squares are the PBG between the second and third bands, circles are the PBG between the fifth and sixth bands, and triangles are the PBG between the seventh and eighth bands. Minima in the PS spectrum (light symbols): squares are due to diffraction by the (111) planes, and circles are due to diffraction by the (220) planes. (b) Maxima in the BS spectrum (light symbols): circles are due to diffraction by the (111) planes, and squares are due to diffraction by the ($\bar{1}$11) planes. Half-filled symbols in both panels correspond to nondispersion bands.

detection direction is a consequence of the decrease in the number of optical modes in the photonic gap. The necessity of the scattering act for the observation of both minima in the FS spectrum is evident from the following simple consideration: a flux propagating inside the PhC collinearly with the incident beam is necessary for the observation of a minimum along the direction of beam incidence, whereas the propagation of a secondary flux along the direction determined by the angle α is necessary for the appearance of a minimum along the detection direction. It is evident in Fig. 5a that the summation of the scattered light over all angles leads to the pulling of the high-frequency edge of the PBG minimum along the direction of light incidence and to the absence of directional minima. This behavior is in agreement with the results of the numerical simulation of scattering in a slightly disordered 2D PhC [14].

The consideration of the trajectories of photons scattered in the opal film and reaching the detector aperture shows that the red shift of the photonic-gap frequency in the FS spectrum with respect to the gap in the transmission spectrum can be explained both by the difference in the PhC band curvatures above and below the PBG frequency [14] and by purely geometrical factors. It is evident from the scheme in Fig. 5b that beams reaching the detector are scattered at different depths. Beam *1* has a smaller scattering angle than beam *2*, and, hence, the PBG in the direction of its propagation is less frequency-shifted than in the direction of beam *2*. The intensities of the scattered light add up with a weight factor taking into account the diagram of scattering directionality in directions *1* and *2*. Because the intensity varies with the angle as $I \sim 1/\alpha^{3/2}$, the conclusion can be drawn that the observed PBG position with respect to the propagation direction of beam *3*, for which the detection angle is nominally determined, should exhibit an effective red shift.

The band in the BS spectrum that depends on the detection angle is conjugated with the corresponding

Fig. 5. (a) The FS spectrum summed over all angles α (thickened line) and the transmission spectrum at $\theta = 0°$. (b) Schematic diagram explaining the red shift of the dispersion minimum in the FS spectra.

the PBG, and the scattering significantly increases at the PBG edge because of the localization of optical modes. Of the two back-scattering enhancement mechanisms, namely, weak localization due to the interference of scattered photons [15] and strong localization at the PBG edge [16], preference should be given to the latter. The reason is that weak localization is independent of the frequency and is observed in a limited range of scattering angles with respect to the normal to the surface because of a sharp decrease in the interference contribution as the optical path length increases. It should be noted that, first, the nondispersion FS minimum is shifted with respect to the angle-independent BS maximum and, second, these features are the manifestations of different processes of light propagation in the PhC.

In conclusion, it should be emphasized that studying the light scattering in a PhC is of both practical and fundamental interest, because this phenomenon is related to both optimization of light losses in various optical devices and investigation of light propagation in PhCs. In this work, the structure of spectra of light scattered in 3D opal PhCs has been discussed and classified. It is shown that diffractions associated with the observation angle decrease losses due to forward scattering, which is compensated by an increase in the intensity of the back-scattered flux. On the contrary, the angle-independent features of the loss spectra are not complementary to each other. The angle-independent minimum in the FS spectrum corresponds to the decrease in the intensity of light penetrating into the PhC in the range of PGB frequencies in the direction of the incident beam because of its diffraction reflection. The nondispersion band in the BS spectrum is a result of a decrease in the rate of light flux transfer toward the PBG edge. It has not been possible so far to separate the contributions to the decrease in forward scattering that come from the localization at the photonic-gap edge and from the diffraction because of the frequency intervals in which these mechanisms are operative overlap.

band in the FS spectrum; that is, it is the band of light diffraction reflection along the detection direction. In this case, the sources of light are both the losses at the air–opal interface and the scattering by near-surface defects. The position of this band is less subject to the effect of the geometry of light collection, because light propagation from the opal depth is suppressed in this direction.

The nondispersion band in the BS spectrum characterizes the losses due to the binding of the incident light with the PhC in the region of photonic-gap edge. It should be noted that the maximum of this band lies at the PBG edge along the [111] axis, because it coincides in frequency with the maximum of the first derivative of the transmission spectrum at $\theta = 0°$. It can be suggested that this BS band is caused by a change in the PhC transmission: the PhC transmission much below the PBG frequency is analogous to the transmission of a uniform medium, light is reflected by the PhC within

REFERENCES

1. P. St. J. Russel, T. A. Brick, and F. D. Llooyd-Lucas, in *Confined Electrons and Photons: New Physics and Applications*, Ed. by E. Burstein and C. Weisbuch (Plenum, New York, 1995), p. 585–633.
2. Y. Xia, B. Gates, and Y. Yin, Adv. Mater. **12**, 693 (2000).
3. Yu. A. Vlasov, V. N. Astratov, A. V. Baryshev, *et al.*, Phys. Rev. E **61**, 5784 (2000).
4. A. F. Koenderink and W. L. Vos, Phys. Rev. Lett. **91**, 213 902 (2003).
5. S. G. Romanov and C. M. Sotomayor Torres, Phys. Rev. E (in press).
6. V. N. Astratov, A. M. Adawi, S. Fricker, *et al.*, Phys. Rev. B **66**, 165 215 (2002).

7. Y. A. Vlasov, M. A. Kalitieevski, and V. V. Nikolaev, Phys. Rev. B **60**, 1555 (1999).

8. J. Huang, N. Eradat, M. E. Raikh, *et al.*, Phys. Rev. Lett. **86**, 4815 (2001).

9. J. F. Galisteo-Lopez, E. Palacios-Lidon, E. Castillo-Martinez, *et al.*, Phys. Rev. B **68**, 115 109 (2003).

10. S. G. Romanov, D. N. Chigrin, and C. M. Sotomayor Torres (in preparation).

11. A. Reynolds, F. Lo'pez-Tejeira, D. Cassagne, *et al.*, Phys. Rev. B **60**, 11 422 (1999).

12. R. C. Schroden, M. Al-Daous, C. F. Blanford, *et al.*, Chem. Mater. **14**, 3305 (2002).

13. H. Miguez, V. Kitaev, and G. A. Ozin, Appl. Phys. Lett. **84**, 1239 (2004).

14. M. A. Kalitieevski, J. Manzanares-Martinez, D. Cassagne, *et al.*, Phys. Rev. B **66**, 113 101 (2002).

15. P. van Albada and A. Lagendijk, Phys. Rev. Lett. **55**, 2692 (1985).

16. S. John, Phys. Rev. Lett. **58**, 2486 (1987).

Translated by A. Bagatur'yants

Magnetic Hysteresis in the Generalized Mean-Field Model for Ising System

E. Z. Meĭlikhov

Russian Research Centre Kurchatov Institute, pl. Kurchatova 1, Moscow, 123182 Russia
e-mail: meilikhov@imp.kiae.ru
Received April 19, 2004

Magnetic hysteresis and demagnetization of a simple cubic lattice of Ising spins is studied in the framework of the generalized mean-field approximation taking into account spatial fluctuations of the local magnetic field. The existence of a dynamic phase transition is demonstrated. © *2004 MAIK "Nauka/Interperiodica"*.

PACS numbers: 75.10.Hk; 75.60.Ej

Magnetic hysteresis is, on the one hand, an example of a dynamic nonequilibrium process having important practical applications in various magnetic devices and, on the other hand, the general property of physical systems of a definite type. One such system (uniaxial ferromagnet) can be described by the Ising model, which was studied both numerically and analytically by many authors. However, in most publications in this field, the stationary properties of the model were studied, while the nonequilibrium effects associated with the transitions of the magnetic system between two equivalent states differing in the direction of the magnetic moment have been studied insufficiently. Such dynamic effects in the Ising model were studied both in the mean-field approximation [1, 2] and by the Monte Carlo simulation [3–6]. For a ferromagnetic system in a varying magnetic field $H_e(t) = H_0\sin\omega t$, the dynamic order parameter is the magnetization $j(t)$ averaged over a period of field variation,

$$\bar{j} = \frac{\omega}{2\pi}\oint j(t)dt. \tag{1}$$

It was shown [2] that the system undergoes a dynamic phase transition, with the transition curve separating (in the H_0, T coordinates) phases with $\bar{j} \neq 0$ (in the region of small values of H_0 and T) and phases with $\bar{j} = 0$ (in the region of large values of H_0, T). This is shown schematically in the inset in Fig. 1. According to some indications, this transition is a true thermodynamic transition, because it is accompanied by the characteristic features in the susceptibility and specific heat [6]. Many authors claim that this transition curve contains a tricritical point separating the curve into two segments, namely, a high-temperature segment, in which the transition is smooth, and a low-temperature segment, in which the transition occurs jumpwise [4, 7]. However, it was stated in a recent publication by Korniss *et al.* [8] that the dynamic phase transition cannot be a first-order

transition and that all previous conclusions drawn on the basis of the Monte Carlo method are the results of the analysis of finite-size systems.

Since an exact solution does not exist even for a steady-state 3D Ising system (not only in a magnetic field but also without it), the mean-field theory is the main analytic method for studying such a system. It was in the framework of this theory that the dynamic properties of Ising systems were studied. This work is aimed at the analysis of such properties within the framework of the generalized mean-field model taking into account spatial fluctuations of the effective local magnetic field.
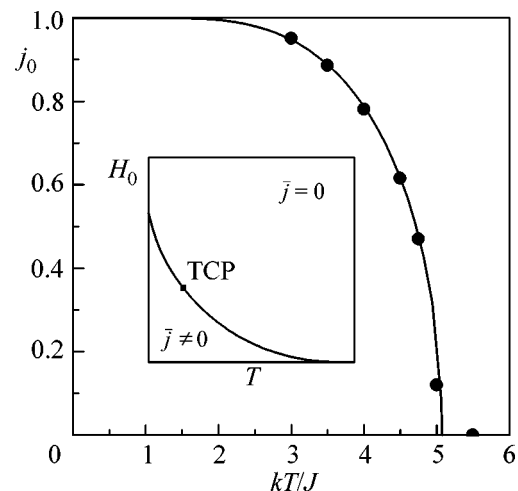
Fig. 1. Temperature dependence of the magnetization of a simple cubic lattice of Ising spins interacting with nearest neighbors (the result obtained in the generalized mean-field theory). Circles correspond to the magnetization of the system subjected to demagnetization. The inset shows schematically the dynamic phase-transition curve; TCP marks a hypothetical tricritical point.

Let us consider a system of magnetic moments μ in the form of a 3D lattice of Ising spins; we will describe this system by its spin variables $s_j = \pm1$, $j = 1, 2, \ldots$. At a finite temperature T, thermal fluctuations lead to spin flip from state $+1$ to state -1 and back. The probabilities of such transitions determine the relaxation equation for one of the parameters of the system. For example, the probability $P(s_1, s_2, \ldots, +s_j, \ldots, s_N; t)$ of realizing a certain spin configuration at time t is defined by the equation [1]

$$\frac{d}{dt}P(s_1, s_2, \ldots, +s_j, \ldots, s_N; t)$$

$$= -\sum_j w_j(s_j)P(s_1, s_2, \ldots, +s_j, \ldots, s_N; t) \qquad (2)$$

$$+ \sum_j w_j(-s_j)P(s_1, s_2, \ldots, -s_j, \ldots, s_N; t),$$

where $w_j(s_j)$ and $w_j(-s_j)$ are the probabilities of the jth spin flip from state $+1$ and -1, respectively. In accordance with the detailed balancing principle, we have

$$w_j(s_j)P_0(s_1, s_2, \ldots, +s_j, \ldots, s_N)$$
$$= w_j(-s_j)P_0(s_1, s_2, \ldots, -s_j, \ldots, s_N), \qquad (3)$$

where the probabilities $P_0(s_1, \ldots)$ correspond to a thermodynamically equilibrium configuration. These probabilities are related by the Boltzmann relationship

$$\frac{P_0(s_1, s_2, \ldots, -s_j, \ldots, s_N)}{P_0(s_1, s_2, \ldots, +s_j, \ldots, s_N)} = \exp\left(-\frac{\Delta_j E}{kT}\right), \qquad (4)$$

where $\Delta_j E$ is the energy difference between the states differing only in the direction of the jth spin. Obviously, $\Delta_j E = 2E_j$, where the energy of the jth spin in state $s_j = +1$

$$E_j = \mu H_e + \sum_{k \neq j} s_k J_{jk} \qquad (5)$$

is determined by its interaction with the external magnetic field H_e and the remaining spins, and J_{jk} is the energy of interaction with the kth spin. Equations (3)–(5) imply that

$$\frac{w_j(s_j)}{w_j(-s_j)} = \frac{1 - s_j\tanh(E_j/kT)}{1 + s_j\tanh(E_j/kT)}. \qquad (6)$$

Using Glauber's receipt [9], we can write the individual probabilities $w_j(s_j)$ and $w_j(-s_j)$ satisfying relation (6) in the form

$$w_j(s_j) = \frac{1}{2}\Omega[1 - s_j\tanh(E_j/kT)],$$
$$\qquad (7)$$
$$w_j(-s_j) = \frac{1}{2}\Omega[1 + s_j\tanh(E_j/kT)],$$

where Ω is a parameter having the meaning of the frequency with which spin tries to change its orientation.

Generally speaking, this frequency depends on the temperature and configuration of all spins in the system, though it is usually assumed to be constant. With such a choice, the equilibrium state of the system coincides with the state following from the mean-field equation (see below).

The average (over configurations) value of the jth spin at time t is given by

$$\langle s_j \rangle = \sum_{(s)} s_j P(s_1, \ldots, s_N; t), \qquad (8)$$

where summation is over all spin configurations. Substituting Eq. (2) into Eq. (8) and using relations (7), we obtain [1]

$$\frac{d}{dt}\langle s_j \rangle = -\Omega[\langle s_j \rangle - \langle \tanh(E_j/kT) \rangle]. \qquad (9)$$

This equation could be simplified in the spirit of the mean-field theory by substituting $\langle \tanh(E_j/kT) \rangle \longrightarrow \tanh(\langle E_j \rangle/kT)$, where $\langle E_j \rangle = \mu H_e + \sum_{k \neq j} J_{jk}\langle s_k \rangle$ and taking into account that the relative magnetization j of the system is proportional to $\langle s_j \rangle$. This would lead to the equation

$$\frac{dj}{dt} = -\Omega\left[j - \tanh\left(\frac{\mu H_e + j\sum J_{jk}}{kT}\right)\right], \qquad (10)$$

which describes the magnetization relaxation to a thermodynamically equilibrium state defined by the standard mean-field equation $j = \tanh[(\mu H_e + j\sum J_{jk})/kT]$. The approximate nature of this equation follows if only from analysis of the results of its application to the situation where the external field is absent ($H_e = 0$) and only the interaction with the nearest neighbors is significant; we denote the energy of this interaction by J. In this case, $\sum J_{jk} = zJ$, where z is the number of nearest neighbors. The critical temperature predicted by the mean-field equation in this case is equal to $kT_C = zJ$; for a simple cubic lattice, this gives $kT_C = 6J$. However, a practically exact result [10] is $kT_C = 4.51J$.

For this reason, we will simplify Eq. (9) using a different procedure that is a generalization of the mean-field model. We introduce the effective molecular field H_3 acting on the chosen spin from the remaining spins:

$$H_3 \equiv \frac{1}{\mu}\sum_{k \neq j} s_k J_{jk}. \qquad (11)$$

For different spins, this field is different and can be described by the distribution function $F(j, H_3)$ depend-

Configurations of the magnetic moments of nearest neighbors in a simple cubic lattice and their probabilities

Effective magnetic field, $\mu H_3/J$	Number of possible configurations	Configuration probability in a system with magnetization j
6 (+++++)	$C_6^0 = 1$	$(1/64)(1+j)^6$
4 (++++−)	$C_6^1 = 6$	$(6/64)(1+j)^5(1-j)$
2 (++++−−)	$C_6^2 = 15$	$(15/64)(1+j)^4(1-j)^2$
0 (+++−−−)	$C_6^3 = 20$	$(20/64)(1+j)^3(1-j)^3$
−2 (++−−−−)	$C_6^4 = 15$	$(15/64)(1+j)^2(1-j)^4$
−4 (+−−−−−)	$C_6^5 = 6$	$(6/64)(1+j)(1-j)^5$
−6 (−−−−−−)	$C_6^6 = 1$	$(1/64)(1-j)^6$

ing on the system magnetization. Then, Eq. (9) can be written in the form

$$\frac{dj}{dt} = -\Omega\left\{j - \int_{-\infty}^{\infty} \tanh\left[\frac{\mu(H_e + H_3)}{kT}\right]F(j, H_3)dH_3\right\}, \tag{12}$$

and the problem can be reduced to the determination of the function $F(j, H_3)$. Unfortunately, exact calculation of this function requires the inclusion of spin correlations [11], but the appropriate method is currently unknown. However, we can derive an approximate expression for this function; to find out the extent to which the result obtained in the mean-field theory is improved in this case, we calculate the corresponding value of the critical temperature and compare it with the exact value mentioned above. For this purpose, we consider a simple cubic lattice of Ising spins with the interaction between nearest neighbors.

The interaction energy of the jth spin with its nearest neighbors in a simple cubic lattice is the algebraic sum of six terms with the same absolute value J; the sign of these terms is determined by the relative orientation of the spin in question and the neighboring spins. The number of corresponding configurations is $2^6 = 64$. Their distribution in the effective magnetic field H_3 and the probabilities of these configurations in a system with magnetization j are given in the table.

The corresponding distribution function has the form

$$F(j; H_3) = \frac{1}{64}[(1+j)^6\delta(6h_J) + 6(1+j)^5(1-j)\delta(4h_J)$$

$$+ 15(1+j)^4(1-j)^2\delta(2h_J) + 20(1+j)^3(1-j)^3\delta(0)$$

$$+ 15(1+j)^2(1-j)^4\delta(-2h_J) \tag{13}$$

$$+ 6(1+j)(1-j)^5\delta(-4h_J) + (1-j)^6\delta(-6h_J)],$$

where $h_J \equiv J/\mu$. Substituting this function into Eq. (12), we obtain the equation describing the time evolution of the system magnetization:

$$\frac{dj}{d(\Omega t)} = j - \frac{1}{64}\{(1+j)^6\tanh[(h_e + 6h_J)/\theta]$$

$$+ 6(1+j)^5(1-j)\tanh[(h_e + 4h_J)/\theta]$$

$$+ 15(1+j)^4(1-j)^2\tanh[(h_e + 2h_J)/\theta]$$

$$+ 20(1+j)^3(1-j)^3\tanh[h_e/\theta] \tag{14}$$

$$+ 15(1+j)^2(1-j)^4\tanh[(h_e - 2h_J)/\theta]$$

$$+ 6(1+j)(1-j)^5\tanh[(h_e - 4h_J)/\theta]$$

$$+ (1-j)^6\tanh[(h_e - 6h_J)/\theta]\},$$

where $h_e \equiv \mu H_e(t)/J$ and $\theta \equiv kT/J$ are the reduced values of the external varying field and temperature, respectively.

First of all, let us find the Curie temperature obtained in the given approximation for our system for $H_e = 0$. To do this, it is sufficient to equate the right-hand side of Eq. (14) to zero, which gives

$$j_0^2 = \frac{A - [A^2 - 36B_-(B_+ - 16/3)]^{1/2}}{6B_-}, \tag{15}$$

where

$$A = 10[3\tanh(2/\theta) - \tanh(6/\theta)] > 0,$$
$$B_\pm = 5\tanh(2/\theta) \pm \tanh(4/\theta) + \tanh(6/\theta) > 0. \tag{16}$$

The Curie temperature is determined by the condition $B_+ - 16/3 = 0$; by solving the corresponding equation, we obtain $\theta_C = kT_C/J = 5.08$, which is much closer to the exact result than the mean-field value. Equation (15) also defines the temperature dependence $j_0(T)$ of the equilibrium magnetization of the system, as shown in Fig. 1.

Let us now consider magnetic relaxation effects in the given system of spins. The traditional (most often considered) phenomenon among these effects is hysteresis; in addition, we will also consider the process of demagnetization from the saturated state. Both these phenomena are described by the dependence $j(H_e)$ of the system magnetization on the varying magnetic field $H_e(t)$. When hysteresis is analyzed theoretically, the time dependence of the field is usually chosen [3] in the form of a constant-amplitude sinusoid: $H_e(t) = H_0\sin\omega t$. On the other hand, experiments are usually carried out with a linear sweep of the field. For this reason, we sought the solution of relaxation Eq. (14) for a magnetic field varying in time according to a saw-tooth dependence with a gradually decreasing tooth height (inset in Fig. 2). The period of oscillations decreased synchronously with the field amplitude, and the total
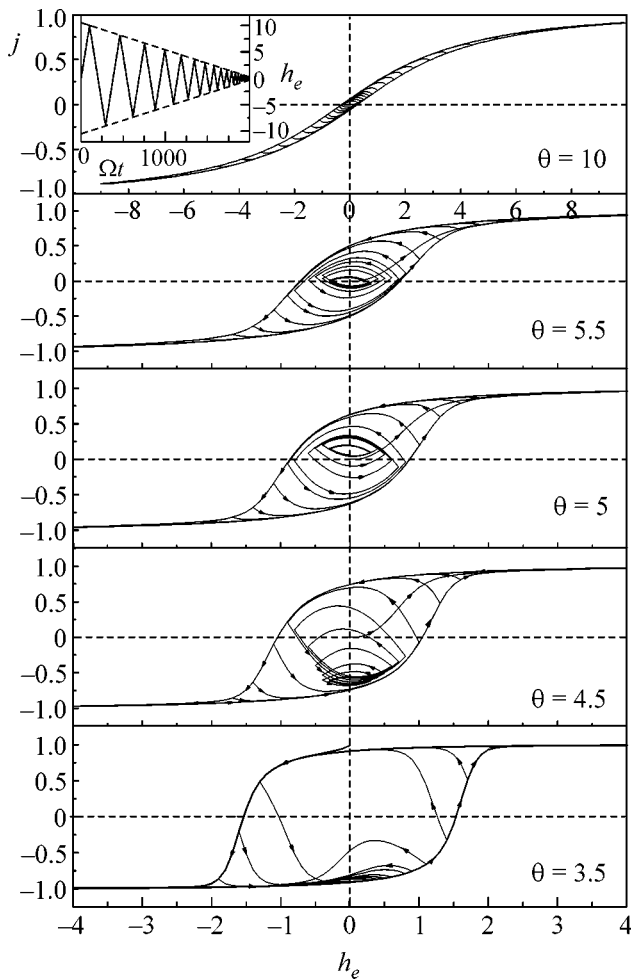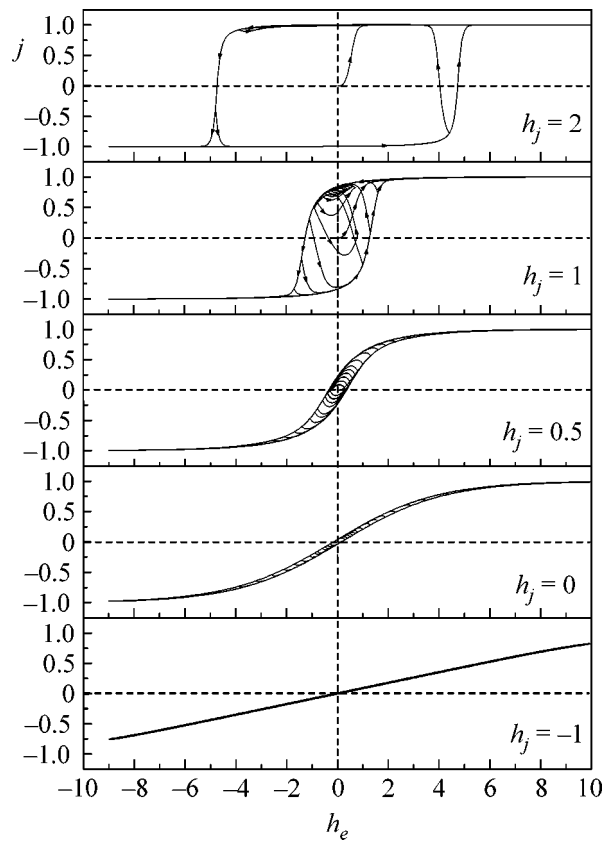
Fig. 2. Field dependences $j(h_e)$ of the system magnetization with the spin–spin interaction energy $h_J = +1$ at various temperatures. The final value of magnetization is determined by the temperature: it is finite at $\theta < \theta_C$ and is zero at $\theta > \theta_C$. The inset shows the time dependence of the magnetic field.


Fig. 3. Field dependences $j(h_e)$ of the magnetizations of the systems with different spin–spin interaction energies h_J at temperature $\theta = 4$ corresponding to the Curie temperature for a system with $h_J \approx 0.8$.

time of the process was $2000/\Omega$. Thus, in the course of unified calculation, we obtained the hysteresis loop and, at the same time, determined the state to which the system passed as a result of demagnetization. The results of such calculations are presented in Figs. 2 and 3. The former shows the evolution of magnetization/demagnetization of the system at various temperatures, while the latter illustrates the effect of spin-interaction energy characterized by the effective field $h_J = J/\mu$ on this process.

It can be seen from Fig. 2 that the area of the hysteresis loop monotonically decreases with increasing temperature. The process of demagnetization pushes the system into a state with a magnetization whose absolute value always coincides with the thermodynamically equilibrium (at a given temperature) magnetization j_0 defined by Eq. (15). As for the sign (i.e., direction) of the final magnetization, it depends on the details of the

demagnetization process itself and can be either positive or negative.

Similarly, Fig. 3 demonstrates that the hysteresis loop increases with the energy of spin–spin ferromagnetic interaction and is absent for the antiferromagnetic interaction (lower panel in Fig. 3).

The field dependences of the magnetization shown in Figs. 2 and 3 clearly demonstrate the existence of dynamic phase transition. The latter is manifested in a sharp variation of the average (over a period of field oscillations) magnetization of the system $\bar{j} \equiv (\omega/2\pi)\oint j\,dt$ from zero to a finite value, when the field amplitude becomes smaller than a certain critical value h_{e0} (depending on the temperature and oscillation frequency). This is a general property of stochastic dynamic systems with fluctuations of the type of kinetic Ising model [5, 6]; at present, such systems can be investigated only using Monte Carlo simulation. In this case, the transition is manifested in the solution of the mean-field generalized relaxation equation. It is illustrated by the dependences of the average magnetization $\bar{j}$ of the system on the cycle number in the demagnetization process shown in Fig. 4. At a high temperature
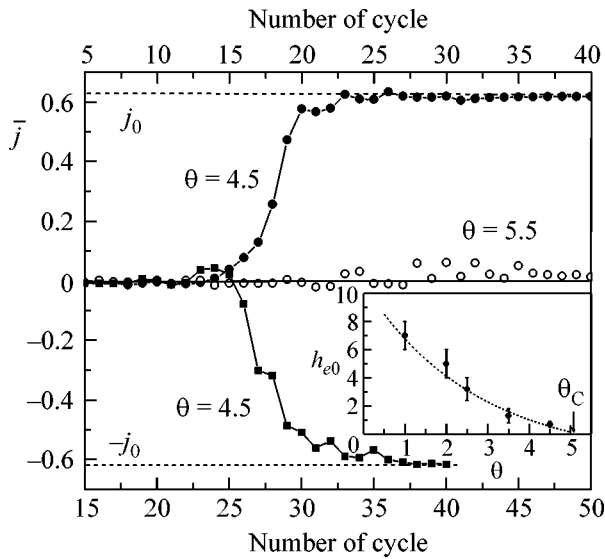
Fig. 4. Dependence of the average magnetization $\bar{j}$ of a system with $h_J = 1$ on the number of the cycle in the process of demagnetization from the saturated state. The two curves for the ferromagnetic state ($\theta = 4.5$) correspond to the processes with differing (by 30%) periods of field variation. The inset shows the dynamic phase-transition curve of the system.

($\theta = 5.5 > \theta_C = 5.08$ for $h_J = 1$), when the ground state of the system is paramagnetic, the hysteresis loops are symmetric and the average magnetization is close to zero (the latter differs from zero only due to the finite rate of the decrease in the amplitude of saw-tooth-field variation, which amounts to 5% per oscillation half-period in our calculations). On the contrary, at a low temperature ($\theta = 4.5 < \theta_C$), the ground state of the system is ferromagnetic and spontaneous symmetry breaking takes place (Fig. 4). The system falls into one of the two possible states with opposite signs of magnetization, characterized by an equilibrium magnetization $\pm j_0$.

This occurs when the field amplitude achieves the critical value h_{e0}. The temperature dependence $h_{e0}(\theta)$ is precisely the factor that determines the dynamic phase-transition curve. The inset in Fig. 4 shows the shape of this line for a system with $h_J = 1$.

The next step may be analysis of the behavior of the system placed in a varying magnetic field with a small random component. In this way, the role of fluctuations can be simulated.

REFERENCES

1. M. Suzuki and R. Kubo, J. Phys. Soc. Jpn. **24**, 51 (1968).
2. T. Tomé and M. J. de Oliveira, Phys. Rev. A **41**, 4251 (1990).
3. M. Rao, H. R. Krishnamurty, and R. Pandit, Phys. Rev. B **42**, 856 (1990).
4. M. Acharyya and B. K. Chakrabarti, Phys. Rev. B **52**, 6550 (1995).
5. W. S. Lo and R. A. Pelcovitz, Phys. Rev. A **42**, 7471 (1990).
6. M. Acharyya, Phys. Rev. E **56**, 1234 (1997).
7. M. Acharyya, Phys. Rev. E **59**, 218 (1999).
8. G. Korniss, P. A. Rikvold, and M. A. Novotny, Phys. Rev. E **66**, 056127 (2002).
9. R. J. Glauber, J. Math. Phys. **4**, 294 (1963).
10. T. L. Hill, *Statistical Mechanics: Principles and Selected Applications* (McGraw-Hill, New York, 1956; Inostrannaya Literatura, Moscow, 1960).
11. M. Thomsen, M. F. Thorpe, T. C. Choy, and D. Sherrington, Phys. Rev. B **30**, 250 (1984); T. C. Choy, D. Sherrington, M. Thomsen, and M. F. Thorpe, Phys. Rev. B **31**, 7355 (1985); M. Thomsen, M. F. Thorpe, T. C. Choy, and D. Sherrington, Phys. Rev. B **33**, 1931 (1986).

Translated by N. Wadhwa

Nonzeroth-Order Anomalous Optical Transparency in Modulated Metal Films Owing to Excitation of Surface Plasmon Polaritons: An Analytic Approach[¶]

A. V. Kats and A. Yu. Nikitin

Usikov Institute for Radiophysics and Electronics, National Academy of Sciences of Ukraine, Kharkov, 61085 Ukraine
e-mail: avkats@akfirst.kharkiv.com, avkats@online.kharkov.ua
Received April 19, 2004; in final form, May 6, 2004

The problem of anomalous light tunneling through periodically modulated metal films is examined in a purely analytical approach. The approach uses large magnitude of the dielectric permittivity of metals in the visible and near-infrared (it is equivalent to that resulting in the Leontovich boundary conditions for semi-infinite problems). It is shown that the anomalous transparency recently discovered experimentally is caused by the excitation of single- or double-boundary surface plasmon polaritons due to film modulation. Dependences of the resonance transparency on parameters of the problem are analyzed in detail, and the optimum parameters (optimal layer thickness and optimal modulation amplitude) corresponding to extreme values of the transmittance of both zero and nonzero diffraction orders have been found. Classifying the possible types of resonances has allowed the identification of special and nontrivial features of the effect. In particular, we predict strong nonzeroth-order anomalous transparency. © 2004 MAIK "Nauka/Interperiodica".

PACS numbers: 42.25.Bs; 73.20.Mf; 78.20.-e

Despite the great amount of papers on the photon–SPP (surface plasmon polariton) transformations in periodical structures that appeared over the past decades (it is sufficient to mention [1–3]), the experiment concerning transparency of metal films [4] which is caused by the effect was realized only recently. Since this first observation of the extraordinary optical transmission through subwavelength hole arrays, many theoreticians have contributed to explaining the effect [5–11]. But still the qualitative analytical picture of the light tunneling phenomenon is not sufficiently covered. The majority of the explanations are based upon numerical calculations (to the best of the author's knowledge, the only exceptions are [5, 9], but paper [5] contains only crude quantitative estimates, while paper [9] deals with the case of a strictly normal incidence onto the harmonically modulated film; moreover, the second spatial field harmonic was not taken into account in the latter paper, which prevented finding the true position of the resonance). Numerical approaches do not make it possible to obtain a deep intuitive insight into the problem.

While the principal channel for anomalous light transmittance for normal incidence and nonsymmetrical dielectric surrounding is in a nonspecular direction, most papers on the subject examined the zeroth-order transmittance and reflectivity alone (an exception is the recent paper [12]). The nonzeroth-order transmittance

can exceed the zeroth-order value of a few tens that of zeroth-order. This means that the process of light tunneling in the case of "single-boundary-localized" (SB) excitation (when an SPP is localized at one face of the metal film only) can be to no lesser a degree effective than under the "double-boundary-localized" (DB) excitation (with SPP localized at both sides of the film; see the experiment of [13]).

This letter suggests a thorough new analytical examination of the effect. We will discuss both specular and nonspecular transmittance. General results are obtained for both oblique and normal incidence. Simple estimates are given for 2D periodic structures, and it is shown that they are similar to those for 1D gratings, contrary to conclusions of some writers (see [10, 14]). Our approach also makes it clear that the main resonance effects depend on the existence of the periodicity itself, being rather insensitive to the specific type of modulation (modulation of the dielectric permittivity [5, 9] or dielectric pillars [6, 12], cylindrical [11] or square [10] holes, relief corrugations [7]). However, the type of modulation can influence polarization properties of the periodically modulated film, as will be shown in a future paper.

Let a *p* (*TM*)-polarized monochromatic wave (time dependence of the form exp($-i\omega t$) is omitted) of magnetic field amplitude H^i be incident onto a metal film surrounded by dielectric media with permittivities ε_σ, $\sigma = \pm$, from the medium with ε_-. Let the dielectric per-

---

[¶]This article was submitted by the authors in English.
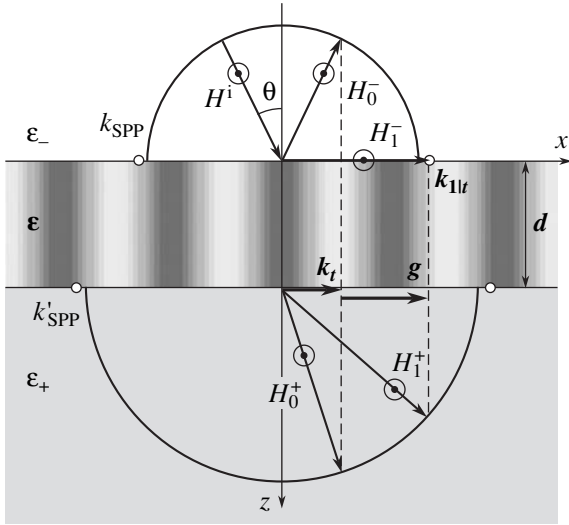
Fig. 1. Geometry of the problem. Nonsymmetric dielectric surrounding of a metal film. A single SB metal–superstrate first-order resonance, $k_{1x} \simeq K^-$, is shown. The circles $\odot$ show that the magnetic field is guided along the y axis.

mittivity of the film be periodically modulated along the x direction, $\varepsilon(x) = \varepsilon(x + \Lambda)$, and the plane of incidence coincide with the xz plane (see Fig. 1). Owing to the symmetry, only the y component of the magnetic field is nonzero. Seeking the solution in the form of a Fourier–Floquet expansion and taking into account the radiation conditions, we obtain, in the dielectric media,

$$H^\sigma(x, z) = \delta_{\sigma, -} H^i \exp(ik_{-|z} z + ik_x x)$$
$$+ \sum_n H_n^\sigma \exp[ik_{\sigma|nz}(z - \delta_{\sigma, +} d) + ik_{nx} x)],$$

$$k_{nx} = k_x + ng, \quad k_{\sigma|nz} = \sigma\sqrt{\varepsilon_\sigma k^2 - k_{nx}^2}, \quad g = 2\pi/\Lambda,$$

$$\text{Re, Im}\{\sqrt{\varepsilon_\sigma k^2 - k_{nx}^2}\} \geq 0, \quad \sigma = \pm,$$

where d is the film thickness and $H^\sigma(x, z)$ denote field strengths in the media with the dielectric permittivity ε_σ, i.e., for $z \geq d$ ($z \leq 0$) if $\sigma = +$ ($\sigma = -$), respectively.

The solution in the film can be represented as

$$H(x, z) = H^i \sum_{n, \sigma} h_n^\sigma(z) \exp[ik_{nx} x + \sigma\tilde{k}z],$$

where $\tilde{k} = k\sqrt{-\varepsilon_0}$, $\text{Re}\,\tilde{k} \geq 0$, and ε_0 denotes some mean value of $\varepsilon(x)$ with $\text{Re}\,\varepsilon_0 < 0$. For simplicity, we will neglect the dependence upon z of the transformation coefficients (TCs) $h_n^\sigma(z)$ here and below. This approximation is equivalent to the one resulting in the impedance (Leontovich) boundary conditions for semi-infinite problems (cf. [15]) and takes account of the large

dielectric permittivity, $|\varepsilon(x)| \gg 1$, along with the assumption of a small modulation,[1] $|\varepsilon(x) - \varepsilon_0| \ll |\varepsilon_0|$. In addition, we neglect the impact of bulk modulation on the diffraction; that is, the permittivity modulation is taken into account in the boundary conditions only. An analogous model was first applied in [17] to explain the Wood anomalies.

Using continuity of the electric and magnetic field tangential components, we can express the TCs outside the metal, $R_m \equiv H_m^-/H^i$ and $T_m \equiv H_m^+/H^i$, in terms of the inner TCs, h_m^σ,

$$R_m = -\delta_{n, 0} + \sum_\sigma h_m^\sigma, \quad T_m = \sum_\sigma h_m^\sigma \exp(\sigma\Phi), \quad (1)$$

to obtain the following infinite set of linear equations (cf. [18]):

$$\sum_{m, \sigma' = \pm} D_{nm}^{\sigma\sigma'} h_m^{\sigma'} = V_n^\sigma, \quad \sigma = \pm,$$

$$D_{nm}^{\sigma\sigma'} = [(\beta_{\sigma|n} + \sigma'\sigma\xi_0)\delta_{n, m} + \sigma\sigma'\tilde{\xi}_{n-m}]$$

$$\times [\delta_{\sigma, -} + \delta_{\sigma, +} \exp(\sigma'\Phi)], \quad V_n^\sigma = 2\beta_{-|0}\delta_{n, 0}\delta_{\sigma, -},$$

$$\beta_{\sigma|n} = \sigma k_{\sigma|nz}/k\varepsilon_\sigma, \quad \Phi = \tilde{k}d,$$

$$\xi(x) \equiv 1/\sqrt{\varepsilon(x)} = \xi_0 + \sum_n \tilde{\xi}_n \exp(ingx), \quad \tilde{\xi}_0 = 0.$$

By equating to zero the determinant of diagonal in diffraction order 2–2 submatrices of the $D_{nm}^{\sigma\sigma'}$ matrix, $\hat{D}_n = \|D_{nm}^{\sigma\sigma'}\|$,

$$|\hat{D}_n| \equiv d_n = b_{+|n}^+ b_{-|n}^+ \exp\Phi - b_{+|n}^- b_{-|n}^- \exp(-\Phi),$$

we obtain the SPP dispersion relation for the nonmodulated film. When the spatial field harmonics are far away from eigenmodes of the nonmodulated film (nonresonance conditions), the coefficients $b_{\sigma|n}^{\sigma'}$ are of the order of unity, $|b_{\sigma|n}^{\sigma'}| \simeq |\beta_{\sigma|n}| \sim 1$, whence the estimate for the determinant is $|d_n| \sim \exp\Phi'$. Under the nonresonance conditions, the matrix $D_{nm}^{\sigma\sigma'}$ is diagonal-dominated; that is, elements of the off-diagonal submatrices $D_{nm}^{\sigma\sigma'} \propto \xi_{n-m}$ for $m \neq n$ and, hence, are small as compared with that of the diagonal ones, $D_{nn}^{\sigma\sigma'}$. On the contrary, under the

---

[1] For an arbitrary film thickness, the approximation is certainly valid under the restriction $|\varepsilon(x) - \varepsilon_0| \ll \sqrt{|\varepsilon_0|}$. But, this condition, while being sufficient, seems to be far from necessary, as follows from comparison with straightforward numerical calculations (cf. [16]). Evidently, in the limit $d \longrightarrow \infty$, the validity condition is much less restrictive, $|\varepsilon(x) - \varepsilon_0| \ll |\varepsilon_0|$. Moreover, the structure of the solution obtained is completely analogous to the one for the film with a corrugated relief (see forthcoming papers).

resonance conditions, the determinant of $\hat{D}_n$ decreases by several orders of magnitude. For thick films, $\exp(-\Phi') \ll 1$, and for the determinant to decrease significantly, the condition $|b^+_{\sigma|m}| \ll 1$ or $|\beta_{\sigma|m}| \lesssim |\xi_0|$ must hold. As for the diffraction problem, $\beta_{\sigma|m}$ can possess either purely real or purely imaginary values only; the minimum of $|b^+_{\sigma|m}|$ (namely, $|b^+_{\sigma|m}|_{\min} = \xi'_0$) is achieved for $\beta_{\sigma|m} = -i\xi''_0$, which yields an SPP dispersion relation for the boundary between the metal and the dielectric half-spaces.[2] The magnitude of the determinant at this point is $|d_m| \sim \xi'_0 \exp\Phi'$. Denoting the resonance diffraction orders as r, r', etc., and the set of the resonance orders as $\mathscr{R}$, we can write the resonance condition as $\mathrm{Im}(b^+_{\sigma|r}) \simeq 0$, or, in a more explicit form,

$$\sqrt{\varepsilon_-}\sin\theta + r\kappa \simeq \tau K^\sigma, \quad \kappa \equiv g/k, \quad \tau = \pm,$$
$$K^\sigma \equiv \sqrt{\varepsilon_\sigma + \varepsilon^2_\sigma \xi''^2_0} \simeq \sqrt{\varepsilon_\sigma}, \quad \exp(-\Phi') \ll 1. \quad (2)$$

Evidently, equation with $\tau = +(-)$ corresponds to the forward (backward) direction of SPP propagation relative to the incident wave; $\sigma = -(+)$ corresponds to SPP excitation at the metal–superstrate (substrate) interface.

Analogously, the condition $|b^{\sigma'}_{\sigma|N}| \gg |\xi_0|$ defines the nonresonance subset of diffraction orders, $\mathscr{N}$, where the integers belonging to $\mathscr{N}$ are denoted as N, M, etc. Accordingly, the matrix $\hat{D}$ is decomposed into two submatrices with resonance (nonresonance) diffraction orders, $\hat{R} = \|D^{\sigma\sigma'}_{rr'}\|$ ($\hat{M} = \|D^{\sigma\sigma'}_{NN'}\|$), and two mixed matrices, $\hat{U} = \|D^{\sigma\sigma'}_{rN}\|$, and $\hat{L} = \|D^{\sigma\sigma'}_{Nr'}\|$. The corresponding right-hand sides have been denoted as $\hat{u} = \|V^\sigma_r\|$ and $\hat{v} = \|V^\sigma_N\|$. Decomposing the submatrix $\hat{M} = \|D^{\sigma\sigma'}_{NN'}\|$ into a block-diagonal and a nondiagonal matrix, we have

$$\hat{M} = \hat{A}(\hat{1} - \hat{\nu}), \quad A^{\sigma\sigma'}_{NM} = \delta_{N,M}D^{\sigma\sigma'}_{NN}, \quad \hat{\nu} = O(\tilde{\xi}),$$

where the norm of the matrix $\hat{\nu}$ is small, as its elements are proportional to the small modulation amplitude, $\hat{\nu} \sim \tilde{\xi}$. Then, $\hat{M}^{-1} = \sum^\infty_{s=0}\hat{\nu}^s\hat{A}^{-1}$. As a result, we can solve the nonresonance subsystem for $h^\sigma_N, N \in \mathscr{N}$, in an explicit form as $\|h^\sigma_N\| = \hat{M}^{-1}(\hat{v} - \hat{L}\|h^\sigma_r\|)$ and repre-

[2] For thin films, the dispersion relation changes substantially. If $\varepsilon_+ = \varepsilon_-$ and $|\Phi| \ll 1$, there are two very distinct resonance points, $\beta_r \simeq -2i\xi''_0/\Phi'$ and $\beta_r \simeq -i\xi''_0\Phi'/2$ (see [19]).

sent the resonance subsystem as

$$\sum_{r', \sigma'} \tilde{D}^{\sigma\sigma'}_{rr'} h^{\sigma'}_{r'} = \tilde{V}^\sigma_r, \quad r, r' \in \mathscr{R}, \quad (3)$$

where $\|\tilde{D}^{\sigma\sigma'}_{rr'}\| \equiv \hat{R} - \hat{U}\hat{M}^{-1}\hat{L}$, $\|\tilde{V}^\sigma_r\| \equiv \hat{u} - \hat{U}\hat{M}^{-1}\hat{v}$.

For further analytical treatment, we will consider this solution in the *main approximation*, taking into account the terms linear in $\tilde{\xi}$, in $\tilde{V}^\sigma_r$, and quadratic terms in $\tilde{D}^{\sigma\sigma'}_{rr'}$. In this approximation, it is sufficient to restrict the analysis by the zeroth-order term in the series expansion $\hat{M}^{-1} = \hat{A}^{-1} + O(\tilde{\xi})$. Then,

$$\tilde{D}^{\sigma\sigma'}_{rr'} = D^{\sigma\sigma'}_{rr'} + \sigma'\sum_N \tilde{\xi}_{r-N}\tilde{\xi}_{N-r'}d^{-1}_N[q^{\sigma-}_N - q^{\sigma+}_N e^{\sigma'\Phi}],$$

$$\tilde{V}^\sigma_r = 2\beta_{-|0}(\delta_{r,0}\delta_{\sigma,-} - \tilde{\xi}_r d^{-1}_0 q^{\sigma-}_0), \quad (4)$$

$$q^{\sigma\sigma'}_N = \delta_{\sigma,\sigma'}[b^+_{\bar{\sigma}|N}e^\Phi + b^-_{\bar{\sigma}|N}e^{-\Phi}] - 2\bar{\delta}_{\sigma,\sigma'}\beta_{\bar{\sigma}|N}.$$

Here, $\bar{\sigma} = -\sigma$, $\bar{\delta}_{\sigma,\sigma'} = 1 - \delta_{\sigma,\sigma'}$.

All the external TCs of Eq. (1) are expressed in terms of the inner TCs with resonance indices, h^σ_r. Thus, the solution of the resonance diffraction problem reduces to that of the resonance subsystem (Eq. (3)). For instance, in the main approximation,

$$T_N = \delta_{N,0}T^F_0 - \sum_{r,\sigma,\sigma'}\sigma\sigma'd^{-1}_N$$

$$\times[b^\sigma_{-|N}\exp[(\sigma'+\sigma)\Phi] + b^{\bar{\sigma}}_{+|N}]\tilde{\xi}_{N-r}h^{\sigma'}_r,$$

$$R_N = \delta_{N,0}R^F_0 - \sum_{r,\sigma,\sigma'}\sigma\sigma'd^{-1}_N \quad (5)$$

$$\times[b^\sigma_{-|N}\exp(\sigma'\Phi) + b^{\bar{\sigma}}_{+|N}\exp(\bar{\sigma}\Phi)]\tilde{\xi}_{N-r}h^{\sigma'}_r,$$
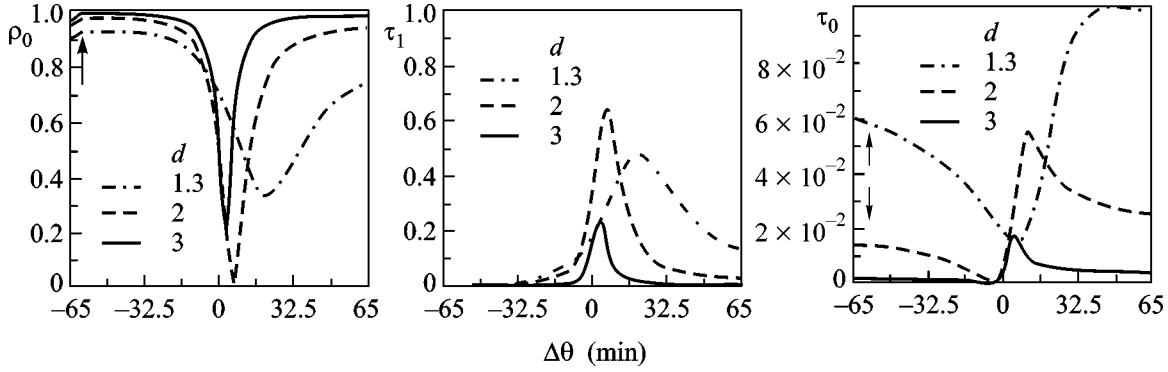
where R^F_0 and T^F_0 are the well-known transmittance and reflectivity coefficients corresponding to the non-modulated film.

The energy flux in the dielectrics is determined by the energy TCs, giving a ratio of the z components of the corresponding Poynting vectors to that of the incident wave,

$$\rho_m = |R_m|^2\frac{\mathrm{Re}(\beta_{-|m})}{\beta_{-|0}}, \quad \tau_m = |T_m|^2\frac{\mathrm{Re}(\beta_{+|m})}{\beta_{-|0}}.$$

When considering the simplest resonance ($|d_r| \ll 1$ for the unique number r, in view of the condition $|b^+_{\sigma|r}| \ll 1$ for one or simultaneously both values of σ, the latter can hold for $\varepsilon_- = \varepsilon_+$), resonance subsystem (3) includes two equations for two main Fourier field

Fig. 2. A single nonsymmetric metal–superstrate SB resonance for a sinusoidal grating. Dependences of homogeneous wave TCs on the angle of incidence, $\Delta\theta = \theta - \theta_i$, for incidence from air onto a Ag film on the quartz substrate, $\varepsilon_+ = 2.31$. Wavelength $\lambda = 1.06$ μm ($\xi_0 = -0.133i + 0.00071$), spacing $\Lambda = 7.41$ μm ($\kappa = 0.143$), film thickness d is shown in skin depths, $\tilde{\xi}_{\pm 1} = 1.53i\sqrt{\xi_0'}$. The arrows in τ_0 and ρ_0 indicate the Rayleigh anomalies (branch points $\beta_{-|1} = 0$).

amplitudes, h_r^+ and h_r^-. The solution presented permits easy numerical calculations for films of arbitrary thicknesses, but to achieve a better insight into the problem and having comparison with the experiment in mind, we concentrate on the results for thick films, $\exp(-\Phi') \ll 1$. In the framework of approximation (4), we obtain from Eq. (3)

$$h_r^\sigma \simeq \frac{2\sigma\tilde{\xi}_r}{\tilde{d}_r}[\delta_{\sigma,-}\tilde{\beta}_{+|r} + (b_{+|r}^\sigma + 2\beta_{-|r})e^{-2\Phi}], \qquad (6)$$

where

$$\tilde{d}_r \equiv \tilde{\beta}_{+|r}\tilde{\beta}_{-|r} - b_{+|r}^- b_{-|r}^- e^{-2\Phi},$$

$$\tilde{\beta}_{\sigma|r} \equiv \beta_{\sigma|r} + \xi_0 + \sum_N \frac{a_{r-N}}{b_{\sigma|N}^+}, \quad a_m \equiv -\tilde{\xi}_m\tilde{\xi}_{-m}. \qquad (7)$$

Assuming absorption to be small, $\xi_0' \ll |\xi_0''|$, we restrict ourselves to modulation of the imaginary part of ξ only. Then, $a_m = |\tilde{\xi}_m|^2$. The denominator, $\tilde{d}_r$, retains contributions of first-order resonance-to-nonresonance scattering processes and vice versa. The processes involving inhomogeneous waves result mainly in a shift of the resonance, while those involving homogeneous ones give rise to the widening. Also, consider the TC for the rth diffraction order. As will be seen below, it may be of great interest for the SB resonance, since, with $\varepsilon_+ \neq \varepsilon_-$, the corresponding Fourier field component may represent an outgoing wave in one of the half-spaces. Using Eqs. (6) and (1), and considering a quasi-harmonic modulation, $|\tilde{\xi}_N| \ll |\tilde{\xi}_{\pm r}|$, we have

$$T_r \simeq \frac{2\tilde{\xi}_r}{\tilde{d}_r}[\tilde{\beta}_{+|r} + b_{+|r}^+ + 2\beta_{-|r} + (b_{+|r}^- + 2\beta_{-|r})e^{-2\Phi}]e^{-\Phi}.$$

The specular coefficients can be simplified as

$$\Delta R_0 \simeq -\frac{2a_r}{\beta_{-|0}\tilde{d}_r}[\tilde{\beta}_{+|r} + (4\beta_{-|r} + 2\beta_{+|r})e^{-2\Phi}],$$

$$\Delta T_0 \simeq \frac{a_r}{\xi_0\tilde{d}_r}(\beta_{-|r} + \xi_0 + \beta_{+|r}), \qquad (8)$$

where $\Delta R_0 \equiv (R_0 - R_0^F)/R_0^F$ and $\Delta T_0 \equiv (T_0 - T_0^F)/T_0^F$. We neglect ξ_0 in comparison with $\beta_{\sigma|0}$, which is valid for not too grazing incidence.

Let examine an substantially nonsymmetric situation, where the resonance condition is fulfilled for a sole number r and a fixed sign of σ, $|\beta_{\sigma|r}| \ll 1$, i.e., an SPP mode is excited at the one of metal–dielectric interfaces. While being the simplest example of SPP excitation, it may provide a very nontrivial light transmission. We choose the case of the metal–superstrate resonance, $\sigma = -$. Estimating the values $|\beta_{\sigma|r}|$ in the resonance vicinity as $|\beta_{-|r}| \simeq |\xi_0|$ and $|\beta_{+|r}| \simeq 1$ (see the discussion above Eq. (2)), we have, for the minimal magnitude of the denominator $\tilde{d}_r$,

$$|\tilde{d}_r|_{\min} \simeq \xi_0' + a_r + O(e^{-2\Phi'}). \qquad (9)$$

Then, Eq. (7) results in $|\Delta T_0| \sim \dfrac{a_r}{|\xi_0|(\xi_0' + a_r)}$. $|\Delta T_0|$ increases with an increase of a_r to become of order one for the modulation amplitude $a_r \sim \xi_0'|\xi_0|$. The zeroth-order transmittance exhibits a saturation for $a_r \gtrsim \xi_0'$ (see Fig. 2) at the level $|T_0|_{\max} \sim |\xi_0|^{-1}|T_0^F|$, being enhanced by the factor $|\xi_0|^{-1}$ as compared with $|T_0^F| \simeq 4|\xi_0|\exp(-\Phi') \ll 1$. The maximal zeroth-order transmittance τ_0 at $\Phi' = 3$ (three skin depths) is about several percent (for $|\xi_0| \simeq 0.1$), while, in the experiment of

Ebbesen *et al.*, the maximal transmittance was about several percent for $\Phi' = 7$. Such an increase apparently may be due to different reasons. First, it is evident that the validity of all above formulas is restricted by the smallness of the modulation amplitude, and, therefore, we cannot suggest a rigorous estimate of the effect for hole array. Second, while measuring the transmitted light intensity in the experiment, the detector could fully register not only the zeroth-order channel but other homogeneous outgoing channels as well (the details concerning the position of the detector have not been reported, in spite of this being an essential point; hence, we cannot make a positive judgment). Note that, in spite of the low transmittance, the reflectivity may have deep resonance minima, and they appear to be more pronounced in the case of SPP excitation at the front surface ($\sigma = -$) than at the back ($\sigma = +$), which follows directly from Eq. (8) for $|\beta_{-|r}| \ll 1$ and $|\beta_{+|r}| \ll 1$, respectively (cf. also [8]).

The transmittance can be increased in two possible ways. One is to adjust the parameters so that excitation of a DB SPP should exist (see below). The other relates to the specific case when the diffraction order of a, SPP excited at one of the interfaces corresponds to a propagating wave in the opposite-side dielectric half-space, and we arrive at "nonzeroth-order, plasmon enhanced light transmittance" Consider the latter case in some detail.

Let a light wave be incident from the dielectric of lower optical density, $\varepsilon_- < \varepsilon_+$, and the diffraction order r correspond to both the homogeneous outgoing wave in the substrate and the SB SPP on the front interface (see Fig. 1 for $r = 1$). In Fig. 2, the ρ_0 minima and τ_1, τ_0 maxima correspond to excitation of a, SPP; τ_0 possesses typical Fano profile. The rth-order transmitted wave becomes the principal channel for light tunneling, resulting in $T_r \simeq 4\tilde{\xi}_r \exp(-\Phi)/[\tilde{\beta}_{-|r} + 2\xi_0\exp(-2\Phi)]$. Since $\tilde{\beta}_{-|r}$ includes a term proportional to $|\tilde{\xi}_r|^2$, there exists an optimal modulation depth, $a_r = a_{opt} \sim \xi_0'$, corresponding to the highest transmittance (see Fig. 3): $\tau_r|_{max} \sim \xi_0'^{-1} \exp(-2\Phi')$ exceeds the maximum value of τ_0 by the factor $\xi_0'^{-1}$. This value of a_r differs only weakly from that corresponding to a totally suppressed specular reflection for the case of diffraction at the interface between the metal and dielectric half-spaces (see [20]). This result is universal for different metals if we renormalize the modulation amplitude using its characteristic value, $\sqrt{\xi_0'}$ so that $w = |\tilde{\xi}_r|/\sqrt{\xi_0'}$ and $w_{opt} \sim 1$. A close-to-total light transmittance, $\tau_r \sim 1$, takes place for film thicknesses of order $\Phi' \sim |\ln\xi_0'|/2$ (see Fig. 3).

A strong nonzeroth-order anomalous transmittance can also occur under the condition that the zeroth-order wave in the substrate is inhomogeneous ($\varepsilon_- > \varepsilon_+$;
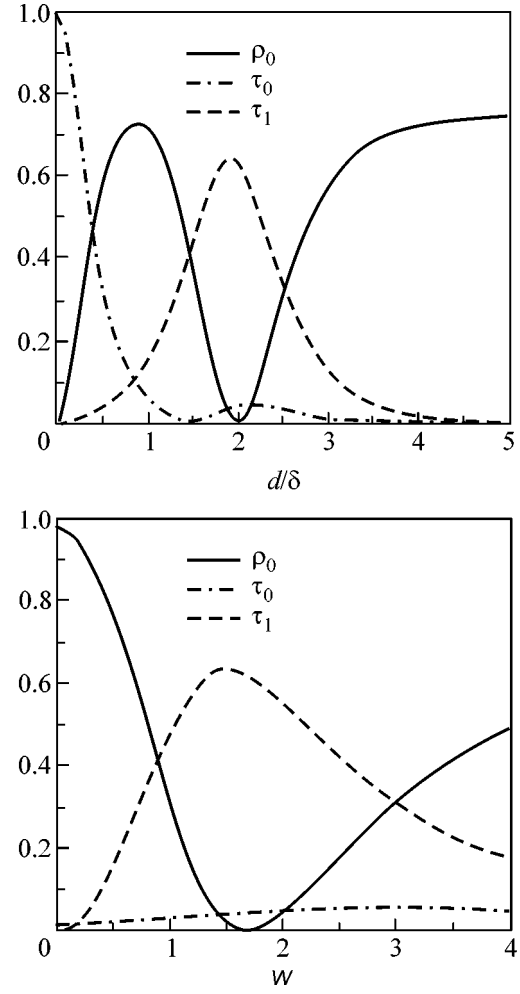
Fig. 3. Modulation amplitude and film thickness dependences of the transmittance and reflectivity (for $d = 2$, in terms of skin depths $\delta = (k^{-1}|\xi_0''|)$, and for $w = 1.53$, $\tilde{\xi}_{\pm1} = iw\sqrt{\xi_0'}$), corresponding to a nonsymmetric, single metal–superstrate SB resonance. The angle of incidence is $\theta = 60°$; other parameters are the same as in Fig. 2.

cf. Kretshmann geometry, [19]). Then, for such an angle of incidence with which the zeroth diffraction order corresponds to SPP excitation on the far interface, $\sqrt{\varepsilon_-}\sin\theta \simeq K^+$, the Nth-order diffracted waves with $|\sqrt{\varepsilon_-}\sin\theta + N\kappa| < \sqrt{\varepsilon_+}$, $N < 0$, $\kappa < 2\sqrt{\varepsilon_+}$ are homogeneous ones. The corresponding TCs can become of the same order as the τ_r of the previous case. The first observation of this effect (in the simplest case and for a dielectric grating deposited on the metal film) was reported in [12]. Besides, for a long-spacing nonharmonic grating, $\kappa < \sqrt{\varepsilon_+}$, the transmitted energy flux is redistributed between these diffraction orders in accordance with the Fourier spectrum of the grating.

Let us briefly discuss more complicated SPP resonances. Along with the resonances related to the excitation of one SPP, double and fourfold resonances can occur under some specific conditions, which result in complex spectral and angular dependences and in additional enhancement of the transmittance peaks (reflectance dips). Recall that, for given values of ε_σ and period Λ, the resonance condition of Eq. (2) defines a resonance curve in the λ–θ (vacuum wavelength and angle of incidence) in the region $-\sqrt{\varepsilon_-} < K^\sigma - \tau r \kappa < \sqrt{\varepsilon_-}$, which is enumerated by two signs, σ, τ, and the integer r. Then, for a fixed θ (and a fixed period), there is a specific value of the wavelength, and vice versa, for a fixed λ, there is a specific value of angle of incidence corresponding to SPP excitation. In the generic case, these curves corresponding to different values of r and σ do not intersect. Then, we arrive at a *single* SB resonance (SBS).

Under specific conditions, different resonance curves may intersect. An intersection of two curves specifies the values of κ and θ corresponding to a *double* resonance. If these curves correspond to equal σ (and two different resonance orders, $r' \ne r$), then a simultaneous excitation of two SPPs on one of the interfaces holds. These SPPs are coupled due to the periodicity, and we arrive at a double SB resonance (SBD). SBDs do not significantly enhance the peak transmittance magnitudes (reflection minima) as compared with the single resonance; however, they result in complex wavelength and angle of incidence dependences. Specifically, the interresonance modulation amplitude, $\tilde{\xi}_{r-r'}$, can strongly effect the resonance behavior even for small magnitudes of order $\gtrsim \xi_0'$ (cf. [20], where a comprehensive examination of such resonances is performed for diffraction on metal–dielectric interfaces). Note that, for symmetric film surroundings, $\varepsilon_+ = \varepsilon_-$, we arrive at the fourfold resonance.[3]

A significant enhancement of the transmittance can be achieved during simultaneous excitation of SPPs on both interfaces, coupled due to the finite film thickness, i.e., when a double DB resonance (DBD) occurs. This corresponds to the intersection of two curves with different σ. Equations (6)–(8) describe the symmetric DBD as well, and the transmittance enhancement is caused by the fact that the minimal magnitude of the resonance denominator, $\tilde{d}_r$, is squared in comparison with Eq. (9), while the nominator does not decrease like in the case of an SBD resonance. The greatest relative change of the zeroth-order transmittance is of order $|\Delta T_0| \sim |\tilde{\xi}_r|^2/|\tilde{d}_r|_{\min} \sim |\tilde{\xi}_r|^2(\xi_0' + |\tilde{\xi}_r|^2 + \dots)^{-2}$. Therefore,

zeroth-order transmittance (along with reflectance and absorbance) anomalies are expressed much stronger for the DB resonances. This fact is in agreement with experimental data and numerical calculations for normal incidence (cf. [6, 13]). The detailed analysis (to be published elsewhere) for this specific case is in agreement with results for harmonic modulation presented in the theoretical paper [9] (up to the shift of the resonance peak and dip positions due to scattering processes involving second-order inhomogeneous diffracted waves, which we take into account).

The approach developed allows a natural generalization to 2D periodic structures (cf. [21] for the half-space problem). The main difference consists in the fact that we have to appeal to a 2D Fourier expansion, $\tilde{\xi}(\mathbf{r}) = \sum_{n_1, n_2} \tilde{\xi}_{n_1 n_2} \exp[(in_1\mathbf{g}_1 + in_1\mathbf{g}_1)\mathbf{r}]$, $\tilde{\xi}_{00} = 0$, where $\mathbf{r} = (x, y)$ and $\mathbf{g}_1$, $\mathbf{g}_2$ are reciprocal vectors relating to minimum translations of the reciprocal lattice. Similar changes need to be performed for the Fourier–Floquet expansion of the electromagnetic field. Consequently, a resonance enhancement of the transmittance can be caused by excitation of an SPP in any diffraction order, now numbered by a pair of integers (r_1, r_2). The approximate resonance condition reads as $|\mathbf{k}_t + r_1\mathbf{g}_1 + r_2\mathbf{g}_2| \simeq K^\pm$, where $\mathbf{k}_t$ is the tangential component of the wave vector of the incident wave, $|\mathbf{k}_t| = k^-\sin\theta = \omega c^{-1}\sqrt{\varepsilon_-}\sin\theta$.[4] The resonance contribution to the TCs depends on the incident polarization and orientation of the SPP excited. Specifically, it depends on the angle φ between the SPP propagation direction relative to the incident plane. No data on the polarization of the incident and transmitted light are given in the majority of experimental works (like the information concerning orientation of the incidence plane); exceptions are [14, 22].[5] Therefore, in the generic geometry, we can obtain a nontrivial transformation of the polarization of the zeroth-order transmitted wave, similar to that discussed for the resonance reflection (cf. [23, 24]). Simple estimates for the magnitudes of these coefficients are analogous to that presented above for the 1D grating.

We have shown that the principal point for the light tunneling enhancement is the existence of well-defined surface modes (SPPs) at the interfaces. A great effect can be caused by the zeroth-order transmittance (which has been observed experimentally and discussed theoretically) and other diffraction orders as well. The latter may exceed the zeroth-order transmittance, τ_0, by factors of about $\xi_0'^{-1}$ in the case of SB resonance, while

---

[3] The *fourfold* DB resonance (DBF) can also exist under the condition that the ratio of the refraction indices of the surrounding dielectrics (or, more exactly, the values of K^+ and K^-) is equal to that of two integers resulting in simultaneous intersection of four resonance curves. Note that threefold resonance is impossible.

[4] In the majority of experimental works devoted to the problem, the double periodicity is realized by square hole arrays (i.e., $(\mathbf{g}_1 \cdot \mathbf{g}_2) = 0$, $g_1 = g_2$).

[5] Simple calculations show that the zeroth-order TC angle dependence with (without) change of polarization can be approximated to $\sin 2\varphi(\cos^2\varphi)$ for the impedance modulation. For the relief modulation, it is necessary to change the angle φ to ψ, where ψ is the angle between the incident plane and the vector $r_1\mathbf{g}_1 + r_2\mathbf{g}_2$.

both zeroth- and nonzeroth-order transmittances under DB resonance diffraction on nonharmonic grating may be comparable.

The analytical approach has allowed us to perform a transparent analytical treatment and identify the role of different parameters. It shows as trivialities some results which seem nontrivial within other approaches. While the modulation is supposed to be small, it is in a sense arbitrary (defined by an arbitrary Fourier expansion), in contrast to numerical calculations where the spectral composition of modulation is fixed.

REFERENCES

1. R. Petit, *Electromagnetic Theory of Gratings* (Springer, Berlin, 1980).

2. *Surface Polaritons*, Ed. by V. M. Agranovich and D. L. Mills (North-Holland, Amsterdam, 1982; Nauka, Moscow, 1985).

3. E. Popov and E. G. Loewen, *Diffraction Gratings and Applications* (Marcel Dekker, New York, 1997).

4. T. W. Ebbesen, H. J. Lezec, H. F. Ghaemi, *et al.*, Nature **391**, 667 (1998).

5. S. A. Darmanyan and A. V. Zayats, Phys. Rev. B **67**, 035424 (2003).

6. N. Bonod, S. Enoch, L. Li, *et al.*, Opt. Express **424**, 428 (2003).

7. U. Schröter and D. Heitmann, Phys. Rev. B **60**, 4992 (1999).

8. M. Sarrazin, physics/0401025 v1 (2004).

9. A. M. Dykhe, A. K. Sarychev, and V. M. Shalaev, Phys. Rev. B **67**, 195402 (2003).

10. E. Popov, N. Nevière, S. Enoch, *et al.*, Phys. Rev. B **62**, 16100 (2000).

11. M. Sarrazin, J.-P. Vigneron, and J.-M. Vigoureux, Phys. Rev. B **67**, 085415 (2003).

12. S. Park, G. Lee, S. H. Song, *et al.*, Opt. Lett. **28**, 1870 (2003).

13. A. Krishnan, T. Thio, T. J. Kim, *et al.*, Opt. Commun. **200**, 1 (2001).

14. W. L. Barnes, W. A. Murray, J. Dintinger, *et al.*, Phys. Rev. Lett. **92**, 107401 (2004).

15. L. D. Landau and E. M. Lifshitz, *Course of Theoretical Physics*, Vol. 8: *Electrodynamics of Continuous Media*, 2nd ed. (Nauka, Moscow, 1982; Pergamon, New York, 1984).

16. A. V. Kats and Y. A. Bludov, Proc. SPIE **5221**, 207 (2003).

17. A. Hessel and A. A. Oliner, Appl. Opt. **4**, 1275 (1965).

18. A. V. Kats, Proc. SPIE **4438**, 157 (2001).

19. H. Raether, *Surface Plasmons on Smooth and Rough Surfaces and on Gratings* (Springer, Berlin, 1988).

20. A. V. Kats and N. A. Balakhonova, Proc. SPIE **5184**, 190 (2003).

21. A. V. Kats and A. Y. Nikitin, Proc. SPIE **5221**, 218 (2003).

22. E. Altewischer, M. P. van Exter, and J. P. Woerdman, physics/0208033 v1 (2002).

23. G. P. Bryan-Brown, J. R. Sambles, and M. C. Hutley, J. Mod. Opt. **37**, 1227 (1990).

24. A. V. Kats and I. S. Spevak, Phys. Rev. B **65**, 195406 (2002).

Glass Formation in Amorphous SiO₂ as a Percolation Phase Transition in a System of Network Defects

M. I. Ojovan

Sir Robert Hadfield Building, University of Sheffield, Sheffield, S1 3JD, United Kingdom
Received May 6, 2004

Thermodynamic parameters of defects (presumably, defective SiO molecules) in the network of amorphous SiO₂ are obtained by analyzing the viscosity of the melt with the use of the Doremus model. The best agreement between the experimental data on viscosity and the calculations is achieved when the enthalpy and entropy of the defect formation in the amorphous SiO₂ network are $H_d = 220$ kJ/mol and $S_d = 16.13R$, respectively. The analysis of the network defect concentration shows that, above the glass-transition temperature (T_g), the defects form dynamic percolation clusters. This result agrees well with the results of molecular dynamics modeling, which means that the glass transition in amorphous SiO₂ can be considered as a percolation phase transition. Below T_g, the geometry of the distribution of network defects is Euclidean and has a dimension $d = 3$. Above the glass-transition temperature, the geometry of the network defect distribution is non-Euclidean and has a fractal dimension of $d_f = 2.5$. The temperature T_g can be calculated from the condition that percolation arises in the defect system. This approach leads to a simple analytic formula for the glass-transition temperature: $T_g = H_d/(S_d + 1.735R)$. The calculated value of the glass-transition temperature (1482 K) agrees well with that obtained from the recent measurements of T_g for amorphous SiO₂ (1475 K). © 2004 MAIK "Nauka/Interperiodica".

PACS numbers: 61.43.Dq; 64.60.Ak; 64.70.Pf; 66.20.+d

Percolation transitions attract considerable interest, because they offer an explanation for a wide class of phenomena [1–3]. For example, the glass transition in spin glasses is explained on the basis of the percolation theory [4]. At the same time, the nature of glass transition in oxide systems is not yet clearly understood [5–8]. Amorphous SiO₂, as the simplest glass-forming material, is suitable for use in the model studies in this area of research. At temperatures higher than $T_g = 1475$ K, amorphous SiO₂ transforms to the supercooled liquid state, whereas, below T_g, it is in the glassy solid state. The changes occurring in the atomic system as the temperature passes through T_g have been much investigated. According to the concept proposed by Hunt, the material at temperatures above T_g is in the percolative transport regime, while at low temperatures, it is in the diffusive transport regime [5]. Major progress in the understanding of the structural changes of an amorphous material passing through T_g was achieved with the help of the molecular dynamics (MD) modeling [6] and, in particular, by studying the Voronoi polyhedra (analogues of the Vigner–Seitz cell) [7, 8]. The MD experiments showed that, in the liquid state, percolation clusters composed of Voronoi coordination polyhedra with low-density atomic configurations are formed in the material, while no such clusters occur in the solid (glassy) state [7]. However, in the solid state, percolation clusters of Voronoi coordination polyhedra with high-density (compact) atomic configurations are

formed [7, 8]. Since the percolation clusters of Voronoi coordination polyhedra with low-density atomic configurations exist in the liquid state only, it is possible to distinguish between the liquid and solid (glassy) states of amorphous materials on the basis of the MD experiments [7]. At the same time, the MD experiments show that, near the glass-transition temperature, the geometry of an amorphous material changes because of the formation of the fractal percolation clusters [2].

This paper shows that, as the temperature passes through T_g in amorphous SiO₂, a percolation transition occurs in the system of the network defects presumably consisting of defective SiO molecules. The transition can be traced analytically, making it possible to derive a simple expression for the glass-transition temperature. The analytic calculation is based on the Doremus viscosity model (D model) relating the viscosity of the amorphous material to the thermodynamic parameters of the network defects [9–11].

An amorphous material can be represented by a topologically disordered network. The three-dimensional network of amorphous SiO₂ consists of SiO₄ tetrahedra bridged by oxygen atoms. A perfect network of an amorphous material has no defects at absolute zero, but defects arise at finite temperatures T. The formation of defects depends on the Gibbs free energy of a defect:

$$G_d = H_d - TS_d, \tag{1}$$

where H_d is the enthalpy and S_d is the entropy of formation of one mole of defects. Doremus assumed that the diffusion and viscous flow in silicates proceed through the formation of defective SiO molecules. The formation of these defects favors the appearance of five-coordinate Si and O atoms, which was confirmed experimentally in [9]. The formation of defects in the network of amorphous SiO$_2$ can be represented by the reaction

$$(-Si-)_{net} + (-O-Si-)_{net}$$
$$\longleftrightarrow (-Si-)_{defect} + (-O-Si-)_{defect}, \tag{2}$$
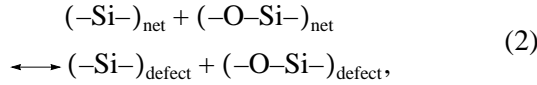
where $(-Si-)_{net}$ and $(-O-Si-)_{net}$ refer to the network and $(-Si-)_{defect}$ and $(-O-Si-)_{defect}$ are the bond-rupture defects. Let the concentration of the elementary blocks of the network be C_0 and the defect concentration be $[(-Si-)_{defect}] = [(-O-Si-)_{defect}] = C_d$. Then, $[(-Si-)_{net}] = [(-O-Si-)_{net}] = (C_0 - C_d)$. The equilibrium reaction constant for (2) depends on the change in the Gibbs energy $G = 2G_d$:

$$K = \exp(-\Delta G / RT). \tag{3}$$

Hence, the equilibrium content of defects is determined as (see also [11, 12])

$$C_d = C_0 \frac{\exp(-G_d/RT)}{1 + \exp(-G_d/RT)}. \tag{4}$$

To calculate the concentration of network defects in amorphous SiO$_2$, it is necessary to know the numerical values of the enthalpy H_d and entropy S_d of defect formation. Both these quantities, H_d and S_d, are involved in the expression for the viscosity in the D model [10, 11]:

$$\eta(T) = \frac{kT}{6\pi r D_0} \exp\left(-\frac{S_m}{R}\right)$$
$$\times \exp\left(\frac{H_m}{RT}\right)\left[1 + \exp\left(-\frac{S_d}{R}\right)\exp\left(\frac{H_d}{RT}\right)\right], \tag{5}$$

where k is the Boltzmann constant, r is the defect radius, $D_0 = f\alpha\lambda^2\nu$, f is the correlation factor, α is the symmetry parameter, λ is the hopping distance, ν is the frequency, and S_m and H_m are the entropy and enthalpy of defect motion. By processing the experimental data on viscosity, it is possible to obtain the exact values of H_d and S_d. The results of this analysis are shown in Fig. 1, which displays the viscosity of amorphous SiO$_2$ calculated from Eq. (5) and the experimental data on viscosity from [13, 14]. The best agreement between the viscosity calculated from Eq. (5) and the experimental data [13, 14] is achieved with $H_d = 220$ kJ/mol and $S_d = 16.13R$, where R is the universal gas constant. Note that the value $H_d = 220$ kJ/mol is practically equal to half the strength of one bond for Si in SiO$_2$ (443 kJ/mol [15]), which agrees with the physical meaning of this quantity.
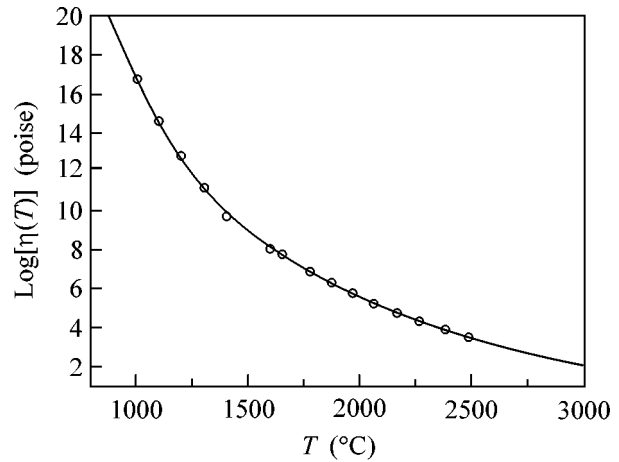
Fig. 1. Viscosity of amorphous SiO$_2$: the curve is calculated from Eq. (5), and the experimental data are taken from [13, 14].
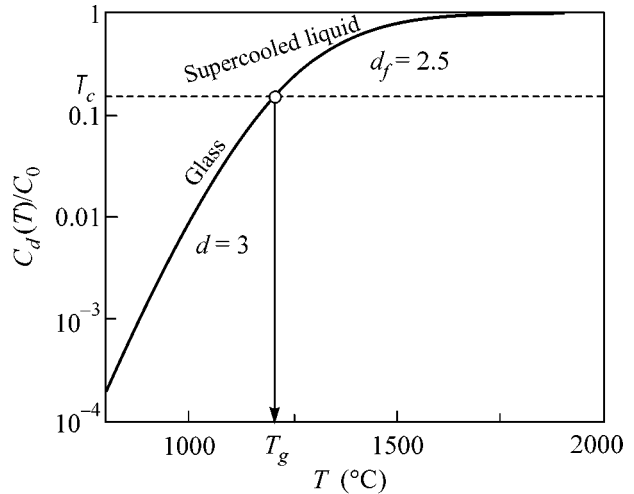
Fig. 2. Concentration of network defects in amorphous SiO$_2$. Above T_g, the defect geometry becomes fractal with the dimension $d_f = 2.5$.

Now, let us consider the evolution of the network defect concentration in amorphous SiO$_2$ with increasing temperature. The results of calculating the relative concentration $\rho = C_d/C_0$ of defects by Eq. (4) are shown in Fig. 2.

The defect clusterization is unlikely as long as the defect concentration is small. As the defect concentration increases, the formation of clusters becomes more and more probable. The relative defect concentration is a function of temperature, $\rho(T) = C_d/C_0$, and increases with temperature T. A percolation cluster of network defects is formed when the relative defect concentration $\rho = C_d/C_0$ reaches the critical value:

$$\rho(T) = \rho_c. \tag{6}$$

For a three-dimensional space, the critical density value is determined by the Scher–Zallen invariant $\vartheta_c = 0.15 \pm 0.01$ [1, 16]. Hence, one can determine from Eq. (6) the percolation transition temperature. Taking into account that $\rho(T)$ in equilibrium can be determined from Eq. (4), we obtain for the glass-transition temperature

$$T_g = \frac{H_d}{S_d + R\ln[(1 - \vartheta_c)/\vartheta_c]}. \tag{7}$$

At temperatures $T < T_g$, no percolation clusters occur in the material and the geometry of the network defects remains Euclidean ($d = 3$). When $T > T_g$, a percolation cluster is formed with the fractal geometry of dimension $d_f = 2.5$ [2]. The network defects are mobile, and, hence, the percolation cluster is dynamic in character (from the viscosity data and from Eq. (5), it follows that the enthalpy of the network defect motion is $H_m = 525$ kJ/mol). Dynamic percolation clusters with the dimension $d_f = 2.6$ were experimentally observed in emulsions [17]. It is also significant that the relaxation processes near the percolation threshold are nonexponential and described by the Kohlrausch law [2–5]. At temperatures $T > T_g$, amorphous SiO_2 is a supercooled liquid, while below T_g, it transforms to the glassy state. Formula (7) for amorphous SiO_2 yields $T_g = 1482$ K. This value is only slightly higher than the known value of $T_g = 1450$ K (see, e.g., [6]). However, it virtually coincides with the recent data of scanning calorimetric measurements: $(T_g)_{exp} = 1475$ K [18].

Thus, the glass formation in amorphous SiO_2 can be considered as a percolation transition in the system of network defects (presumably, defective SiO molecules) with a change in the geometry of the defects from fractal in the liquid state to Euclidean in the glassy state.

REFERENCES

1. B. I. Shklovskiĭ and A. L. Efros, *Electronic Properties of Doped Semiconductors* (Nauka, Moscow, 1979; Springer, New York, 1984).
2. M. B. Isichenko, Rev. Mod. Phys. **64**, 961 (1992).
3. M. I. Klinger, Phys. Rep. **165**, 275 (1988).
4. I. Campbell, P.-O. Mari, A. Alegria, and J. Colmenero, Europhys. News **3/4**, 46 (1998).
5. A. G. Hunt, J. Non-Cryst. Solids **274**, 93 (2000).
6. K. Binder, J. Non-Cryst. Solids **274**, 332 (2000).
7. N. N. Medvedev, A. Geider, and W. Brostow, J. Chem. Phys. **93**, 8337 (1990).
8. A. V. Evteev, A. T. Kosilov, and E. V. Levchenko, Pis'ma Zh. Éksp. Teor. Fiz. **76**, 115 (2002) [JETP Lett. **76**, 104 (2002)].
9. R. H. Doremus, J. Appl. Phys. **92**, 7619 (2002).
10. M. I. Ozhovan, Pis'ma Zh. Éksp. Teor. Fiz. **79**, 97 (2004) [JETP Lett. **79**, 85 (2004)].
11. M. I. Ojovan and W. E. Lee, J. Appl. Phys. **95**, 3803 (2004).
12. J. W. Haus and K. W. Kehr, Phys. Rep. **150**, 263 (1987).
13. G. Urbain, Y. Bottinga, and P. Richet, Geochim. Cosmochim. Acta **46**, 1061 (1982).
14. G. Hetherington, K. H. Jack, and J. C. Kennedy, Phys. Chem. Glasses **5**, 130 (1964).
15. N. M. Pavlushkin, *Fundamentals of Sitalle Technology* (Stroĭizdat, Moscow, 1979) [in Russian].
16. H. Scher and R. Zallen, J. Chem. Phys. **53**, 3759 (1970).
17. M. I. Ozhovan, Zh. Éksp. Teor. Fiz. **104**, 4021 (1993) [JETP **77**, 939 (1993)].
18. R. Bruning, J. Non-Cryst. Solids **330**, 13 (2003).

Translated by E. Golyamina

Evolution of Spin Susceptibility from the Pauli to Curie–Weiss Type in Strongly Correlated Fermi Systems

M. V. Zverev and V. A. Khodel'*

Russian Research Centre Kurchatov Institute, pl. Kurchatova 1, Moscow, 123182 Russia
*e-mail: vak@wuphys.wustl.edu
Received May 11, 2004

The magnetic properties of strongly correlated Fermi systems are studied within the framework of the fermion-condensation model—phase transition associated with the rearrangement of the Landau quasiparticle distribution, resulting in the appearance of a plateau at $T = 0$ exactly in the Fermi surface of the single-particle excitation spectrum. It is shown that the Curie–Weiss term $\sim T^{-1}$ appears in the expression for the spin susceptibility $\chi_{ac}(T)$ of the system after the transition point at finite temperatures. The behavior of $\chi_{ac}(T, H)$ as a function of temperature and static magnetic field H in the region where the critical fermion-condensation temperature T_f is close to zero is discussed. The results are compared with the available experimental data. © *2004 MAIK "Nauka/Interperiodica".*

PACS numbers: 71.10.Hf; 71.27.+a; 75.30.Cr

In recent years, the behavior of strongly correlated Fermi systems in magnetic fields has attracted much attention of both researchers and theorists. In the Landau theory, the magnetic susceptibility $\chi_{ac}(T, H) = \delta\mathcal{M}/\delta H$ ($\mathcal{M}$ is the magnetic moment of the system) depends neither on the static magnetic field H nor on temperature T until the field and temperature are not too high. However, experimentally, χ_{ac} varies with temperature down to absolute zero, and its dependence on H is also far from trivial even at low magnetic fields H [1–8]. To explain the first fact, Anderson's localization theory is often invoked [9], and for the field dependence, one often uses the theory of second-order phase transitions [10–12]. In an alternative approach [13–15], the anomalies in the behavior of the strongly correlated systems in an external magnetic field are treated within the framework of the generalized Fermi-liquid theory, where these anomalies arise in the vicinity of the Fermi-condensation point, i.e., in the vicinity of the phase transition occurring in the Fermi system when the standard quasiparticle distribution (Fermi step at zero temperature, $n_F(p) = \theta(p_F - p)$) becomes unstable [16–26]. As a result, the $n_F(p)$ distribution changes to a new $n_0(p)$ distribution that minimizes the total energy E_0 of the system. It differs from $n_F(p)$ in a certain momentum interval $p_i < p < p_f$ that comprises the Fermi momentum p_F. The Fermi surface "expands": a plateau $\xi(p) = 0$ appears at $p_i < p < p_f$ in the single-particle excitation spectrum. The collection of single-particle excitations in this region of momentum space is referred to as fermion condensate (FC). At finite temperatures, the degeneracy of $\xi(p)$ in the FC region is removed and the

$\xi(p)$ plateau is slightly inclined. Its slope is proportional to T [18]:

$$\xi(p, T \longrightarrow 0) = T\ln\frac{1 - n_0(p)}{n_0(p)}, \quad p_i < p < p_f. \quad (1)$$

After these preliminary remarks, we are in a position to study the magnetic properties of strongly correlated Fermi systems. We will first consider the real part of low-frequency spin susceptibility $\chi_{ac}(T, \omega \longrightarrow 0)$ in zero static magnetic field H. Being the second variational derivative of the energy E_0 with respect to the external field, $\mathrm{Re}\,\chi_{ac}(T)$ is expressed through the real part of the polarization operator $P(T) = (\mathcal{T}_0 G G \mathcal{T})$, where $\mathcal{T}_0 = \mu_B\sigma$ is the bare vertex function (μ_B is the Bohr magneton), $\mathcal{T}$ is the total vertex function, and G is the single-particle Green's function. The brackets stand for integration over all intermediate variables.

Using the standard renormalization procedure, one can rewrite this integral in the form including only the poles G^p of the Green's function G. This part of G is expressed as $G^p(p, \varepsilon) = [\varepsilon - \xi(p) + i\gamma(\varepsilon)]^{-1}$, where the single-particle spectrum $\xi(p) = \epsilon(p) - \mu$ is measured from the chemical potential μ, while the damping constant γ increases after the transition because of the high density of the FC states. However, the damping is still not strong in the energy range $\varepsilon \sim T$ that makes the main contribution to the thermodynamic characteristics: $\gamma(p, \varepsilon \sim T) \sim T$ [21]. Consequently, it is not this quantity that is responsible for the anomalies in the real part of χ_{ac}. If so, the renormalization procedure can be modified using the conventional quasiparticle Green's function $G^q(p, \varepsilon) = [\varepsilon - \xi(p)]^{-1}$. It differs from the Fermi-liquid function only in the spectrum $\xi(p)$, which no longer

coincides with $\xi_{FL}(p) = p_F(p - p_F)/M^*$. As a result, one has [27, 28]

$$\mathrm{Re}\chi_{ac}(T) = \frac{\chi_0(T)}{1 - g_0\Pi_0(T)}, \qquad (2)$$

where g_0 is the zero harmonic of the Landau phenomenological quasiparticle scattering amplitude near the Fermi surface, $\chi_0(T) = -\mu_B^2\Pi_0(T)$, and

$$\Pi_0(T) = \mathrm{Re}\int G^q(\mathbf{p}, \varepsilon)G^q(\mathbf{p}, \varepsilon)n(\varepsilon)\frac{d^4p}{(2\pi)^4 i}$$
$$\equiv \int \frac{dn(\xi)}{d\xi(p)}dv. \qquad (3)$$

The function $n(\varepsilon)$ in this integral has the standard form $n(\varepsilon) = [1 + \exp(\varepsilon/T)]^{-1}$. For definiteness, we restrict ourselves to the three-dimensional case, where the volume element in the momentum space is $dv = d^3p(2\pi)^3$.

The use of Eqs. (2) and (3) beyond the transition point gives the usual T-independent Pauli susceptibility. After the fermion condensation, the substitution of Eq. (1) into Eq. (3) leads to

$$\chi_0(T \longrightarrow 0) = \nu_f\frac{\mu_B^2}{T}\rho \qquad (4)$$

with the dimensionless constant

$$\nu_f = \rho^{-1}\int n_0(p)(1 - n_0(p))dv \qquad (5)$$

proportional to the FC density. In the presence of spin–spin interactions, Eq. (4) is replaced by $\mathrm{Re}\chi_{ac}^{-1}(T) = \chi_0^{-1}(T) + g_0(\rho)/\mu_B^2$ or, equivalently, by

$$\mathrm{Re}\chi_{ac}(T \longrightarrow 0) = \nu_f\frac{\mu_B^2}{T - \Theta_W}\rho. \qquad (6)$$

Therefore, even beyond the quasiparticle description, we arrive at the Curie–Weiss law for $\chi_{ac}(T)$ with the Weiss temperature $\Theta_W = -g_0(\rho)\nu_f\rho$. As was shown in [15], $g_0(\rho)$ is zero at $\rho = \rho_\infty$, so that Θ_W is small in the vicinity of the fermion-condensation point. Experimentally, the Curie–Weiss behavior of the spin susceptibility $\chi_{ac}(T \longrightarrow 0)$ for a small value of Θ_W takes place in a two-dimensional liquid ^{3}He [1, 2] and in a two-dimensional electron gas [3]. Unfortunately, a check of the proposed theory through the direct measurement of the single- particle spectra is as yet hardly possible. The electronic systems of some compounds with an anisotropic Fermi surface, e.g., of Na_xCoO_2 are more suitable for such a verification, because spin susceptibility of this compound has been experimentally measured at various doping levels x [29–31]. We note in this connection that the fermion condensation in anisotropic systems ordinarily involves only part of the Fermi surface, while the remaining part does not participate in

the transition and its T-independent contribution amounts to the renormalization of the $\chi_{ac}^{-1}(T = 0)$ term. Unfortunately, the quality of existing experimental data on single-particle spectra [32] is insufficient for checking the above relationships, because the energy resolution is low.

We now turn to the situation where the fermion-condensation temperature T_f is close to zero. This particular case of quantum critical point was considered in [13]. In this case, the anomalous behavior of $\chi_{ac}(T \longrightarrow 0)$ is determined by the deviation of the spectrum $\xi(p)$ from the Landau form. In the absence of static magnetic fields, such deviations can be examined using the Landau formula [27]

$$\frac{\partial\epsilon(p)}{\partial\mathbf{p}} = \frac{\partial\epsilon_\mathbf{p}^0}{\partial\mathbf{p}} + \int f(\mathbf{p}, \mathbf{p}_1)\frac{\partial n(\xi(p_1))}{\partial\mathbf{p}_1}dv_1, \qquad (7)$$

where $\epsilon_\mathbf{p}^0 = p^2/2M$ is the bare single-particle spectrum, $f(\theta)$ is the spin-independent component of the phenomenological quasiparticle-interaction function $\mathscr{F}(\theta) = f(\theta) = g(\theta)\boldsymbol{\sigma}_1\boldsymbol{\sigma}_2$ with $\cos\theta = \mathbf{p}_1\mathbf{p}_2/p_F^2$, and $\mathbf{p}_1$ and $\mathbf{p}_2$ are momenta of colliding particles.

The fermion-condensation point is found from the condition that the left-hand side of Eq. (7) turns to zero at the Fermi surface; this condition reads

$$p_\infty M f_1/3\pi^2 = 1, \qquad (8)$$

where $f_1 = f_1(p_\infty, p_\infty)$ is the first harmonic of the Legendre polynomial expansion of the $f(\theta)$ amplitude and p_∞ is the momentum of Fermi system with critical density ρ_∞. If the $n_F(p)$ distribution is rearranged as a second-order phase transition, then $d\xi/dp$ reaches minimum exactly at the Fermi surface, giving
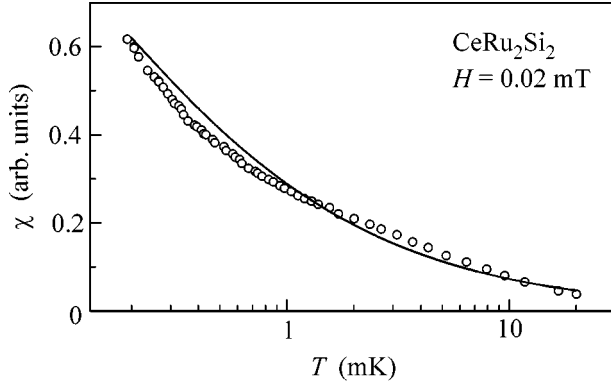
$$p_\infty^2 M f_1'/3\pi^2 = 1, \qquad (9)$$

where $f_1' = (df_1(p_\infty, p)/dp)_{p_\infty}$, and then single-particle spectrum takes the form $\xi(p, T = 0, \rho_\infty) = \xi_3\epsilon_\infty(p - p_\infty)^3/p_\infty^3$, where $\epsilon_\infty = p_\infty^2/2M$,

$$\xi_3 = -p_\infty^3 M f_1''/9\pi^2, \qquad (10)$$
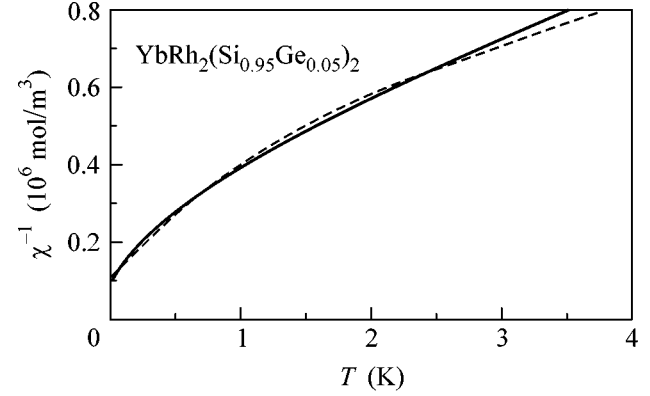
and $f_1'' = (d^2f_1(p_\infty, p)/dp^2)_{p_\infty}$.

At $T \neq 0$, a term with effective mass [13]

$$\xi(p, T, \rho_\infty) = p_\infty\frac{p - p_\infty}{M^*(T, \rho_\infty)} + \xi_3\epsilon_\infty\frac{(p - p_\infty)^3}{p_\infty^3} \qquad (11)$$

Fig. 1. Temperature dependence of the magnetic susceptibility of $CeRu_2Si_2$ in a magnetic field of 0.02 mT. Circles show the data from [8] and solid line is for the calculation of this work.

Fig. 2. Inverse magnetic susceptibility of $YbRh_2(Si_{0.95}Ge_{0.05})_2$ as a function of temperature. Dashes are the data from [7] and solid line is for the calculation of this work.

arises in $\xi(p, T, \rho_\infty)$. The dependence of $M^*(T, \rho_\infty)$ on T can be determined by expanding $f_1(p_\infty, p)p^2$ under the integral in Eq. (7) in powers of $(p - p_\infty)$. Then,

$$\frac{1}{M^*(T, \rho_\infty)} = (f_1' p_\infty + 2 f_1) \int (p - p_\infty) \frac{\partial n(\xi(p))}{\partial p} \frac{dp}{3\pi^2}$$
$$+ \frac{1}{2}(f_1'' p_\infty^2 + 4 f_1' p_\infty + 2 f_1) \int (p - p_\infty)^2 \frac{\partial n(\xi(p))}{\partial p} \frac{dp}{3\pi^2}. \quad (12)$$

According to Eq. (8), the zero term in this expansion and the free term in Eq. (7) cancel out. This equation can be further simplified using the particle number conservation condition rewritten in the integral form:

$$p_F^3 = -\int p^3 \frac{\partial n(\xi(p))}{\partial p} dp. \quad (13)$$

Simple algebra yields

$$p_F \int (p - p_F) \frac{\partial n(\xi(p))}{\partial p} dp$$
$$+ \int (p - p_F)^2 \frac{\partial n(\xi(p))}{\partial p} dp = 0. \quad (14)$$

Here, the contribution from the cubic term is omitted because it is small at low T. After substituting Eq. (14) into Eq. (12), the latter takes the form

$$\frac{M}{M^*(T, \rho_\infty)} = \frac{3\xi_3}{2} \int \frac{(p - p_\infty)^2}{p_\infty^2} \frac{\partial n(\xi(p))}{\partial p} dp. \quad (15)$$

This relation was derived using Eqs. (8)–(10). To simplify the solution, we pass to the new coordinates $z = \xi(p)/T$, $\tau = T/\epsilon_\infty$, and $y = \tau^{-1/3} \xi_3^{1/3} (p - p_\infty)/p_\infty$. Then,

$$\frac{M}{M^*(\tau, \rho_\infty)} = \frac{3}{2} \kappa \xi_3^{1/3} \tau^{2/3}, \quad (16)$$

where κ enters two equations,

$$z = y[3\kappa + y^2] \quad (17)$$

and

$$\kappa = \int_{-\infty}^{\infty} y^2 \frac{e^z}{(1 + e^z)^2} dz, \quad (18)$$

and, obviously, depends neither on ξ_3 nor on T. One can see from Eq. (16) that the effective mass $M^*(T, \rho_\infty)$ at the critical point of an isotropic system decreases with increasing T as $T^{-2/3}$.

By calculating κ, one can not only determine the effective mass but also calculate the susceptibility $\chi_0(T \longrightarrow 0, \rho_\infty)$ using Eq. (3). After some algebra, one gets

$$\chi_0(\tau \longrightarrow 0, \rho_\infty) = \mu_B^2 N_0(0) X \tau^{-2/3}, \quad (19)$$

where $N_0(0) = p_F M/\pi^2$ is the density of single-particle states in the absence of interaction and

$$X = \frac{2}{3\xi_3^{1/3}} \int_{-\infty}^{\infty} \frac{e^z}{(1 + e^z)^2} \frac{dz}{\kappa + y^2}. \quad (20)$$

As before, the inclusion of spin–spin interaction g_0 results in the appearance of a temperature-independent parameter, so that

$$\chi_{ac}^{-1}(\tau \longrightarrow 0, \rho_\infty) = \mu_B^{-2}[g_0 + N_0^{-1}(0) X^{-1} \tau^{2/3}] \quad (21)$$

at sufficiently low temperatures.

Therefore, the critical index α, which characterizes the temperature behavior of spin susceptibility at the quantum critical point, is equal to 2/3 [15], in distinction to 1/2 obtained in [13]. As was pointed out above, g_0 turns to zero at the fermion-condensation point. As a result, the temperature-independent term in Eq. (21) becomes small in the vicinity of this point. A compari
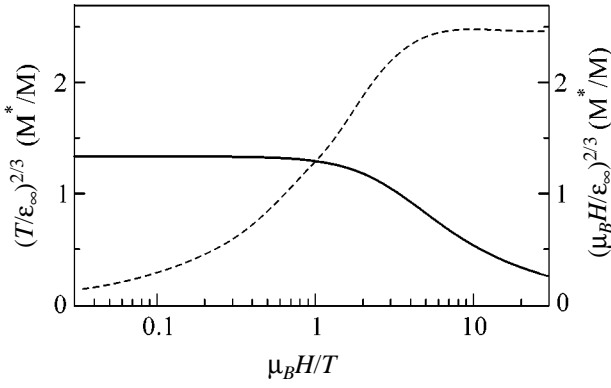
Fig. 3. Dependences of the ratios (solid line) $(T/\varepsilon_\infty)^{2/3}M^*/M$ and (dashes) $(\mu_B H/\varepsilon_\infty)^{2/3}M^*/M$ on the scaling variable $R = \mu_B H/T$ for $\xi_3 = 1$.

son of the results of theoretical calculations with the data obtained in [7, 8] (Figs. 1, 2) confirms the validity of this conclusion.

Analysis shows that heat capacity in the vicinity of quantum critical point also behaves in a different way than in the Fermi-liquid theory. Indeed, using the formula for heat capacity at $\rho = \rho_\infty$ and $T \longrightarrow 0$

$$C(T) = 2\int\xi(p)\frac{dn(\xi, T)}{dT}dv, \qquad (22)$$

one can easily obtain the expression

$$\frac{C(T \longrightarrow 0, \rho_\infty)}{T} = N_0(0)Y\tau^{-2/3}, \qquad (23)$$

after the same algebra as in the calculation of $\chi_0(T \longrightarrow 0, \rho_\infty)$, where

$$Y = \frac{2}{3\xi_3^{1/3}}\int_{-\infty}^{\infty}\frac{e^z}{(1+e^z)^2}\frac{z^2 dz}{\kappa + y^2} \qquad (24)$$

is independent of temperature. Therefore, $C(T \longrightarrow 0, \rho_\infty) \sim T^{1/3}$. Such a behavior of $C(T)$ is observed in YbRh$_2$(Si$_{0.95}$Ge$_{0.05}$)$_2$ at $T < 50$ mK (see Fig. 1 in [7]).

Clearly, the density ρ in a real experiment is always different from the critical value ρ_∞. As a result, one more dimensionless parameter $M^*(\rho)/M$ appears in the formulas before the transition point, after which it gives way to the parameter v_f characterizing the FC density. In particular, Eq. (19) for small v_f is replaced by

$$\chi_0(\tau \longrightarrow 0, \rho_\infty) = \mu_B^2 N_0(0)\left(\frac{2}{3}v_f\tau^{-1} + X\tau^{-2/3}\right). \qquad (25)$$

One can see that the FC contribution dominates at $\tau \longrightarrow 0$ when $\tau < v_f^3$. Such a behavior is observed in YbRh$_2$(Si$_{0.95}$Ge$_{0.05}$)$_2$ at $T < 0.3$ K [7].

The presence of the $\xi(p)$ plateau manifests itself much more efficiently in the resistivity $\rho(T)$: if this pla-

teau exists, a particle can be scattered into the FC. This contribution is independent of v_f and proportional to the temperature T (see Eq. (7.13) in [19]), whereas the off-condensate contribution to $\rho(T)$ is proportional to $T^{4/3}$ because of the softening of the $\xi(p)$ spectrum. Indeed, the resistivity of YbRh$_2$(Si$_{0.95}$Ge$_{0.05}$)$_2$ varies linearly with T at low T (see Fig. 2 in [7]).

We now consider the situation where an additional static magnetic field H is applied to the system. In this case, a new dimensionless parameter $R = \mu_B H/T$ comes into play. Two subsystems appear with the single-particle spectra $\xi_+(p)$ and $\xi_-(p)$ shifted by $\mu_B H$, $n(\xi(p))$ in Eqs. (7), (13), (14) is replaced by $[n(\xi_+(p)) + n(\xi_-(p))]/2$, where $n(\xi_\pm(p)) = [1 + \exp(\xi(p)/T \pm R/2)]^{-1}$, and $\xi(p)$ is given by Eq. (11). At sufficiently small H, the difference in effective masses M_-^* and M_+^* can be ignored, so that $M_-^*(H, T) = M_+^*(H, T) = M^*(H, T)$. To find $M^*(H, T)$, one can again use Landau relation (7) generalized to the case of external magnetic fields. Then, after the same transformations as were carried out above, one obtains

$$\frac{M}{M^*(H, T, \rho_\infty)}$$
$$= \frac{3}{4}\xi_3\int\frac{(p-p_\infty)^2}{p_\infty^2}\left[\frac{\partial n(\xi_+(p))}{\partial p} + \frac{\partial n(\xi_-(p))}{\partial p}\right]dp. \qquad (26)$$

By passing, as before, to dimensionless variables, we find

$$\frac{M}{M^*(\tau, R, \rho_\infty)} = \frac{3}{2}\xi_3^{1/3}\tau^{2/3}\kappa(R), \qquad (27)$$

where $\kappa(R)$ is determined from the condition

$$\kappa(R) = \frac{1}{2}\int_{-\infty}^{\infty}y^2\left(\frac{e^{z+R/2}}{(1+e^{z+R/2})^2} + \frac{e^{z-R/2}}{(1+e^{z-R/2})^2}\right)dz, \qquad (28)$$

while the variables y and z are related by Eq. (17). In the limit $T \longrightarrow 0$, or, equivalently, $R \longrightarrow \infty$, these equations are solved analytically to give $M^*(H, T = 0, \rho_\infty) \sim H^{-2/3}$. The critical index $2/3$, which determines, according to this equation, the change in the effective mass $M^*(H, T = 0, \rho_\infty)$ in a static magnetic field, was found by a different method in [13]. The behavior of $M^*(H, T, \rho_\infty)$ at finite R values is determined by the numerical solution of the set of Eqs. (17) and (28). The dependences of the $(T/\varepsilon_\infty)^{2/3}M^*(H, T, \rho_\infty)/M$ and $(\mu_B H/\varepsilon_\infty)^{2/3}M^*(H, T, \rho_\infty)/M$ ratios on the variable R are shown in Fig. 3 for $\xi_3 = 1$. The fact that the first ratio tends to a constant at $R \ll 1$ illustrates the analytically found asymptotic behavior $M^*(H = 0, T, \rho_\infty) \sim T^{-2/3}$, while the tendency of the second ratio to a constant in the limit $R \gg 1$ reflects the behavior of effective mass in the inverse asymptotic form $M^*(H, T = 0, \rho_\infty) \sim H^{-2/3}$.

The calculation of magnetic moment $\mathcal{M}(H, T, \rho_\infty)$ in the limit $R \longrightarrow \infty$ gives $\mathcal{M}(H, T \longrightarrow 0, \rho_\infty) \sim H^{1/3}$. This dependence is in accordance with the one obtained in [13] and with the experimental data obtained in [8]. In the general case of finite R, the magnetic moment $\mathcal{M}(H, T, \rho_\infty)$ and the spin susceptibility $\chi(H, T, \rho_\infty)$ demonstrate the scaling behavior, as follows from Eqs. (3), (17), and (28):

$$\mathcal{M}(H, T, \rho_\infty) = \mu_B N_0(0)\varepsilon_\infty \tau^{1/3}\tilde{X}(R), \qquad (29)$$

$$\chi(H, T, \rho_\infty) = \mu_B^2 N_0(0)\tau^{-2/3}X(R), \qquad (30)$$

where the function $X(R)$ is given by

$$X(R) = \frac{2}{3\xi_3^{1/3}}$$

$$\times \int_{-\infty}^{\infty}\left(\frac{e^{z+R/2}}{(1+e^{z+R/2})^2} + \frac{e^{z-R/2}}{(1+e^{z-R/2})^2}\right)\frac{dz}{\kappa+y^2}, \qquad (31)$$

and $d\tilde{X}/dR = X(R)$.

By acting in a similar way, one can easily obtain the expression $C(H, T, \rho_\infty)/T$ for the finite R values:

$$\frac{C(H, T, \rho_\infty)}{T} = N_0(0)\tau^{-2/3}Y(R), \qquad (32)$$

where

$$Y(R) = \frac{2}{3\xi_3^{1/3}}$$

$$\times \int_{-\infty}^{\infty}\left(\frac{e^{z+R/2}}{(1+e^{z+R/2})^2} + \frac{e^{z-R/2}}{(1+e^{z-R/2})^2}\right)\frac{z^2 dz}{\kappa+y^2}. \qquad (33)$$

The results of numerical calculations are presented in Fig. 4. This figure also shows the ratio of the susceptibility $\chi_{ac}(T)$ to its value at the peak point T_P, calculated as a function of the T/T_P ratio in this work and found in [8] for three values of magnetic field. The comparison shows that our calculation provides good quantitative description of the scaling behavior of magnetic susceptibility, with the result being independent of the parameter ξ_3. It is worthy of note that this scaling is destroyed in the three-dimensional systems when the magnetic field starts to affect the orbital motion of particles.

It follows from Eqs. (30) and (32) that the ratio $W = \chi_{ac}(H, T, \rho_\infty)T\pi^2/\mu_B^2 C(H, T, \rho_\infty)$ is a function of only variable R. In the $R \longrightarrow 0$ limit, i.e., in the absence of the external field, calculation gives $W \simeq 6$. For the opposite limit $R \longrightarrow \infty$, i.e., at $T \longrightarrow 0$, and for the external field $H \gg T/\mu_B$, one obtains $W \simeq 3$, which is close to the result of the Landau theory.

We note in conclusion that we have studied the behavior of strongly correlated Fermi systems in an
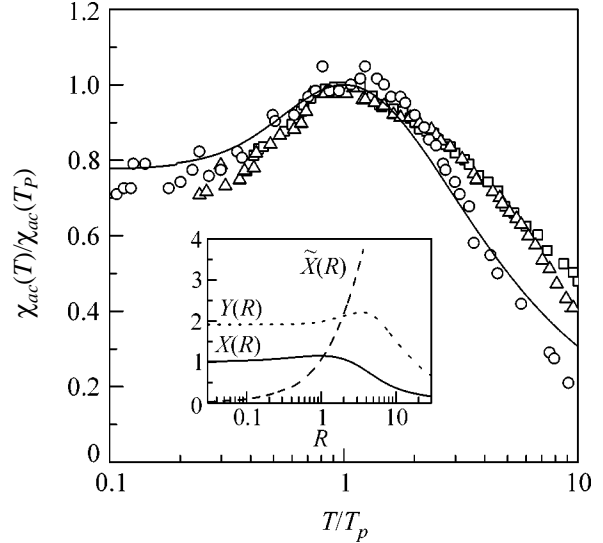
Fig. 4. Reduced magnetic susceptibility $\chi_{ac}(T)/\chi_{ac}(T_P)$ of CeRu$_2$Si$_2$ as a function of reduced temperature T/T_P in magnetic fields of (squares) 0.20 mT, (triangles) 0.39 mT, and (circles) 0.94 mT [8] and (solid line) universal scaling behavior of the same quantity obtained in this work. Inset: scaling functions (solid line) $X(R)$, (dashed line) $\tilde{X}(R)$, and (dotted line) $Y(R)$. Normalization condition is $X(0) = 1$.

external field in the range of parameters where the effective mass M^* diverges and the standard Fermi-liquid description fails. We have found that, as the point where $M^* = \infty$ is approached, the spin susceptibility $\chi_{ac}(T \longrightarrow 0)$ starts to diverge following the law $\chi_{ac}^{-1}(T \longrightarrow 0) \sim T^\alpha$ with the critical index $\alpha = 2/3$. After the phase-transition point, where a plateau appears in the spectrum of single-particle excitations, the critical index changes to $\alpha = 1$. Thus, as the correlations become stronger, the spin susceptibility changes its behavior from the Pauli type to the Curie–Weiss type without any evidence of the localization of single-particle motion.

REFERENCES

1. C. Bäuerle *et al.*, J. Low Temp. **110**, 333 (1998).
2. C. Bäuerle *et al.*, J. Low Temp. **110**, 345 (1998).
3. O. Prus *et al.*, Phys. Rev. B **67**, 205407 (2003).
4. O. Trovarelli *et al.*, Phys. Rev. Lett. **85**, 626 (2000).
5. J. Plessel *et al.*, Phys. Rev. B **67**, 180403 (2003).
6. R. Küchler *et al.*, Phys. Rev. Lett. **91**, 066405 (2003).
7. P. Gegenwart *et al.*, Acta Phys. Pol. B **34**, 323 (2003).
8. D. Takahashi *et al.*, Phys. Rev. B **67**, 180407 (2003).

9. A. Casey *et al.*, Phys. Rev. Lett. **90**, 115301 (2003).

10. S. Sachdev, *Quantum Phase Transitions* (Cambridge Univ. Press, Cambridge, 1999).

11. P. Coleman and C. Pepin, Physica B (Amsterdam) **312–313**, 383 (2002).

12. L. Zhu, M. Garst, A. Rosch, and Q. Si, Phys. Rev. Lett. **91**, 066404 (2003).

13. V. R. Shaginyan, JETP Lett. **77**, 99 (2003); JETP Lett. **79**, 286 (2004).

14. V. A. Khodel, P. Schuck, and M. V. Zverev, Phys. At. Nucl. **66**, 1871 (2003).

15. J. W. Clark, V. A. Khodel, and M. V. Zverev, cond-mat/0403522.

16. V. A. Khodel and V. R. Shaginyan, JETP Lett. **51**, 553 (1990); Condens. Matter Theor. **12**, 221 (1997).

17. G. E. Volovik, JETP Lett. **53**, 222 (1991).

18. P. Nozières, J. Phys. I **2**, 443 (1992).

19. V. A. Khodel, V. V. Khodel, and V. R. Shaginyan, Phys. Rep. **249**, 1 (1994).

20. V. A. Khodel, J. W. Clark, and V. R. Shaginyan, Solid State Commun. **96**, 353 (1995).

21. J. Dukelsky *et al.*, Z. Phys. B **102**, 2 (1997).

22. D. Lidsky *et al.*, Phys. Rev. B **57**, 1340 (1998).

23. M. R. Norman, in *High Temperature Superconductivity*, Ed. by S. E. Barnes, J. Ashkenazi, J. L. Cohn, and F. Zuo (AIP, Woodbury, 1999), p. 298.

24. M. V. Zverev, V. A. Khodel, and J. W. Clark, JETP Lett. **74**, 46 (2001).

25. V. Yu. Irkhin, A. A. Katanin, and M. I. Katsnelson, Phys. Rev. Lett. **89**, 076401 (2002).

26. V. A. Khodel and M. V. Zverev, Physica B (Amsterdam) **312–313**, 506 (2002).

27. L. D. Landau and E. M. Lifshitz, *Course of Theoretical Physics*, Vol. 5: *Statistical Physics*, 3rd ed. (Nauka, Moscow, 1976; Pergamon Press, Oxford, 1980), Part 2.

28. A. A. Abrikosov, L. P. Gor'kov, and I. E. Dzyaloshinskiĭ, *Methods of Quantum Field Theory in Statistical Physics* (Fizmatgiz, Moscow, 1962; Prentice Hall, Englewood Cliffs, N.J., 1963).

29. F. C. Chou *et al.*, cond-mat/0306659.

30. M. L. Foo *et al.*, cond-mat/0312174.

31. F. C. Chou, J. H. Cho, and Y. S. Lee, cond-mat/0404061.

32. H.-B. Yang *et al.*, cond-mat/0310532.

Translated by V. Sakun

Nuclear Spin–Lattice Relaxation in Finely Dispersed Carbonizate Powders

G. V. Mamin[1, 2, *], Haruhiko Suzuki[2], M. S. Tagirov[1], D. A. Tayurskii[1], and A. N. Yudin[1]

[1]*Department of Physics, Kazan State University, ul. Lenina 18, Kazan, 420008 Tatarstan, Russia*
[2]*Physics Department, Kanazawa University, 920-1192 Kanazawa, Japan*
*e-mail: george.mamin@ksu.ru
Received April 23, 2004; in final form, May 11, 2004

Finely dispersed carbonizate powders were studied with the aim of revealing their suitability for producing hyperpolarized noble gases. In the temperature and frequency dependences obtained over a wide range of temperatures and magnetic fields for the spin–lattice relaxation times of the magnetic moments of ^{3}He, ^{1}H, and ^{13}C nuclei, anomalous features caused by the suppression of the exchange between surface paramagnetic centers in a magnetic field were observed. It is shown that the interaction with magnetic moments of the ^{1}H nuclei situated near the paramagnetic centers is the main polarization-leakage channel for the noble-gas nuclear spins. © 2004 MAIK "Nauka/Interperiodica".

PACS numbers: 76.60.Es

At present, optical pumping [1, 2] and polarization of solid ^{3}He and ^{129}Xe by "crude force" in strong magnetic fields at ultralow temperatures, followed by fast melting [3], are the main methods of obtaining hyperpolarized noble gases, such as ^{3}He and ^{129}Xe. The first method is characterized by a rather low output, while the second requires complex equipment and a large amount of coolants for producing ultralow temperatures (lower than 1.3 mK). That is why the study of the possibility of using the dynamic polarization of noble-gas nuclear spins is of undeniable interest. This method is based on the polarization transfer from the electronic subsystem (e.g., paramagnetic centers of a solid substrate contacting the noble gas or the corresponding liquid) to the nuclear spins. An obvious advantage of this method is the fact that, since the polarization of electron-spin system exceeds, under the same conditions, the polarization of nuclear magnetic moments by more than a factor of 1000, no complex cryogenic equipment is required to achieve ultralow temperatures and strong magnetic fields. The output of this method is also expected to be higher than in the case of optical pumping.

The dynamic polarization of liquid or gaseous ^{3}He can be accomplished using the Overhauser and solid state effects. In the first method, spin-polarization transfer to nuclei occurs from delocalized electron moments (conduction electrons in metals), while the second method is based on the polarization transfer from the localized electron magnetic moments in dielectrics. The solid state effect is more preferable to liquid ^{3}He for the reasons pointed out in [4]. In [5], it was proposed that finely dispersed powders of dielectric Van-Vleck paramagnets should be used as a solid

substrate. Finely dispersed carbonizate powders [6] with a well-developed surface capable of adsorbing large amount of gas and containing many paramagnetic centers at their surfaces [7] also show considerable promise as substrate. The EPR line of these centers is strongly narrowed due to the exchange interaction and can be easily saturated. Magnetic coupling between the surface paramagnetic centers and the ^{3}He nuclear spins was revealed from the change in the EPR spectra upon filling a tube with carbonizate by gaseous ^{3}He [8]. Classical estimate of the maximal enhancement of the ^{3}He NMR signal for the scalar second-type relaxation [9] gives a value of 430 in this case.

Nevertheless, attempts to dynamically polarize ^{3}He gas in this system have failed [6]. This failure can be due to the presence of polarization-leakage channels to magnetic nuclei of other types in the system. The carbon–noble gas systems contain, apart from the polarized noble gas, nuclei of other carbon isotope ^{13}C (natural abundance 1.108%) and the OH chains remaining after pyrolysis and containing ^{1}H nuclei. The purpose of this work was to thoroughly study this system and reveal the main channels through which the electron-spin polarization can be carried away, so that one can choose in the future a carbon type that will have the minimal parasitic polarization-leakage channels.

SAMPLE PREPARATION

Carbon obtained by fructose pyrolysis was used as a starting material. To obtain finely dispersed carbonizate, a fructose powder was placed in a tube evacuated by a backing pump. Upon heating, the fructose tubes melted and, at temperatures above 600°C, started to
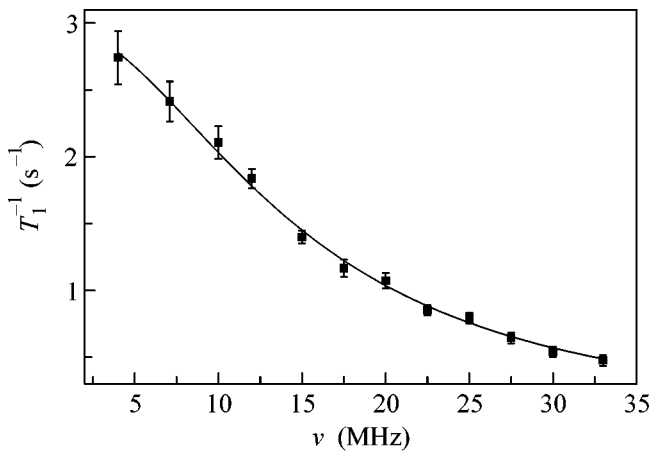
Fig. 1. Frequency dependence of the ^{13}C NSLR rate. Approximation of the experimental data by Eq. (1) is shown by the solid line. Approximation parameters: $C = (0.25 \pm 0.1) \times 10^{+9}$ and $\tau = (11.2 \pm 0.7) \times 10^{-9}$ s.
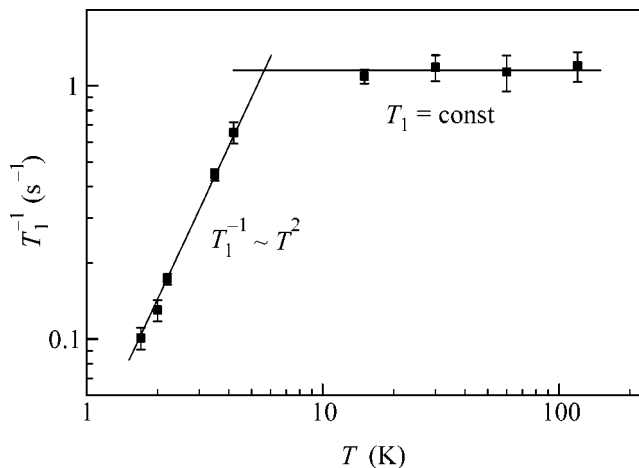
Fig. 2. Temperature dependence of the ^{13}C NSLR rate.

decompose into carbon and water. Continuously evacuated chemical decay products foamed the fructose mass and, after the pyrolysis was completed, the final product consisted of small bubbles with thin walls (about 1 μm). It is likely that one can control the fructose foaming by varying the temperature and heating rate and, hence, vary the wall thickness and chemical composition. Therein lies the main distinction from carbonizates prepared through the wood pyrolysis, because in this case the wall thickness fully depends on the structure of the wood used.

Grinding gave a powder consisting of small flakes. Then, the powder was sieved through a set of sieves to calibrate the particle sizes. Upon measuring the EPR linewidth in the course of filling the tube with gaseous ^3He, one could judge the presence of a magnetic coupling between the paramagnetic samples and ^3He

nuclei. Since this change was most pronounced in the powders with particles 150–250 μm in size, they were used in our study of the nuclear spin–lattice relaxation (NSLR).

EXPERIMENTAL

To study the NSLR, the powder was poured into a U-shaped quartz tube. The tube was pumped out for several days at a temperature of 200°C by a diffusion pump. The increased temperature was used for a more efficient evacuation of absorbed water, to attain good reproducibility of the proton NSLR results. After cooling the sample to room temperature, the tube was hermetically sealed. To study the ^3He NSLR, the corresponding gas was admitted into the tube up a pressure of 0.9 atm before sealing. The helium volume in the tube was equal to 1.8 cm^3 per 80 mg of carbonizate. The amount of inert gas absorbed by the carbonizate at room temperature was negligibly small. Our estimates of the carbonizate surface area showed that only a ^3He monolayer could form at low temperatures in the case of complete gas absorption. The NMR spectrometer coil was winded as a bare single-core copper wire over the quartz tube, and the tube was fixed through the protruding stems. This allowed us to minimize the influence of constructive elements containing ^1H nuclei. The NSLR was measured using a pulsed spectrometer with a working frequency range of 4–35 MHz. The spin–lattice relaxation rate was measured by the standard method with the detection of spin–echo recovery after the pumping pulse. The temperature below 4.2 K was achieved by evacuating the vapor of liquid ^4He from the cryostat. To measure the temperature dependences above 4.2 K, a flow-type helium anticryostat was used.

RESULTS

We measured the frequency (or, in other words, field) and temperature dependences of the ^{13}C and ^1H nuclear relaxation times in the sample, as well as the nuclear magnetization of gaseous ^3He in contact with carbonizate.

The magnetization recovery curve for the ^1H and ^3He nuclei is well described by a single exponential, whereas the same curve for ^{13}C has a more complicated shape $1 - \exp(-(t/T_1)^\alpha)$ typical of the nuclear magnetic-moment relaxation in powders [10]. The frequency dependence of the ^{13}C NSLR time is shown in Fig. 1. The coefficient α does not change its value of 0.66 over the entire frequency and temperature ranges. This dependence can be described by the expression

$$T_1^{-1} = \frac{C\tau}{1 + \tau^2(2\pi\nu)^2}, \qquad (1)$$

which is valid for the nuclear-spin relaxation through the paramagnetic impurities [9] in the fast-diffusion

approximation. In Eq. (1), $\tau \sim 10$ ns is the characteristic correlation time of the system of paramagnetic spins.

One can clearly distinguish two regions in the temperature dependence of the ^{13}C NSLR time (Fig. 2). At temperatures below 10 K, the NSLR rate is proportional to T^2. The fact that the NSLR rate is independent of temperature above 10 K is evidence of the presence of mechanisms restricting relaxation.
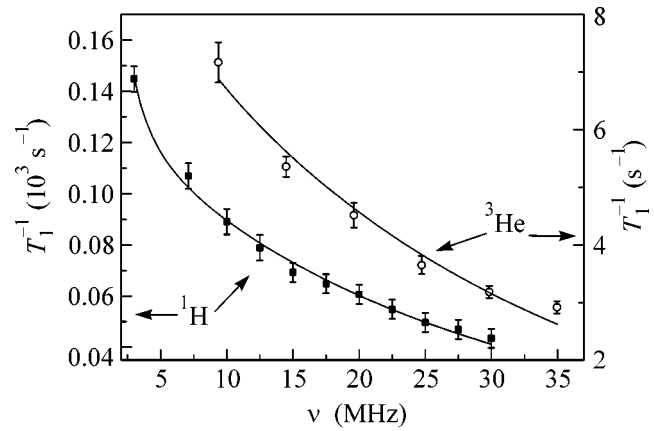
In contrast to the frequency dependence of the ^{13}C NSLR rate, the dependences of the ^1H and ^3He NSLR rates have a more complicated form (Fig. 3). One can also see that these dependences are similar. At low temperatures, the relaxation rate increases approximately as $T^{0.36}$ at 30 MHz and as $T^{0.08}$ at 3 MHz. For the ^1H nuclei, the relaxation rate increases, though it is decelerated more and more with temperature, and, starting at 60 K, the NSLR slows down with increasing temperature.

Fig. 3. Frequency dependences of the ^1H and ^3He NSLR rates at $T = 4.2$ K. Approximations of the experimental data ($\square$ ^1H and $\circ$ ^3He) by Eq. (2) are shown by the solid lines. The parameter $K = (35 \pm 2) \times 10^{-9}$ s is the same for both nuclei.

DISCUSSION

Since all measured NSLR times are short, one can assume that the nuclear magnetic-moment relaxation through the paramagnetic impurities is the dominant relaxation mechanism. Unpaired electrons placed at the surfaces of carbon particles are paramagnetic centers (PCs) in the substance under study. These PCs are combined into clusters, whose inner exchange interaction strongly narrows the EPR line [7]. In fact, we observed signals from three types of nuclei differently arranged about the paramagnetic centers:

(1) from the ^{13}C nuclei homogeneously distributed over the volume of carbon grain;

(2) from protons situated at the sample surface in the immediate vicinity of the paramagnetic centers, because an unpaired electron most likely appears as a result of breaking the C–OH bond; and

(3) from the spins of the ^3He nuclei situated outside the particle volume.

Spin relaxation of the ^{13}C nuclei is nonexponential and corresponds to the relaxation in a system with a limited size and $\alpha = 0.66$ [10]. The coefficient $\alpha = (D + d)/6$ is determined by the dimensionality D of nuclear distribution and the reduced dimensionality d of the distribution of dipole–dipole interaction between the nuclear magnetic moment and the paramagnetic centers. Since the particle thickness (≈ 1 μm) far exceeds the mean distance (≈ 1 nm) between the nuclei of less-abundant ^{13}C isotope, one can assume that the ^{13}C distribution in the particle volume is three-dimensional. Then, the reduced dimensionality d corresponding to the distribution of the average distance between the paramagnetic centers and the ^{13}C nuclei equals 1. The system of paramagnetic centers is placed at the particle surface, so that the nuclear spin diffuses to the nearest PC, i.e., perpendicular to the particle surface. In this case, the parameter d describes the variation of a "one-dimensional" parameter, namely, the particle thickness in the powder. At low temperatures, the temperature and frequency dependences can be explained by fast spin diffusion [9]. The parameter $\tau \sim 11 \times 10^{-9}$ s obtained from the approximation of the frequency dependence is determined by the characteristic exchange-interaction time in the paramagnetic clusters, because it is much shorter than both the PC spin–lattice relaxation time $T_1 \sim 10^{-3}$ s and the PC spin–spin relaxation time $T_2 \sim 10^{-6}$ s.

The observed increase in the relaxation rate with temperature is caused by the rise in the fluctuation amplitude of the local fields produced by the paramagnetic centers. However, the same local fields hamper the magnetization transfer from the ^{13}C nuclei located inside the carbon particle to the rapidly relaxing ^{13}C near the surface PCs, so that the NSLR rate at temperatures above 10 K becomes temperature-independent. In summary, one can say that the ^{13}C spin relaxation is governed by two processes: spin diffusion from the particle volume to the surface and relaxation of the near-surface ^{13}C nuclei in the strongly fluctuating PC magnetic fields. The temperature dependence of the NSLR rate illustrates the transition between the two regimes: at low temperatures, the bottleneck of this process is determined by the ^{13}C relaxation in the fluctuating fields of surface PCs, and at temperatures above 10 K, by the magnetization transfer between the ^{13}C nuclei through the spin diffusion in inhomogeneous local magnetic fields.

The relaxation of ^1H spins situated at the particle surfaces has a nondiffusive character. One can also note that the ^1H linewidth ($\Delta = 48$ kHz) is larger than the ^{13}C ($\Delta = 14$ kHz) and ^3He ($\Delta = 4.2$ kHz) NMR linewidths because of the stronger PC local fields on the ^1H nuclei. One can see in Fig. 3 that, despite the fact that the major
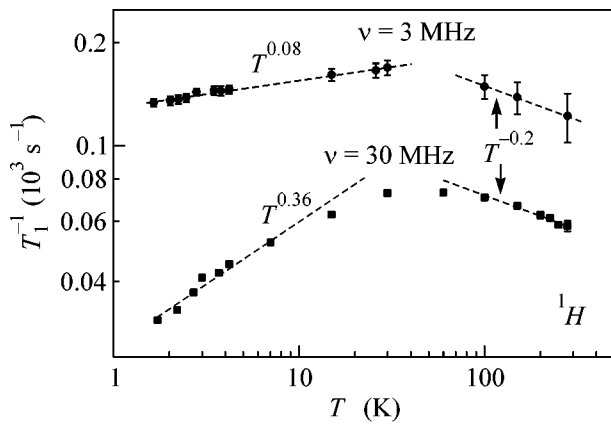
Fig. 4. Temperature dependences of the proton NSLR rate in different magnetic fields.

part of ^{3}He nuclei are situated outside the particle volume, the nuclear magnetic moments of ^{3}He relax in a similar way as ^{1}H. This is likely explained by the high spin-diffusion rate in the ^{3}He gas [11], as a result of which the magnetization transfer from the bulk ^{3}He to the ^{3}He nuclei adsorbed at the surface of carbon particles is fast, so that the bottleneck for ^{3}He NSLR is determined by the relaxation of the surface ^{3}He spins having a relatively low magnetic specific heat in the PC local fields.

It is reasonable to assume that both the isolated PCs and the clusters of exchange-coupled PCs exist at the surface of carbon particles. This exchange interaction should be rather weak, because it is destroyed upon the absorption of the paramagnetic O_2 molecules and, in part, of the inert ^{4}He atoms [8]. For this reason, one can expect that the exchange between the electronic centers will also be suppressed with an increase in magnetic field. In the model suggested, the NSLR rate of protons and ^{3}He spins is given by

$$T_1^{-1} = T_{1,\,is}^{-1} + T_{1,\,clust}^{-1}, \tag{2}$$

where the indices *is* and *clust* correspond to the isolated PCs and the clusters, respectively. The first term in Eq. (2) accounts for the second-type scalar relaxation [9], so that $T_{1,\,is}^{-1} \sim \nu^{-2}$. Assuming that the exchange interaction between the paramagnetic centers is caused by a partial and rather weak overlap of electron shells, one can represent the magnetic-field (frequency) dependence of the second term in Eq. (2) in the form

$$T_{1,\,clust}^{-1} \sim \exp(-K\nu). \tag{3}$$

Since the parameter K includes only the properties of electron shells and should be independent of the types of relaxing nuclei, its values obtained by approximating the frequency dependences are the same for the ^{3}He and ^{1}H NSLRs (Fig. 3).

It is likely that the possible magnetic-field-induced suppression of the interaction between the PCs in the cluster practically did not affect the ^{13}C NSLR rate, because, due to the small gyromagnetic ratio, all measurements were performed in magnetic fields stronger than for ^{3}He and ^{1}H. This caused an appreciably lower ^{13}C NSLR rate. The experiment on measuring the EPR dipolar linewidth in strong magnetic fields (about 3 T) can provide direct confirmation of the suggested field-induced exchange-interaction suppression.

The NSLR model suggested above is in agreement with the experimentally measured temperature dependence of the proton relaxation rate in different magnetic fields (Fig. 4). The increase in the slope of temperature curve and the decrease in the relaxation rate in a higher magnetic field correspond to the increase in the relative contribution of the first term in Eq. (2) as a result of the field-induced suppression of exchange interaction in clusters. The observed frequency-independent maximum in the proton relaxation rate (at temperatures on the order of 60–70 K) and the subsequent change in the temperature dependence are likely associated with the initiation of mobility of the surface PCs and, as a consequence, with a change in the NSLR mechanism.

We intend to gain more detailed information on the exchange clusters and their role in the NSLR from the planned experiments on measuring the temperature dependence of the relaxation rate of liquid and gaseous ^{3}He in the pores of carbon powders.

We note in conclusion that it is the ^{1}H nuclei that are responsible for the main spin-polarization leakage channel in the dynamic polarization using finely dispersed carbonizate powders, because these nuclei interact with the paramagnetic centers more strongly than the magnetic moments of polarized ^{3}He nuclei. The ^{13}C relaxation is much slower and cannot account for the polarization-leakage channel. Therefore, for the successful dynamic polarization of noble gases using carbonizates, one should, first of all, develop a technique for their preparation without proton impurities. When preparing activated carbon from wood, this can be done by cleaning from resins with water vapor under high pressure. In the case of carbonizates prepared from monosaccharides, this can be done by choosing the pyrolysis temperature regime to provide a deeper sample pyrolysis.

REFERENCES

1. B. Driehuys, G. D. Cates, E. Miron, *et al.*, Appl. Phys. Lett. **69**, 1668 (1996); M. V. Romalis and M. P. Ledbetter, Phys. Rev. Lett. **87**, 067601 (2001).

2. E. Stolz, M. Meyerhoff, N. Bigelow, *et al.*, Appl. Phys. B **63**, 629 (1996); M. Leduc, P. J. Nacher, G. Tastevin, and E. Courtade, Hyperfine Interact. **127**, 443 (2000).

3. G. Frossati, J. Low Temp. Phys. **111**, 521 (1998).

4. S. A. Langer, K. DeConde, and D. L. Stein, J. Low Temp. Phys. **57**, 249 (1984).

5. M. S. Tagirov and D. A. Tayurskiǐ, Pis'ma Zh. Éksp. Teor. Fiz. **61**, 652 (1995) [JETP Lett. **61**, 672 (1995)].

6. L. W. Engel and K. DeConde, Phys. Rev. B **33**, 2035 (1986).

7. V. A. Atsarkin, G. A. Vasneva, V. V. Demidov, *et al.*, Pis'ma Zh. Éksp. Teor. Fiz. **72**, 530 (2000) [JETP Lett. **72**, 369 (2000)].

8. G. V. Mamin, H. Suzuki, V. N. Efimov, *et al.*, Physica B (Amsterdam) **329**, 1237 (2002).

9. A. Abragam, *The Principles of Nuclear Magnetism* (Clarendon Press, Oxford, 1961; Inostrannaya Literatura, Moscow, 1963).

10. G. B. Furman, E. M. Kunoff, and S. D. Goren, Phys. Rev. B **52**, 10182 (1995).

11. V. J. Emery, Phys. Rev. A **133**, 661 (1964).

Translated by V. Sakun

Qubit Decoherence by Gaussian Low-Frequency Noise[¶]

K. Rabenstein[1], V. A. Sverdlov[1, 2], and D. V. Averin[1]

[1] *Department of Physics and Astronomy, Stony Brook University, SUNY, Stony Brook, NY 11794-3800, United States*
[2] *V. A. Fock Institute of Physics, St. Petersburg State University, St. Petersburg, 198904 Russia*
Received May 11, 2004

We have derived an explicit nonperturbative expression for decoherence of quantum oscillations in a qubit by Gaussian low-frequency noise. Decoherence strength is controlled by the noise spectral density at zero frequency, while the noise correlation time τ determines the time t of crossover from the $1/\sqrt{t}$ to the exponential suppression of coherence. We also performed Monte Carlo simulations of qubit dynamics with noise which agree with the analytical results. © *2004 MAIK "Nauka/Interperiodica".*

PACS numbers: 03.65.Yz; 03.67.Lx; 72.70.+m

Despite the large number of successful demonstrations of coherent quantum oscillations in individual [1–8] and coupled [9] Josephson-junction qubits, quantitative understanding of these oscillations is so far limited. The main area of discrepancy between experiment and theory is qubit decoherence. The typical quality factors of reported oscillations, while not as large as required by potential applications in quantum computation, are still quite large in physics terms (typically not less than 20–30). This fact should imply weak decoherence describable by the standard perturbation theory in qubit-environment coupling (see, e.g., [10]). Several basic features of this theory, however, do not agree with experimental observations. Most importantly, observed decay time T_2 of coherent oscillations is typically shorter than the energy relaxation time T_1 even at optimal qubit bias points [3, 4, 11], where perturbation theory predicts no pure dephasing terms. Another discrepancy is between the observed two-qubit decoherence rate [9] and its values that can be obtained from the perturbation theory under natural assumptions [12].

Qualitatively, the basic reason for discrepancy between T_1 and T_2 is the low-frequency noise that can reduce T_2 without changing significantly the relaxation fates. Mechanisms of low-frequency, or specifically $1/f$, noise exist in all solid-state qubits: background charge fluctuations for charge-based qubits [13], impurity spins or trapped fluxes for magnetic qubits [14]. Manifestations of this noise are observed in the echo-type experiments [11]. Low-frequency noise for qubits is also created by the electromagnetic fluctuations in filtered control lines.

The goal of our work is to develop a quantitative theory of low-frequency decoherence by studying qubit dynamics under the influence of Gaussian noise with small characteristic amplitude v_0 and long correlation

time τ. In this case, we obtained an explicit nonperturbative expression describing decay in time of coherent qubit oscillations. The strength of decoherence in this expression is controlled by the noise spectral density at zero frequency, $S_v(0) \propto v_0^2 \tau$. For long correlation times $\tau \gg \Delta^{-1}$, where Δ is the qubit tunnel amplitude, $v_0^2 \tau$ can be large even for weak noise $v_0 \ll \Delta$ and our analytical results are exact as a function of $v_0^2 \tau$ in this limit. We also performed direct numerical simulations of the low-frequency qubit decoherence. The simulation results confirm the analytical expressions and show that our main conclusions, cross-over from the $1/\sqrt{t}$ to the exponential suppression of coherence at time $t \simeq \tau$ and the strength of decoherence controlled by the noise spectral density $S_v(0)$ at zero frequency, are valid for quite large noise amplitudes v.

The Hamiltonian of a qubit with a fluctuating bias energy $v(t)$ (see inset in the figure) is

$$H = -\frac{1}{2}[\Delta\sigma_x + (\varepsilon + v(t))\sigma_z], \qquad (1)$$

where ε is the average bias, and σ's here and below denote Pauli matrices. In this work, we mostly focus on the situation when the noise $v(t)$ has characteristic correlation time τ, i.e., the noise correlation function and its spectral density can be taken as

$$\langle v(t)v(t')\rangle = v_0^2 e^{-|t-t'|/\tau}, \quad S_v(\omega) = \frac{2v_0^2\tau}{1+(\omega\tau)^2}, \quad (2)$$

where v_0 is the typical noise amplitude and $\langle \ldots \rangle$ denotes average over different realizations of noise. We assume that the temperature T of the noise-producing environment is large on the scale of the cut-off frequency $1/\tau$ and can be treated as classical. In the regime

---

[¶]This article was submitted by the authors in English.

of interest, $1/\tau \ll \Delta$, the temperature can obviously be still small on the qubit energy scale.

The two effects of the weak noise on the dynamics of qubit (1) are the transitions between two energy eigenstates with energies $\pm\Omega/2$, $\Omega \equiv (\Delta^2 + \varepsilon^2)^{1/2}$, and "pure" (unrelated to transitions) dephasing that suppresses coherence between these states. Within the standard perturbation theory, the transition rate is proportional to $S_v(\Omega) = 2\,v_0^2/\Omega^2\tau$. One can see that the condition of weak noise $v_0 \ll \Delta$ makes the transition rate small compared to both Δ and $1/\tau$, ensuring that the perturbation theory is sufficient for the description of transitions. As was discussed qualitatively in the introduction, the fact that the noise correlation time is long, $\tau \gg \Delta^{-1}$, makes the perturbation theory inadequate for the description of pure dephasing. For low-frequency noise, a proper (nonperturbative in $v_0^2\tau$) description is obtained by looking at the accumulation of the noise-induced phase between the two instantaneous energy eigenstates. If $v_0 \ll \Delta$, one can determine the rate of accumulation of this phase by expanding the energies in noise amplitude $v(t)$. Also, in this case, the dephasing rate is larger than the transition rate and can be calculated disregarding the transitions. The factor $F(t)$ describing suppression in time of coherence between the two states (i.e., suppression of the off-diagonal element ρ_{12} of the qubit density matrix in the energy basis: $\rho_{12}(t) = F(t)\rho_{12}(0)e^{-i\Omega t}$) can be written then as follows:

$$F(t) = \left\langle \exp\left\{-i\int_0^t \left[\frac{\varepsilon v(t')}{\Omega} + \frac{\Delta^2 v^2(t')}{2\Omega^3}\right]dt'\right\}\right\rangle. \quad (3)$$

For Gaussian noise, correlation function (2) determines the noise statistics completely, and it is convenient to take the average in Eq. (3) by writing it as a functional integral over noise. For this purpose, and also for use in the numerical simulations, we start with the "transition" probability $p(v_1, v_2, \delta t)$ [15] for the noise to have the value v_2 a time δt after it had the value v_1:

$$p(v_1, v_2, t)$$
$$= [2\pi v_0^2(1 - e^{-2\delta t/\tau})]^{-1/2}\exp\left\{-\frac{1}{2v_0^2}\frac{(v_2 - v_1 e^{-\delta t/\tau})^2}{1 - e^{-2\delta t/\tau}}\right\}. \quad (4)$$

Using this expression, we introduce the probability of specific noise realization as $p_0(v_1)p(v_1, v_2, \delta t_1)p(v_2, v_3, \delta t_2)\ldots$, where $p_0(v) = (2\pi v_0^2)^{-1/2}\exp\{-v^2/2 v_0^2\}$ is the stationary Gaussian probability distribution of v. Taking the limit $\delta t_j \longrightarrow 0$, we see that the average over the noise can be written as the following function integral:
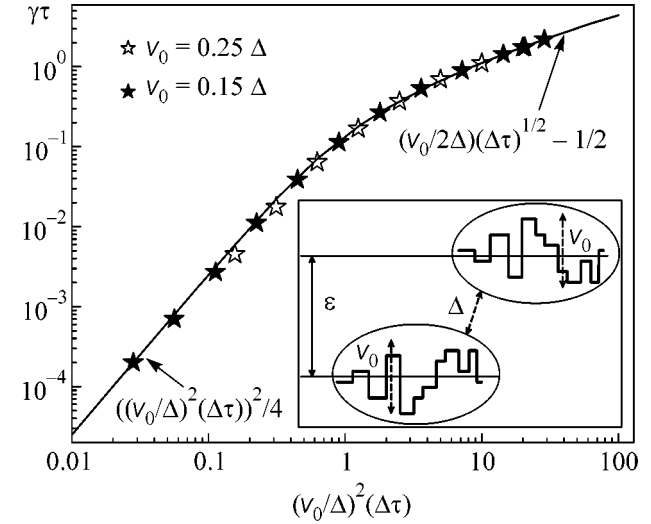
The rate γ of exponential qubit decoherence at long times $t \gg \tau$ for $\varepsilon = 0$ and noise with characteristic amplitude v_0 and correlation time τ. Solid line gives analytical results from Eq. (8). Symbols show γ extracted from Monte Carlo simulations of qubit dynamics. Inset shows schematic diagram of qubit basis states fluctuating under the influence of noise $v(t)$.

$$\langle\ldots\rangle = \int dv(0)dv(t)Dv(t')\ldots\exp\left\{-\frac{v(0)^2 + v(t)^2}{4v_0^2}\right.$$
$$\left. -\frac{1}{4v_0^2\tau}\int_0^t dt'(\tau^2\dot{v}^2 + v^2)\right\}. \quad (5)$$

Since the average in Eq. (3) with weight (5) is now given by the Gaussian integral, it can be calculated straightforwardly:

$$F(t) = F_0(t)\exp\left[-\alpha^2\left(\frac{\nu t}{\tau} - 2\left[\coth\frac{\nu t}{2\tau} + \nu\right]^{-1}\right)\right],$$
$$F_0(t) = e^{t/2\tau}\left[\cosh(\nu t/\tau) + \frac{1+\nu^2}{2\nu}\sinh(\nu t/\tau)\right]^{-1/2}, \quad (6)$$

where $\nu \equiv \sqrt{1 + 2iv_0^2\Delta^2\tau/\Omega^3}$ and $\alpha \equiv \varepsilon\tau v_0/\Omega\nu^{3/2}$.

Equation (6) is our main analytical result. To analyze its implications, we start with the case $\varepsilon = 0$, where pure qubit dephasing vanishes in the standard perturbation theory. Dephasing (6) is still nonvanishing, and its strength depends on the noise spectral density at zero frequency $S_v(0) = 2v_0^2\tau$ through $\nu = \sqrt{1 + is}$, $s \equiv S_v(0)/\Delta$. For small and large times t, Eq. (6) simplifies to

$$F(t) = \begin{cases} \left[\dfrac{1 + t/\tau}{1 + t/\tau + ist/2\tau}\right]^{1/2}, & t \ll \tau, \\[2ex] 2\sqrt{\nu}e^{-(\gamma + i\delta)t}/(1 + \nu), & t \gg \tau, \end{cases} \quad (7)$$

where

$$\gamma = \frac{1}{2\tau}\left[\left(\frac{(1+s^2)^{1/2}+1}{2}\right)^{1/2}-1\right]. \tag{8}$$

Besides suppressing coherence, the noise also shifts the frequency of qubit oscillations. The corresponding frequency renormalization is well denned for $t \gg \tau$:

$$\delta = \frac{1}{2\tau}\left[\frac{(1+s^2)^{1/2}-1}{2}\right]^{1/2}. \tag{9}$$

Suppression of coherence (7) for $t \ll \tau$ can be qualitatively understood as the result of averaging over the static distribution of noise v. In contrast to this, at large times $t \gg \tau$, the noise appears to be δ-correlated, the fact that naturally leads to exponential decay (7). This interpretation means that the two regimes of decay should be generic to different models of the low-frequency noise. Crossover between the two regimes takes place at $t \simeq \tau$, and the absolute value of $F(t)$ in the crossover region can be estimated as $(1 + s^2)^{-1/4}$; i.e., s determines the amount of coherence left to decay exponentially. Rate (8) of exponential decay shows a transition from the quadratic to square-root behavior as a function of $S_v(0)$ that can be seen in the figure, which also shows the decay rate extracted from numerical simulations of Gaussian noise. Our numerical procedure was based on direct Monte Carlo simulations of coherent oscillations of a qubit with Hamiltonian (1) that start in one of the eigenstates of the σ_z operator. The qubit density matrix was averaged over up to 10^7 realizations of noise that were built using transition probability (4). The rate γ of pure dephasing was extracted from the long-time behavior of the off-diagonal element of the density matrix by subtracting the transition-induced dephasing rate $S_v(\Delta)/4 \equiv v_0^2/(2\Delta^2\tau)$ from the total oscillation decay rate. One can see from the figure that the analytical and numerical results agree well for quite large noise amplitudes v.

Nonzero qubit bias ε leads to additional dephasing $F(t)/F_0(t)$ described by the last exponential factor in Eq. (6). The contribution from $F_0(t)$ is of the same form as in $\epsilon = 0$ case but now with $s \longrightarrow s(\Delta/\Omega)^3$. Similarly to $F_0(t)$, the additional dephasing exhibits the crossover at $t \simeq \tau$ from "inhomogeneous broadening" (averaging ever the static distribution of the noise v) to exponential decay at $t \gg \tau$. In contrast to the zero-bias case, the short-time decay is now Gaussian:

$$\ln\left[\frac{F(t)}{F_0(t)}\right] = -\frac{\varepsilon^2}{\Omega^2}\begin{cases} v_0^2 t^2/2, & t \ll \tau, \\ v_0^2 \tau t/(1+is(\Delta/\Omega)^3), & t \gg \tau. \end{cases}$$

We see that, again, the rate of exponential decay depends nontrivially on the noise spectral density $S_v(0)$, changing from direct to inverse proportionality to $S_v(0)$ at small and large s, respectively.

Our approach can be used to calculate the rate of exponential decay at large times t for Gaussian noise with arbitrary spectral density $S_v(\omega)$. Such a noise can be represented as a sum of noises (2), and appropriate transformation of variables in this sum enables one to write the average over the noise as a functional integral similar to (5). For calculation of the relaxation rate at large t, the boundary terms in integral (5) can be neglected and it is dominated by the contribution from the "bulk," which can be conveniently written in terms of the Fourier components

$$v_n = (2/t)^{1/2}\int_0^t dt' v(t')\sin\omega_n t', \quad \omega_n = \pi n/t.$$

Then, $\langle...\rangle = \int Dv ...\exp\{-(1/2)\sum_n |v_n|^2/S_v(\omega_n)\}$. Combining this equation and Eq. (3), we get at large t

$$F(t) = \exp\left\{-\frac{t}{2}\left[\frac{\varepsilon^2\Omega S_v(0)}{\Omega^3+iS_v(0)\Delta^2}\right.\right.$$
$$\left.\left.+\frac{1}{\pi}\int_0^\infty d\omega \ln(1+iS_v(\omega)\Delta^2/\Omega^3)\right]\right\}. \tag{10}$$

For an unbiased qubit, $\varepsilon = 0$, this equation coincides with the one obtained by more involved diagrammatic perturbation theory in quadratic coupling [16].

In summary, we developed a nonperturbative theory of qubit dephasing by Gaussian low-frequency noise and performed Monte Carlo simulations of qubit dynamics with this noise. The theory agrees well with simulations and shows that the decoherence strength is controlled by the noise spectral density at zero frequency. It allows for generalizations in several experimentally relevant directions and should be useful for analysis of observed shapes of quantum qubit oscillations.

REFERENCES

1. Y. Nakamura, Yu. A. Pashkin, and J. S. Tsai, Nature **398**, 786 (1999).

2. J. R. Friedman, V. Patel, W. Chen, *et al.*, Nature **406**, 43 (2000).

3. C. H. van der Wal, A. C. J. ter Haar, F. K. Wilhelm, *et al.*, Science **290**, 773 (2000); I. Chiorescu, Y. Nakamura, C. J. P. M. Harmans, and J. E. Mooij, Science **299**, 1869 (2003).

4. D. Vion, A. Aassime, A. Cottet, *et al.*, Science **296**, 886 (2002).

5. J. M. Martinis, S. Nam, J. Aumentado, and C. Urbina, Phys. Rev. Lett. **89**, 117901 (2002).

6. E. Il'ichev, N. Oukhanski, A. Izmalkov, *et al.*, Phys. Rev. Lett. **91**, 097906 (2003).

7. T. Duty, D. Gunnarsson, K. Bladh, and P. Delsing, Phys. Rev. B **69**, 140503 (2004).

8. J. Claudon, F. Balestro, F. W. J. Hekking, and O. Buisson, *Coherent Oscillations in a Current-Biased dc SQUID* (2004).

9. Yu. A. Pashkin, T. Yamamoto, O. Astafiev, *et al.*, Nature **421**, 823 (2003).

10. K. Blum, *Density Matrix Theory and Its Applications*, 2nd ed. (Plenum, New York, 1991; Mir, Moscow, 1983).

11. Y. Nakamura, Yu. A. Pashkin, T. Yamamoto, and J. S. Tsai, Phys. Rev. Lett. **88**, 047901 (2002).

12. K. Rabenstein and D. V. Averin, Turk. J. Phys. **27**, 313 (2003); cond-mat/0310193.

13. E. Paladino, L. Faoro, G. Falci, and R. Fazio, Phys. Rev. Lett. **88**, 228304 (2002); E. Paladino, L. Faoro, and G. Falci, Adv. Solid State Phys. **43**, 747 (2003); T. Itakura and Y. Tokura, Phys. Rev. B **67**, 195320 (2003); Y. M. Galperin, B. L. Altshuler, and D. V. Shantsev, cond-mat/0312490.

14. N. V. Prokof'ev and P. C. E. Stamp, Rep. Prog. Phys. **63**, 669 (2000).

15. J. L. Doob, Trans. Am. Math. Soc. **52**, 37 (1942); H.-P. Breuer and F. Petruccione, *The Theory of Open Quantum Systems* (Oxford Univ. Press, Oxford, 2002).

16. Yu. Makhlin and A. Shnirman, JETP Lett. **78**, 497 (2003); cond-mat/0308297.

Impurity Pairs and Excitation Relaxation in Doped Silicon

Ya. E. Pokrovskiĭ* and N. A. Khval'kovskiĭ

Institute of Radio Engineering and Electronics, Russian Academy of Sciences, Moscow, 125009 Russia
* *e-mail: yaep@mail.cplire.ru*
Received April 29, 2004

The kinetics of photoconductivity is studied in silicon doped with B, Al, Ga, In, P, As, and Sb with concentrations of 10^{16}–10^{18} cm^{-3} at 4.2 and 10.5 K placed in an 8-mm microwave electric field under pulsed impurity excitation. It is found that infrared absorption by impurity pairs and a slow component of photoresponse relaxation arise at close impurity concentrations. It is shown that this component is due to an increase in the polarization hopping conductivity in the presence of the optical charge exchange of impurity states—isolated impurities and impurity pairs and dipoles (pairs of the major and compensating impurities). The hopping transfer processes of ion charges in the course of relaxation are analyzed. It is shown that the main contribution to polarization photoconductivity comes from hopping transitions in impurity pairs at relatively small concentrations and from hopping with the participation of isolated ions at increased concentrations. © *2004 MAIK "Nauka/Interperiodica"*.

PACS numbers: 71.55.Cn; 72.40.+w

1. Hopping polarization photoconductivity. The initial goal of the study started in 1987 was to develop a contactless method for measuring the relaxation time of impurity photoresponse in silicon doped with group III and V elements with concentrations $N > 10^{16}$ cm^{-3}. For this purpose, the phase and amplitude of the photoresponse of samples was studied as a function of the modulation frequency *f* of the exciting radiation at constant and microwave (MCW) bias voltages [1]. The photoresponse relaxation time in a constant electric field at 20 K did not exceed 10^{-7} s and decreased by two or three orders of magnitude with decreasing temperature and increasing concentration of the compensating impurity N_c. The same relaxation times of the photoresponse U_{MCW} in a microwave field and their dependences on the temperature and compensation were found at $f > 1$ MHz; that is, the process in both cases was determined by the cascade capture of free charge carriers by ionized impurities [2]. However, it was found in [3, 4] that, in an MCW field at $T < 20$ K, not only the fast component but also the slow photoresponse component appear in the photoresponse U_{MCW}. The relaxation time of this component estimated from the dependence of the response on *f* turned out to be of order 10^{-5} s at 5 K. Under low-frequency ($f \sim 1000$ Hz) excitation, U_{MCW} increased both with decreasing *T* and with increasing *N* and N_c. At 5 K, the ratio of the MCW responses under low-frequency and high-frequency excitation reached almost three orders of magnitude [4]. Similar regularities were observed in studying germanium with As [5] and gallium phosphide with Te [6]. Thus, the slow relaxation of the impurity photoresponse in doped semiconductors was manifested only
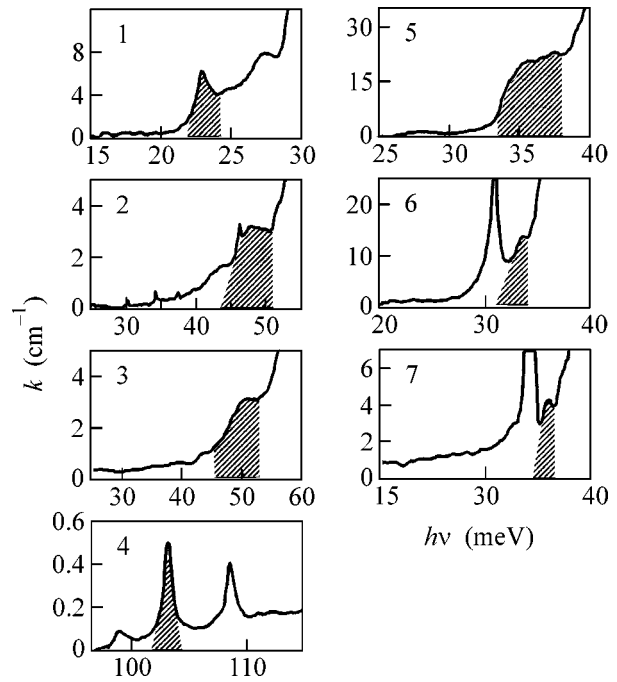
in an MCW electric field. From here, it followed that this phenomenon was associated with hopping photoconductivity (PC). Here, there is a perfect analogy with [7], where the hopping conductivity σ of doped silicon was studied in an alternating electric field. Carrier hopping between neutral and ionized impurities induced by the alternating field changes the distances between the major and compensating impurity ions, that is, changes the dipole moments. This conductivity is of the polarization type and exceeds the percolation conductivity by several orders of magnitude even at low frequencies. It was suggested that excitation can change the hopping conductivity of a semiconductor through the accumulation of charge carriers in long-lived excited 1*S* states of impurities with large orbitals. Optical transitions between these states and the ground 1*S* state are forbidden in the dipole approximation. The charge-carrier photoexcitation cross section in such transitions in silicon does not exceed 10^{-18} cm^2 [8], which corresponds to a radiative lifetime of order 1 s. This suggestion is also confirmed by the fact that the slow relaxation of U_{MCW} has not been exhibited in silicon doped with Bi and Ga at $N \sim 3 \times 10^{16}$ cm^{-3} [3, 4]. Bi, Ga, and Al impurities have high-lying excited states whose energies are close to the energies of optical phonons [9]. Therefore, a captured charge carrier from these higher lying states can rapidly relax to the ground state bypassing the excited 1*S* states. A number of experimental results [10] were in agreement with the model of MCW PC [11] with the participation of long-lived excited states of impurities. However, some experiments were contradictory to such an interpretation. Thus, a decrease in the excitation intensity led to an increase in the relaxation
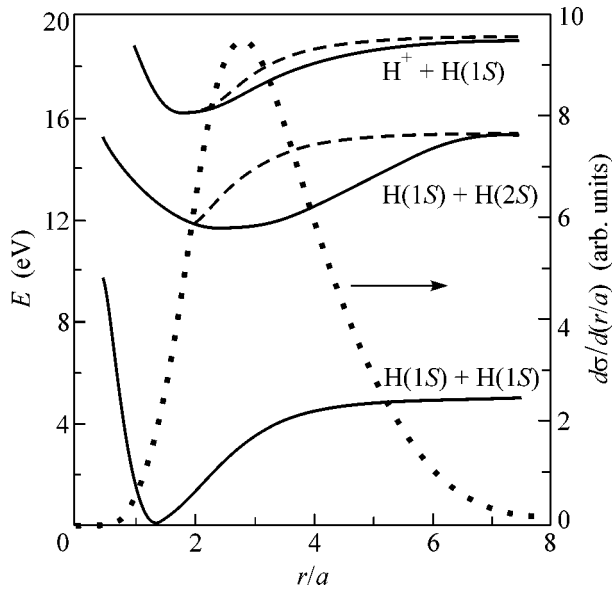
Fig. 1. One-electron terms of the hydrogen molecule (r is the distance between protons, and a is the Bohr radius). The differences between the solid and dashed lines correspond to the decrease in the ionization and excitation energies E with respect to the isolated atoms ($r = \infty$). Points correspond to the relative contribution of the electron transition between the neutral and ionized atoms to the conductivity σ due to an 8-mm electric field [7].

Fig. 2. Spectral dependences of the absorption coefficients k at 4.2 K for silicon with the concentration of impurities N (10^{16} cm^{-3}): (*1*) B (7.6), (*2*) Al (15), (*3*) Ga (16), (*4*) In (40) [21], (*5*) As (18), (*6*) Sb (2.6), and (*7*) P (1.5).

time of U_{MCW} from 10 μs in [3, 4] to 500 μs in [10]. Taking into account the formation of D^- or A^+ centers [12] did not explain such a strong dependence of the relaxation rate on the excitation conditions. Furthermore, it was found that the slow relaxation of U_{MCW} was also exhibited in silicon doped with Ga and Al if $N > 5 \times 10^{16}$ cm^{-3}. Finally, estimates for the probability of transitions with the emission of acoustic phonons [4] showed that the lifetimes of the excited 1S states in silicon did not exceed 10^{-10} s. For these reasons, a new approach to the problem of the polarization conductivity of doped silicon was developed in [13–15].

2. Impurity pairs. The approach is based on taking into account the interaction of impurities. In contrast to fast-diffusing impurities forming close pairs, group III and V impurities are randomly distributed over silicon crystal lattice sites. In the latter case, there is no well-defined boundary between pairs and isolated impurities. However, it is possible to distinguish a group of impurities that must play a leading part in the hopping polarization PC. We will clarify the situation using a system of two protons and two electrons as the simplest analogue. This system is described by the known pattern of the one-electron terms of hydrogen molecule (Fig. 1) [16]. Here, the energy differences between the dashed and solid lines correspond to the decrease in the energies E of electron ionization and excitation to the 2S state as compared to the energies for distant protons. It is evident that the regions in which the energies decrease substantially correspond to distances $r \approx (2$–

5)a, where a is the Bohr radius. In this case, the energy of both neutral and ionized "molecules" is lower than for the isolated hydrogen atom and ion. A similar situation must also take place in the case of impurity pairs in crystals [17], but at different scales of distances and energies, depending on the value of impurity Bohr radii r.

Figure 1 also displays the contribution of carrier hopping to the polarization conductivity $d\sigma(r/a)/d(r/a)$ as a function of r/a calculated for an 8-mm MCW electric field at a random impurity distribution [7]. It is evident that impurity pairs localized in the region $r/a = (2$–5) also make the main contribution to the hopping MCW conductivity. If the concentration of such pairs $N_2 \ll N$, then

$$N_2 = v_0 N^2, \qquad (1)$$

where $v_0 = (4/3)\pi r_0^3$ [13]. Quadratic dependences characteristic of the concentration of pairs with a decreased ionization energy were detected in silicon with an In impurity [18] by the temperature dependence of the Hall constant and in silicon with a P impurity [19] by absorption in bands shifted toward regions of lower energies with respect to photoexcitation peaks of isolated impurities. Similar dependences of the absorption coefficient k on N were observed for a number of other group III and V impurities [20]. The broad absorption spectra of these bands (Fig. 2) are a superposition of the contribution of pairs at various distances between the impurities. The structure of bands is different for both dif-
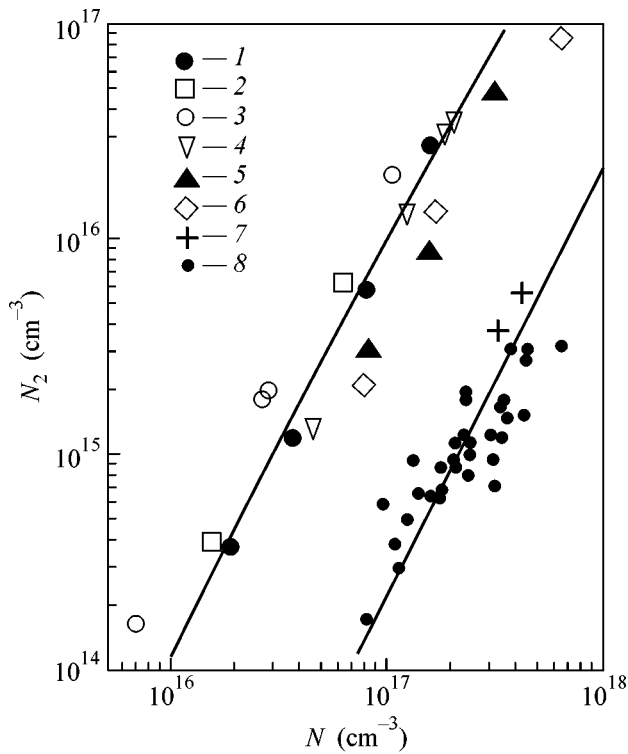
Fig. 3. Dependence of the concentrations of impurities in pairs N_2 on the concentrations of the main impurities N in Si doped with (*1*) B, (*2*) P, (*3*) Sb, (*4*) As, (*5*) Al, (*6*) Ga, and (*7*) In by absorption [21] and photoconductivity [18] and (*8*) In by the Hall effect [18].

ferent impurities and transitions to different excited states but is independent of the impurity concentration N.

In order to compare the results obtained in [20] with the data obtained using Eq. (1), the zones in which the integral absorption corresponds to the concentrations N_2 of the impurities localized at distances no longer than $r_0 = 5a$ are hatched in Fig. 2. In this case, the impurity Bohr radii a are assumed to be $e^2/2\varepsilon E_i$ (here, e is the electron charge, $\varepsilon = 12$ is the dielectric constant, and E_i is the ionization energy). The zone widths were determined from the ratio of their areas to the areas of narrow absorption peaks at transitions to the corresponding excited states of impurities with the known small ($N < 10^{15}$ cm^{-3}) concentrations. The dependences of the concentrations of impurities in the pairs N_2 on the concentrations N of doping impurities obtained on the basis of Eq. (1), [20], and Fig. 2 are shown in Fig. 3 [13–15]. For an In impurity, the same figure also shows the dependence of N_2 on N from [18] and the values of N_2 estimated from [18] by the photoconductivity spectrum and from [21] by the absorption spectrum. It is seen that the values of N_2 for the In impurity determined from different experiments agree with each other. The solid lines correspond to Eq. (1) for a B impurity ($a = 1.3$ nm) and an In impurity ($a = 0.38$ nm). Long-wavelength absorption is revealed at $N v_0 > 10^{-2}$. Thus, the stronger

the localization of charge carriers in the ground state of impurities, the higher the concentrations at which absorption by pairs is observed. Moreover, the slow relaxation of U_{MCW} arises in the same regions of concentrations of various impurities. This fact is an important indication of the participation of the impurity pairs in MCW PC.

3. Optical charge exchange of impurity states and the relaxation of excitation. Consider a situation in n-type silicon at thermodynamic equilibrium and low temperatures. The doping impurity pairs at $N \gg N_c$ were weakly ionized. The doping impurity ions are mainly localized on the nearest distances from the compensating ions, forming pairs of a different type, namely, dipoles in a concentration of N^{+-}. Thus, at $T = 5$ K, $N = 10^{16}$ cm^{-3}, and $N_c = 10^{14}$ cm^{-3}, the concentration of ions N^+ that are not bound into dipoles does not exceed $0.1N_c$ and decreases with increasing N and N_c; that is, $N^{+-} \approx N_c$ [2]. At low temperatures, ions in the dipoles make no contribution to the MCW conductivity, because electron hopping from more distant impurities to dipoles is possible only upon energy absorption.

Excitation results in the random ionization of an impurity, whereas the capture of free carriers leads to optical charge exchange decreasing N^{+-} and increasing N^+ and N_2^+. Electron hopping between such ionized and neutral impurities makes a contribution to MCW PC. Under experimental conditions, silicon is excited by radiation pulses with intensity I and duration Δt, which is much longer than the lifetime of free charge carriers τ but much shorter than the relaxation time of U_{MCW}. Then, a steady-state concentration of free charge carriers $n = ISN/\alpha N_c$ (where S is the photoionization cross section and α is the capture coefficient) is reached in a time exceeding $\tau = 1/\alpha N_c$, and the charge-exchange process can be described by the equations [14, 15]

$$dN^{+-}/dt = ISN - \alpha n N^{+-};$$

$$N^{+-} = N_c - N + \ll N, \qquad (2)$$

$$dN_2^+/dt = IS(N_2 - N_2^+) - \alpha n N_2^+,$$

from which

$$N^+ = N(1 + N/N_c)^{-1}[1 - \exp(-ISt(1 + N/N_c))],$$

$$N_2^+ = N(1 + N/N_c)^{-1}[1 - \exp(-ISt(1 + N/N_c))]. \qquad (3)$$

At $N \gg N_c$, the amplitudes of U_{MCW} due to the charge exchange of isolated impurities and impurities in pairs are proportional to N_c. It also follows from Eq. (3) that the limiting charge exchange of impurities is reached if more than N_c ionizations ($ISNt > N_c$) proceed in time t in a unit volume. Then, a steady nonequilibrium state is reached in the crystal

$$N^+ \approx N_c; \quad N^{+-} \approx N_c^2/N \ll N_c;$$

$$N_2^+ \approx N_2 N_c/N = v_0 N N_c \ll N_2, \quad N^+. \qquad (4)$$

A further increase in intensity must lead only to an increase in the concentration of free carriers rather than to a noticeable change in the ion concentration. It is clear from Eq. (4) that only a small fraction of impurities in pairs is ionized in charge exchange, while $N_2^+ \ll N^+$. Therefore, the contribution of hopping to U_{MCW} with the participation of isolated impurity ions should also be taken into account, despite the fact that the hopping probability in this case is substantially smaller than in pairs.

The relaxation of excitation proceeds as a result of electron transitions between neutral and ionized impurities. The neutralization of an ionized impurity in a pair can be accomplished as a result of a single hopping with energy release at any $r/a > 1$, and its rate should not strongly depend on the temperature. However, the probability that a third impurity is located at a small or even medium distance from the pair must decrease with decreasing r/a. Therefore, the rate of charge relaxation for "close" pairs must be lower than for "distant" pairs, and the relaxation of U_{MCW} must be nonexponential. A crude estimate shows [15] that the relaxation rate can vary in the range 10^7–10^1 s^{-1} at $N \approx 10^{16}$ cm^{-3}. However, the relaxation time must increase proportional to Na^3 and only weakly depend on N_c, because impurities in the vicinity of pairs are mainly neutral.

The isolated impurity ions can make a contribution to MCW PC (Fig. 1) until they are bound into dipoles. Localization occurs as a result of the hopping drift of the ion charge in the constant electric field of compensating impurity ions. The average drift time is the Maxwellian relaxation time of the space charge [11, 14, 15]

$$\tau_m = \varepsilon/4\pi\mu e N^+, \qquad (5)$$

determined by the local conductivity of the medium $\sigma = e\mu N^+$. At the extreme optical charge exchange ($N^+ \approx N_c$), the time dependence of the concentration N^+ can be described by the equation

$$N^+ = N_c \exp(-t/\tau_m). \qquad (6)$$

Here, τ_m itself depends on the concentration of isolated ions N^+. For comparison with experiment, it is convenient to write Eq. (6) in the form

$$-(\varepsilon/4\pi e\mu N_c)(N_c/N^+)\ln(N^+/N_c) = t. \qquad (7)$$

An increase in the relaxation rate due to an increase in the hopping conductivity μ with both increase in N_c and increase in N and T must be a characteristic manifestation of this component of U_{MCW}. It should be expected that hopping with the participation of N^+ ions will be manifested at relatively high concentrations N. At lower concentrations, when the charge relaxation time is larger than the pulse excitation period, a quasi-steady-state concentration N^+ will be reached, and this component of U_{MCW} will not be observed. Thus, the effects of impurity concentration and temperature on the relax-

ation of MCW PC with the participation of pairs and isolated impurities must be substantially different. This allows us to elucidate the conditions under which one of the processes predominates.

4. Relaxation of polarization photoconductivity. In order to investigate the impurity photoresponse kinetics [13–15], doped silicon samples were excited by CO_2-laser radiation pulses (10.6 μm) with a frequency of about 200 Hz. The time dependences of the photoresponses in constant and microwave electric fields were analyzed with a gate integrator with an aperture of 0.5 or 5 μs. The pulse duration, $\Delta t \sim 0.5$ μs, was much longer than the lifetime of free charge carriers τ but much shorter than the relaxation time of U_{MCW}. The energy of pulses at $N_c \sim 10^{14}$ cm^{-3} usually did not exceed 10^{-6} J and was sufficient for the saturation of the slow component of the MCW signal. A further increase in the intensity gave rise to an increase in only the fast component of U_{MCW}, which repeated the response at a constant bias. The fast and slow components of U_{MCW} were of the same polarity corresponding to an increase in the absorption of MCW radiation owing to an increase in the conductivity of the samples upon excitation.

The dependences of the photoresponse U_{MCW} on time t are shown in Fig. 4 for silicon doped with a number of group III and V impurities. It is evident in the figure that the relaxation of the response is nonexponential for all impurities. The start of relaxation corresponds to times of 10–50 μs, which increase to 0.5–2.5 ms as the detection delay increases. It is also seen in the figure that the relaxation rate depends on the nature of impurities. Thus, at $N = 6 \times 10^{16}$ cm^{-3}, the relaxation rate in silicon with P, Al, and Ga decreases as the Bohr radius a of these impurities decreases.

The relaxation time of U_{MCW} depends on the concentration N of main impurity as well. The time dependences of U_{MCW} for silicon doped with boron in relatively small concentrations are shown in Figs. 5 and 6. It is seen that the relaxation time changes initially from 25 μs ($N = 1.8 \times 10^{16}$ cm^{-3}) to 10 μs ($N = 4 \times 10^{16}$ cm^{-3}) and from 1.2 ms to 0.5 ms at a detection delay of 1 ms, that is, decreases as approximately $1/N$. However, it is evident in Fig. 5 that the time dependences at equal concentrations N differ insignificantly even if concentrations N_c in the samples differ by several times. On the other hand, the response amplitude increases with increasing N_c. This agrees with [4], where it was found for a series of samples doped with B ($N = 3.3 \times 10^{16}$ cm^{-3}) and compensated with P that $U_{\mathrm{MCW}} \sim N_c$ at modulation frequency $f = 1$ kHz of intense (20–50 mW) excitation.

Such simple dependences were observed for boron concentrations $N < 5 \times 10^{16}$ cm^{-3}, and then the slower component of the relaxation of U_{MCW} was exhibited again (Fig. 7). It is seen in the figure that the time dependences of U_{MCW} at 4.2 K are similar at $t > 0.5$ ms, though the concentrations N and N_c in the samples strongly differ. However, as the temperature was
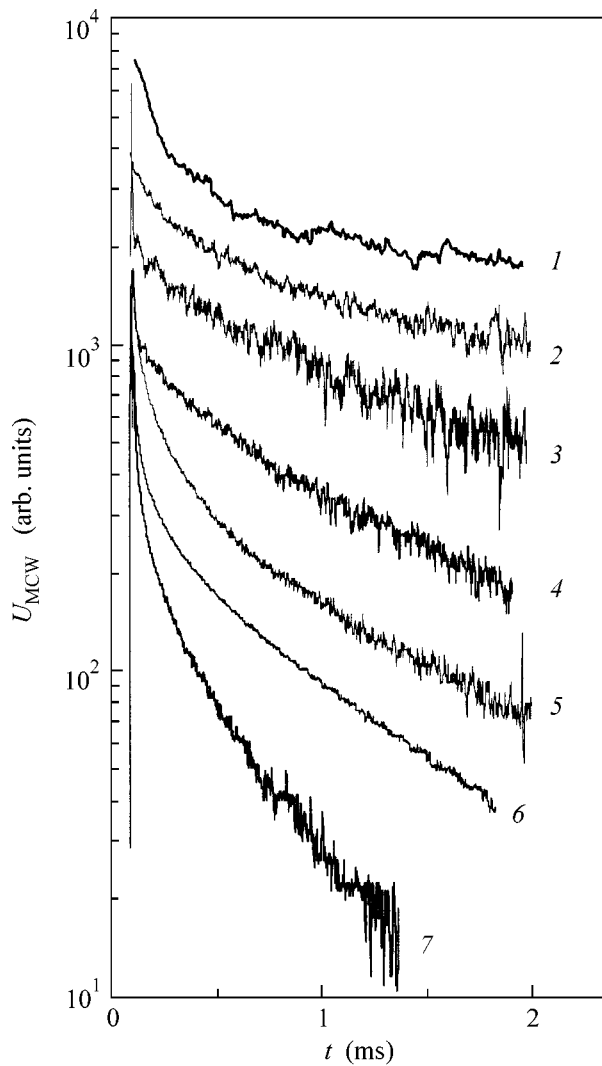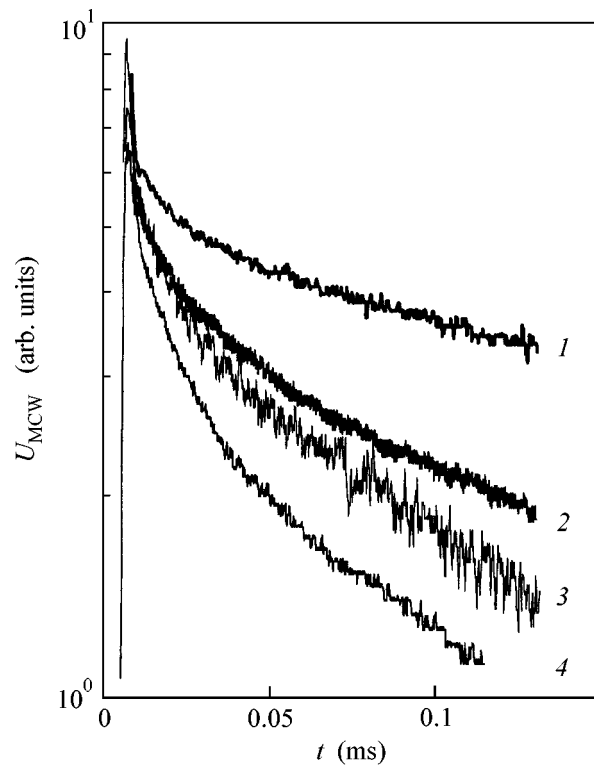
Fig. 4. Time dependences of the photoresponse of Si doped with impurities in concentrations (10^{16} cm^{-3}) (*1*) In (10), (*2*) Sb (2.6), (*3*) Ga (6), (*4*) B (2.4), (*5*) Al (6), (*6*) P (6), and (*7*) As (18) in a microwave electric field U_{MCW}.

Fig. 5. Time dependences of U_{MCW} for Si doped with B and P in concentrations N, N_c (10^{16} cm^{-3}): (*1*) (1.8, 10^{-2}), (*2*) (3.3, 10^{-2}), (*3*) (3.3, 2×10^{-3}), and (*4*) (3.95, 10^{-2}). The aperture is 0.5 μs.

increased to 10.5 K, the relaxation rate did not change at $N = 2.4 \times 10^{16}$ cm^{-3} but increased by approximately one order of magnitude at $N = 5.5 \times 10^{16}$ cm^{-3}. From here, it follows that hopping transitions between pairs of the main impurity make the main contribution to the polarization PC at relatively small boron concentrations (Figs. 5, 6), whereas the slow relaxation of U_{MCW} associated with the contribution to PC from isolated ions appears with increasing N. In the latter case, the time dependence of $U_{MCW} \sim N^+$ must be described by a logarithmic law (Eq. (7)).

The time dependences of U_{MCW} are shown in Fig. 8 for two samples transformed according to Eq. (7) to the form

$$[U(0)/U(t)]\ln[U(t)/U(0)] = t. \qquad (8)$$

It is evident that straight lines fit the experimental points well. The slope of these lines corresponds to

$-\varepsilon/4\pi e\mu N_c$. Hence, it follows that the mobility μ does not depend on time and has a usual physical meaning. Figure 8 demonstrates that, in sample *1* ($N = 5.5 \times 10^{16}$, $N_c = 5 \times 10^{15}$ cm^{-3}), $\sigma(0) = 2.4 \times 10^{-8}$ Ω^{-1} cm^{-1} at 4.2 K and $\sigma(0) = 2 \times 10^{-7}$ Ω^{-1} cm^{-1} at 10.5 K; the hopping mobilities μ are equal to 3×10^{-5} and 2×10^{-4} cm^2 V^{-1} s^{-1}. In sample *2* ($N = 1.15 \times 10^{17}$, $N_c = 10^{14}$ cm^{-3}), $\sigma(0) = 2 \times 10^{-8}$ Ω^{-1} cm^{-1} and $\mu = 1.25 \times 10^{-3}$ cm^2 V^{-1} s^{-1} at 4.2 K. These results confirm that the hopping transitions of isolated ions N^+ contribute to the polarization PC. However, the absolute values of hopping conductivity in the constant field of compensating impurity ions are several orders of magnitude greater than the values typical of doped silicon at a thermodynamic equilibrium. Moreover, the conductivity of sample *1* increases as the temperature increases from 4.2 to 10.5 K by only one order of magnitude, whereas an increase in σ by a factor of approximately 250 should be expected for the activation energy $E_3 = 4.3$ meV corresponding to a concentration of 5.5×10^{16} cm^{-3} (see [22, 23] and references cited therein). Such a discrepancy is natural for two reasons. First, at low temperatures in the absence of excitation, most of the ions of the main impurity are bound into dipoles [3] which make no contribution to hopping conductivity. Second, the drift of the charge of main impurity ions occurs as a result of several jumps in the potential well over the
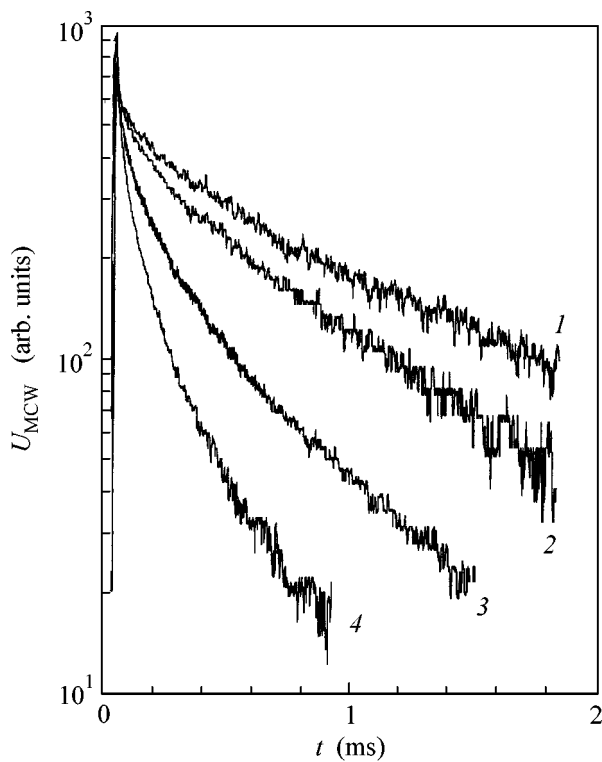
Fig. 6. Time dependences of U_{MCW} for Si doped with B and P in concentrations N (10^{16} cm^{-3}) and $N_c = 10^{14}$ cm^{-3}: (*1*) (1.8), (*2*) (2.4), (*3*) (3.3), and (*4*) (3.95). The aperture is 5 μs.
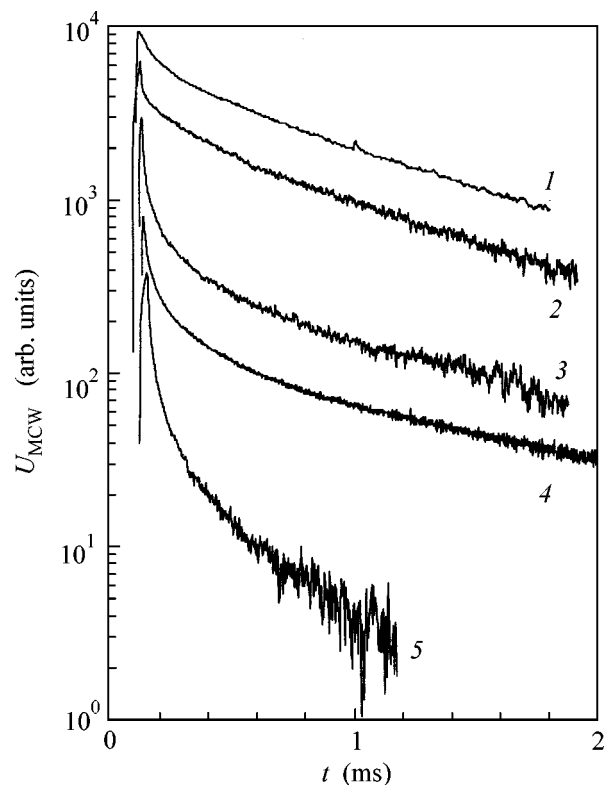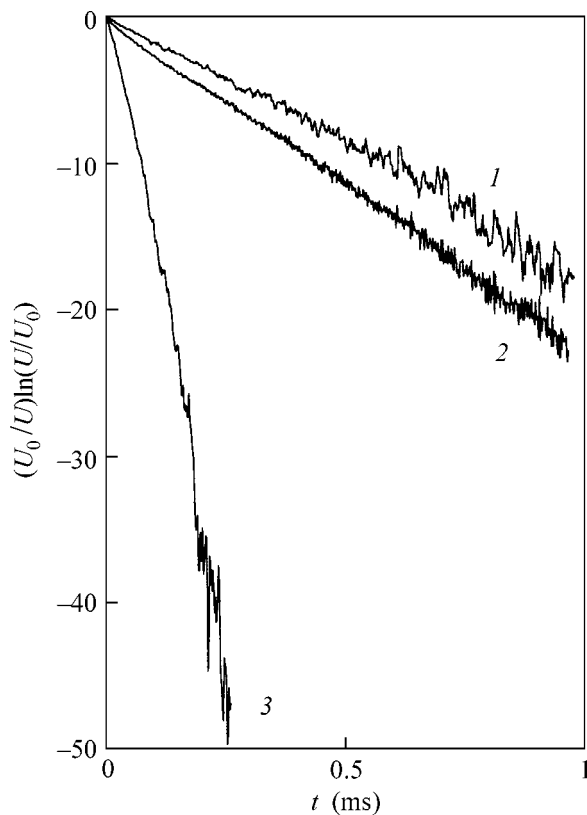

Fig. 7. Time dependences of U_{MCW} for Si doped with B and P in concentrations N, N_c (10^{16} cm^{-3}): (*1*) (2.4, 10^{-2}), 4.2 K; (*2*) (2.4, 10^{-2}), 10.5 K; (*3*) (11.5, 10^{-2}), 4.2 K; (*4*) (5.5, 0.5), 4.2 K; and (*5*) (5.5, 0.5), 10.5 K.

states of impurities with energies decreasing as compensating impurity ions are approached. This charge transfer is activationless, and its rate can be completely independent of temperature. It is possible that the observed temperature dependence is associated with the thermal ionization of the dipoles at 10.5 K [2], which leads to an increase in the equilibrium concentration N^+ and in the relaxation rate. Thus, hopping conductivity in the constant electric field of point charges, which determines the relaxation rate of MCW PC, radically differs from percolation conductivity in an external field. At the values of conductivity determined from the dependences in Fig. 8, the slow component of its relaxation in a constant field would be readily detected even at 4.2 K. However, even at elevated temperatures and with a sufficiently sensitive detection method, this component could not be distinguished.

Conclusions. Based on the experiments performed, a simple explanation is offered for the physical nature of the hopping photoconductivity of doped silicon in a microwave electric field. It is relied upon taking into account interactions due to which impurities can reside in the states of isolated atoms and ions, pairs of the main impurity, and dipoles (pairs of ions of the main and compensating impurities). From the spectra of absorption bands, the concentrations of impurity pairs N_2 were estimated for silicon doped with B, Al, Ga, In, P, As, and Sb with concentrations N(10^{16}–10^{18} cm^{-3}). It is found that these bands are manifested if $N_2 > 10^{-2}N$. In this case, the stronger the localization of the charge carrier in the ground state of impurities, the higher the concentrations at which long-wavelength absorption is exhibited. It is shown that the absorption by impurity pairs and the slow relaxation of MCW PC occur at close concentrations N. The relaxation of MCW PC under pulse impurity photoexcitation is nonexponential, and its rate increases with increasing N but weakly depends on the temperature and compensation. Using a boron impurity as an example, it has been shown that these regularities are fulfilled at $N < 5 \times 10^{16}$ cm^{-3}. As the concentration increases, the slower component of MCW PC appears again, and its rate increases with increasing temperature and compensation. The regularities observed are explained by the optical charge exchange of impurities in various states upon their photoionization. As a result, the concentration N^{+-} of the dipoles into which ions of the main and compensating impurities were bound before excitation decreases, and the concentrations N_2^+ of ionized impurities in pairs and isolated ions N^+ increase. These ions can participate in hopping transitions and contribute to MCW PC. As the excitation intensity increases, the limiting opti-

Fig. 8. Time dependences of the photoresponse $[U(0)/U(t) \cdot \ln(U(t)/U(0))]$ for Si doped with B and P in concentrations N, N_c (10^{16} cm^{-3}): (1) (11.5, 10^{-2}), 4.2 K; (2) (5.5, 0.5), 4.2 K; and (3) (5.5, 0.5), 10.5 K.

cal charge exchange is reached, at which the slow component of MCW PC is saturated. The relaxation of charge exchange occurs as a result of the hopping transfer of ion charges. One jump would suffice to neutralize a pair, and this fast relaxation process predominates at low concentrations N. Isolated ions contribute to PC until they become again bound into dipoles in the time of hopping-charge drift in the electric field of compensating impurity ions. The rate of the process in this case is determined by the space-charge relaxation time, that is, by the conductivity of the medium, which depends both on the concentration of the main and compensating impurities and on temperature. Thus, MCW PC with the participation of isolated ions is exhibited at high concentrations and a significant compensation. The drift occurs in the potential wells of compensating impurity ions and is not associated with percolation. The local conductivity, which determines the drift time, exceeds the percolation conductivity of silicon with a close impurity composition by several orders of magnitude.

REFERENCES

1. I. V. Altukhov, Ya. E. Pokrovskiĭ, O. I. Smirnova, *et al.*, Fiz. Tekh. Poluprovodn. (Leningrad) **24**, 1134 (1990) [Sov. Phys. Semicond. **24**, 717 (1990)].

2. V. N. Abakumov, V. I. Perel', and I. N. Yassievich, *Nonradiative Recombination in Semiconductors* (S.-Peterb. Inst. Yad. Fiz. Ross. Akad. Nauk, St. Petersburg, 1997) [in Russian].

3. Ya. E. Pokrovskiĭ and O. I. Smirnova, Pis'ma Zh. Éksp. Teor. Fiz. **51**, 377 (1990) [JETP Lett. **51**, 429 (1990)].

4. Ya. E. Pokrovskii and O. I. Smirnova, Mater. Sci. Forum **65–67**, 271 (1990).

5. Ya. E. Pokrovskiĭ, O. I. Smirnova, and N. A. Khval'kovskiĭ, Pis'ma Zh. Éksp. Teor. Fiz. **61**, 602 (1995) [JETP Lett. **61**, 624 (1995)].

6. Ya. E. Pokrovskiĭ, O. I. Smirnova, and N. A. Khval'kovskiĭ, Zh. Éksp. Teor. Fiz. **114**, 2204 (1998) [JETP **87**, 1201 (1998)].

7. M. Pollak and T. M. Geballe, Phys. Rev. **122**, 1724 (1961).

8. Ya. E. Pokrovskiĭ, O. I. Smirnova, and N. A. Khval'kovskiĭ, Zh. Éksp. Teor. Fiz. **117**, 457 (2000) [JETP **90**, 404 (2000)].

9. A. K. Ramdas and S. Rodrigues, Rep. Prog. Phys. **44**, 1278 (1981).

10. Ya. E. Pokrovskiĭ and O. I. Smirnova, Zh. Éksp. Teor. Fiz. **102**, 660 (1992) [Sov. Phys. JETP **75**, 353 (1992)].

11. Ya. E. Pokrovskiĭ and O. I. Smirnova, Zh. Éksp. Teor. Fiz. **103**, 1411 (1993) [JETP **76**, 690 (1993)].

12. Ya. E. Pokrovskiĭ, O. I. Smirnova, and N. A. Khval'kovskiĭ, Pis'ma Zh. Éksp. Teor. Fiz. **66**, 224 (1997) [JETP Lett. **66**, 241 (1997)].

13. Ya. E. Pokrovskii and N. A. Khvalkovskii, Phys. Status Solidi C **0**, 707 (2003).

14. Ya. E. Pokrovskiĭ and N. A. Khval'kovskiĭ, Fiz. Tekh. Poluprovodn. (St. Petersburg) **37**, 1305 (2003) [Semiconductors **37**, 1266 (2003)].

15. Ya. E. Pokrovskiĭ and N. A. Khval'kovskiĭ, Radiotekh. Élektron. (Moscow) **48**, 1120 (2003).

16. *Tables of Physical Data: Reference Book*, Ed. by I. K. Kikoin (Atomizdat, Moscow, 1976) [in Russian].

17. Sh. M. Kogan and A. F. Polupanov, in *Proceedings of 3rd International Conference on Shallow Impurities in Semiconductors, Linchoping, Sweden, 1988* (1989), Inst. Phys. Conf. Ser., Vol. 95, p. 527.

18. F. Baron, M. Young, O. J. Neeland, and O. Marsh, Appl. Phys. Lett. **30**, 594 (1977).

19. G. Thomas, M. Capizzi, F. De Rosa, *et al.*, Phys. Rev. B **23**, 5472 (1981).

20. Ya. E. Pokrovskiĭ, O. I. Smirnova, and N. A. Khval'kovskiĭ, Zh. Éksp. Teor. Fiz. **122**, 97 (2002) [JETP **95**, 83 (2002)].

21. W. Scott, Appl. Phys. Lett. **32**, 540 (1978).

22. B. I. Shklovskiĭ and A. L. Éfros, *Electronic Properties of Doped Semiconductors* (Nauka, Moscow, 1979; Springer, New York, 1984).

23. R. K. Ray and H. Y. Fan, Phys. Rev. **121**, 768 (1961).

Translated by A. Bagatur'yants